Photodeposition of Gold and Platinum on Titanium Dioxide

Marko Vaelma

School of Chemical Engineering

Thesis submitted for examination for the degree of Master of Science in Technology.

Espoo 20.11.2017

Thesis supervisor:

Prof. Ilkka Tittonen

Thesis advisor:

M.Sc. Jorma Selin

Aalto University
School of Chemical Technology

AALTO UNIVERSITY
SCHOOL OF CHEMICAL TECHNOLOGY

ABSTRACT OF THE
MASTER'S THESIS

Author: Marko Vaelma

Title: Photodeposition of Gold and Platinum on Titanium Dioxide

Date: 20.11.2017 Language: English Number of pages: 8+103

Department of Electronics and Nanoengineering

Professorship: S-129 Electrophysics

Supervisor: Prof. Ilkka Tittonen

Advisor: M.Sc. Jorma Selin

In photochemistry, light is used as an energy source for chemical reactions, such as hydrogen fuel generation and water purification. Photocatalytic materials often require a cocatalytic material to increase the efficiency of the reactions. The most typical cocatalytic materials are noble metals, such as gold and platinum.
This thesis studies the photodeposition of gold and platinum nanoparticles. Photodeposition is conducted on an ALD grown titanium dioxide layer that acts as a photoactive material and absorbs incident photons, initiating the metal reduction of metal ions. The results of the photodeposition process can be controlled by changing the process parameters. The influence of multiple parameters are characterized with scanning electron microscopy, followed by image analysis. The results obtained are further discussed and conclusions are drawn on the capabilities of photodeposition.
In this thesis, photodeposition process is used to control the particle size and particle density of noble metal nanoparticles. Significant variation is achieved for both gold and platinum nanoparticles by changing the process parameters. The particle densities for platinum nanoparticles varied from 120 μm^{-2} to 4993 μm^{-2}, and the average particle diameters from 3.09 nm to 5.89 nm. The particle densities for gold range from 28.7 μm^{-2} to 440.1 μm^{-2}, and the particle diameters from 15.86 nm to 37.25 nm. The most influential process parameter for increasing both the particle size and density is discovered to be precursor concentration. According to the results obtained in this thesis, photodepostion can be used to control the size and density of the deposited nanoparticles.

Keywords: Gold, Platinum, Titanium dioxide, Photodeposition, Photocatalyst, Cocatalyst, Atomic layer deposition

AALTO-YLIOPISTO
KEMIAN TEKNIIKAN KORKEAKOULU

DIPLOMITYÖN
TIIVISTELMÄ

Tekijä: Marko Vaelma

Työn nimi: Platinan ja kullan fotodepositio titaanidioksille

Päivämäärä: 20.11.2017 Kieli: Englanti Sivumäärä: 8+103

Elektroniikan ja nanotekniikan laitos

Professuuri: S-129 Sähköfysiikka

Työn valvoja: Prof. Ilkka Tittonen

Työn ohjaaja: DI Jorma Selin

Fotokemiallisissa sovelluksissa valo toimii energianlähteenä reaktioille, joilla voidaan esimerkiksi tuottaa vetypolttoainetta tai puhdistaa vettä epäpuhtauksista. Fotokatalyyttiset materiaalit vaativat usein katalyytin parantamaan reaktioiden tehokkuutta. Nämä kokatalyytit ovat tyypillisimmin jalometallisia partikkeleja kuten kultaa tai platinaa.

Tässä työssä käytetään fotodepositio-menetelmää kulta- sekä platinananopartikkelien valmistukseen. Fotodepositio suoritetaan ALD kasvatetulle titaanidioksidi pinnalle, joka absorboi pintaan osuvat fotonit käynnistäen metallin pelkistysreaktion. Fotodepositiota voidaan kontrolloida muuttamalla prosessiparametreja. Parametrien vaikutusta pelkistettyihin metallipartikkeleihin tutkitaan pyyhkäisyelektronimikroskoopialla, ja sitä seuraavilla kuva-analyyseillä. Saatuja tuloksia tarkastelemalla voidaan tehdä johtopäätöksiä fotodeposition soveltuvuudesta jalometallinanopartikkelien valmistukseen.

Tämä työ esittelee fotodeposition mahdollisuudet jalometallipartikkelien tiheyden sekä koon säätelemiseksi. Prosessiparametreja muuttamalla on mahdollista vaikuttaa niin kulta- kuin platinapartikkelienkin muodostumiseen. Platinapartikkelien tiheys vaihteli 120 μm^{-2}:stä 4993 μm^{-2}:in, ja partikkelien halkaisija 3.09 nm:stä 5.89 nm:iin. Kultapartikkelien tiheys puolestaan on välillä 28.7 μm^{-2} – 440.1 μm^{-2}, kun taas niiden halkaisijat vaihtelevat 15.86 nm:sta 37.25 nm:iin. Suurin muutos sekä partikkelikoossa että -tiheydessä saadaan aikaan metallisuolan konsentraatiota kasvattamalla. Työn tulosten perusteella fotodepositio-menetelmää voidaan käyttää kulta- ja platinapartikkelien koon sekä tiheyden kontrolloimiseen.

Avainsanat: Platina, Kulta, Titaanidioksidi, Fotodepositio, Fotokatalyytti, Kokatalyytti, Atomikerroskasvatus

Preface

First of all, I would like to thank my advisor Jorma Selin for allowing a *chemist* to participate in the OptoBio project, and guiding me fearlessly throughout the thesis. I show my gratitude also to Camilla Tossi and the VTT people for working towards the same goal in this project. I want to thank professor Ilkka Tittonen for making me a part of the Micro and Quantum Systems group and for supervising my thesis. Additionally, a thanks to the whole MQS group for helping me with my daily struggles with MATLAB and LaTeX, as well as keeping the mood light throughout my stay here at the Micronova Nanofabrication Centre.

Last but not least, I thank my friends and family for the support I have received for all my life thus far. And of course, I show my gratitude to Hilde, who still voluntarily agrees to spend most of her free time with me.

Otaniemi, 20.9.2017

Marko Vaelma

Contents

Symbols and abbreviations

Symbols

c	speed of light in vacuum $\approx 3 \times 10^8$ [m/s]
C	concentration
D	diffusion coefficient
D_{ox}	oxidation state distribution
D_{red}	reduction state distribution
$\bar{d}$	average diameter
d_p	diameter of scanning electron probe
E	photon energy
E_C	conduction band energy
E_F	Fermi level energy
E_{Fn}	quasi-Fermi level of electrons
E_{Fp}	quasi-Fermi level of holes
$E(r^2)$	second moment of variable r
E_t	energy level of trap site
E_V	valence band energy
h	Planck constant $\approx 4.14 \times 10^{-15}$ [eV×s]
i_p	electron probe current
k_B	Boltzmann constant $\approx 8.62 \times 10^{-5}$ [eV×K^{-1}]
L	carrier diffusion length
$L(A)$	area defined by A
m_A	mass per area A
M	median
m_{ef}	effective mass of charge carrier
n	electron concentration
N	number of points
n'	photogenerated electron concentration
N_A	number of particles in analyzed area
N_C	density of states in the conduction band
n_i	intrinsic carrier concentration
N_V	density of states in the valence band
p	hole concentration
P	intensity of light
p'	photogenerated hole concentration
q	elementary charge
r	radius
R^2	indicator value of the goodness of fit
$\bar{r_A}$	average nearest neighbor distance
R_{CE}	indicator value of Clark-Evans test
$\bar{r_E}$	average nearest neighbor distance of randomly distributed points with density ρ
r_{NND}	nearest neigbor distance
t	time

T	temperature
v	drift velocity
V_o	acceleration voltage
α_f	convergence angle of electron probe
β	brightness of electron beam
ϵ	realtive permittivity
λ	wavelength of light
Λ	points per area
μ	expectation of distribution
μ_m	carrier mobility
ν	frequency of light
ϕ	work function
ρ	event density
σ	standard deviation
σ^2	variance
σ_{rE}	standard error associated with variable $\bar{r_E}$
τ	carrier lifetime
τ_m	mean free time of between charge carrier collisions
$\mathcal{E}$	electric field

Abbreviations

ACE	acetone
ALD	atomic layer deposition
BSE	backscattered electron
CB	conduction band
CVD	chemical vapor deposition
DIW	de-ionized water
FE-SEM	field emission scanning electron microscope
FTO	fluorine doped tin oxide
IEP	isoelectric point
IPA	isopropyl alcohol
NHE	normal hydrogen electrode
NND	nearest neighbor distance
PEC	photoelectrochemical cell
SRH	Shockely-Read-Hall
SE	secondary electron
SEM	scanning electron microscope
UV	ultraviolet
VB	valence band

1 Introduction

Sunlight is an intriguing source of energy. In addition to electricity production, solar energy can be utilized in photocatalytic reactions. In photocatalysis, solar radiation is absorbed by a photocatalyst, generating an electron-hole pair. These photogenerated charge carriers may participate in various oxidation and reduction reactions on the surface of the photocatalyst. At present, these reactions are already utilized in order to solve critical environmental problems. For example, photocatalysis can be used in hydrogen fuel synthesis, which could replace the fossil fuels as energy carriers in the future [1, 2]. H_2 fuel does not produce harmful emissions as it burns to pure water [3]. It has been predicted that in 2050 photocatalytically synthesized hydrogen could cover one third of global energy consumption in an area corresponding to only 1% of the areas covered by deserts [4]. Photocatalysis is also utilized in water purification to remove organic pollutants, offering a solution to the increasing water shortage [5, 6].

Photocatalysts are semiconductor materials which can absorb a photon with sufficient energy and create an electron-hole pair. All semiconductors however, are not suited for photocatalysis due to unsuitable electronic band structures or instability. Nevertheless, titanium dioxide (TiO_2) has shown great potential in photocatalytic applications [6]. TiO_2 is a cheap and chemically stable material, which has a favorable band structure for water splitting reactions, making hydrogen and oxygen evolution reactions energetically favored [7].

TiO_2 is still not optimal material for photocatalysis. The largest flaw of TiO_2 is that it can only absorb high-energy photons which are in the UV range, having a wavelength lower than 400 nm. As seen in Figure 1, UV-light (colored in blue) constitutes only a small fraction of the solar spectrum. This causes a loss of 95% of the solar radiation reaching the surface of the Earth [8]. TiO_2 has also a high recombination rate which limits its use in photocatalysis [6].

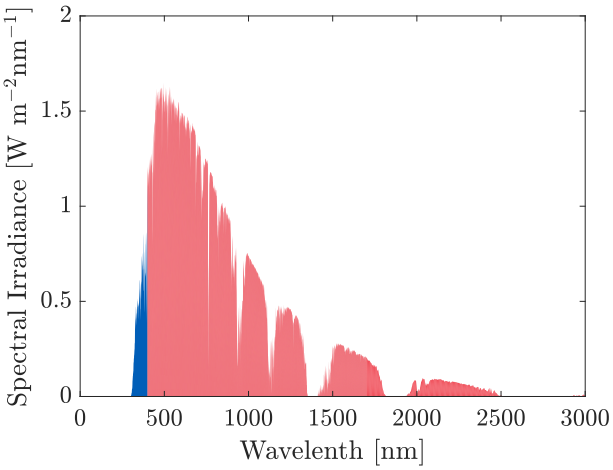

Figure 1: Solar radiation spectrum. The blue area indicates wavelengths shorter than 400 nm, which only accounts for around 5% of the total solar radiation reaching the surface of Earth.

Because of these features of TiO_2, there is a need for stable and more efficient photocatalysts which can absorb a wider range of the solar spectrum. The semiconductors which could absorb longer wavelengths of light are typically unstable in the harsh environments in which photocatalysis occurs [9]. However, there are two commonly used methods to improve the performance of semiconductors in photocatalysis. First, the surface of unstable semiconductors with large absorption range can be passivated to increase stability in photocatalysis. Multiple researches have proven that a thin TiO_2 layer passivates and protects the semiconductor surfaces efficiently, still allowing the photocatalytic reactions to occur [10–15]. The second method is to deposit a cocatalyst on the semiconductor surface. The cocatalyst participates in the photocatalytic reaction by decreasing its activation energy or by facilitating the movement of photogenerated charge carriers [16]. Cocatalysts utilized in photocatalysis are typically noble metals, such as platinum and gold [1].

Noble metal cocatalysts can be deposited on the semiconductor surface with multiple methods such as electrodeposition [17], sputtering [18], impregnation [19] and physical mixing [20]. However, a method called photodeposition has lately shown promise towards cocatalyst deposition. Even though the method was already demonstrated in 1965 [21] and the first platinum catalysts were deposited in 1978 [22], interest towards photodeposition has increased dramatically during the last 15 years, as can be seen from the number of publications related to photocatalysis (Figure 2). In photodeposition, a semiconductor is illuminated and electron-hole pairs are generated. The photogenerated charge carriers react with metal-ions adsorbed onto the surface of the semiconductor, causing a reduction or oxidation reaction. Photodeposition is an attractive deposition method for cocatalysts, since it does not require high temperatures or an applied electrical bias, allowing efficient particle deposition with simple setups. Photodeposition also allows the control of geometrical distribution by using masks, because the reactions occur only under illumination [23].

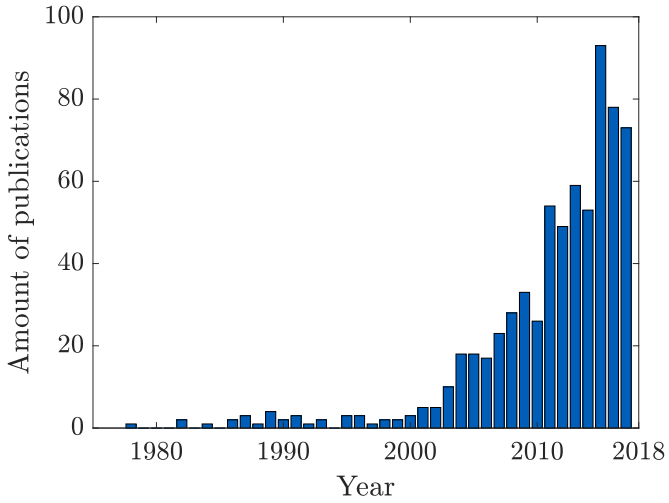

Figure 2: The number of publications available in Scopus database with a search term "photodepo* AND photocat*", searched on the 5th of September, 2017. Figure updated and recreated from reference [23].

In this thesis, gold and platinum are photodeposited on glass substrates coated with a thin TiO_2 layer. This thesis aims to determine the effect of selected photodeposition parameters on the deposited nanoparticles. The goal is to achieve a densely packed area of nanoparticles with diameters less than 20 nm. The nanoparticles are characterized based on their size, surface density and nearest neighbor distances since these properties significantly affect the catalytic properties of the particles. In order to fully demonstrate the effectiveness of photodeposition, the particles in this thesis are deposited only by UV-illumination, and no heat or electricity is applied.

This thesis is organized as follows. In Chapter 2, the structure and properties of titanium dioxide are introduced. The use of TiO_2 in photocatalytic applications is discussed, and possible improvements to the photoactivity of TiO_2 are presented. Chapter 3 describes the photodeposition process. Relevant process parameters are also introduced and discussed based on the literature. In Chapter 4, the specific photodeposition procedure and materials used in this thesis are described. In Chapter 5 we present and discuss the obtained results. Lastly in Chapter 6, conclusions are provided based on the results.

2 Properties and applications of titanium dioxide

Titanium dioxide or titania (TiO_2) is a widely studied material in the field of photocatalysts. It was utilized already in the first experiments of electrochemical photolysis of water by Fujishima in 1972 [24]. This chapter focuses on the structure of TiO_2 and the influence of defects to the behavior of the material. The use of TiO_2 in photocatalysis as a light absorber and as a protecting layer is also discussed.

2.1 Structure of titanium dioxide

In this section, two of the most common crystal structures of TiO_2 are presented and their differences are discussed. The most common fabrication methods for TiO_2 thin films are listed with special attention towards atomic layer deposition.

Titanium dioxide is a natural oxide of titanium. The titanium and oxide atoms can be arranged differently in the TiO_2 lattice, forming various crystal structures. TiO_2 has two common crystal structures called rutile and anatase, which are presented in Figure 3. Both structures consist of repeated octahedrons where a single Ti^{4+} is surrounded by six O^{2-} ions [25]. Differences between anatase and rutile phases arise from different distortions and assembly patterns. Different structures lead to differences in mass densities and electron band structure, causing typical behavior for both structures [9]. For example, anatase has a larger surface area which is beneficial for reactions that occur on the TiO_2 surface [7]. On the other hand, the rutile phase is more thermodynamically stable and kinetically favored in high temperatures (over 600°C) [7]. Rutile TiO_2 is also the favored structure with larger particle sizes, whereas anatase becomes the stable structure for particle sizes smaller than 15 nm [26]. As Figure 3 illustrates, rutile and anatase lattices are asymmetric in [010] and [100] or [001] directions. For both allotropes, the differences in lattice parameters for these directions lead to anisotropic properties [27, 28]. In addition to crystalline phases, TiO_2 can exist in amorphous form which has no long-term periodicity in the lattice.

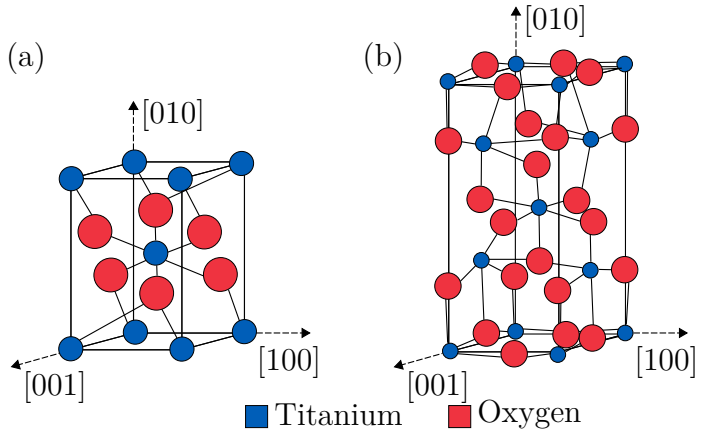

Figure 3: Structures of two typical TiO_2 crystals: (a) rutile (b) anatase.

TiO_2 is not an excellent electrical conductor nor insulator, making it a semiconductor. TiO_2 is an n-type semiconductor, since the electrical conduction occurs mainly

due to electron movement in the lattice. All of the TiO_2 crystal structures experience n-type conduction, even though the structure affects the electrical properties. Both anatase and rutile phases have also a large band gap, meaning that there is a large energy difference (band gap) between the top of the valence band and bottom of the conduction band. The band gap of TiO_2 is dependent on the crystal structure, changing between 3.23 and 3.02 eV for anatase and rutile, respectively [29]. For amorphous TiO_2, the band gap is even larger at 3.66 eV [30]. The width of the band gap is an important quality because it determines the minimum photon energy that a semiconductor can absorb. Photon energy E is dependent on the wavelength of light according to

$$E = h\nu = h\frac{c}{\lambda}, \tag{1}$$

where h is the Planck constant, ν is the frequency of the light, c is the speed of light and λ is the wavelength of the light [31]. From Equation 1 it can be deduced that the maximum wavelengths which are absorbed by anatase and rutile are around 384 nm and 411 nm, respectively. When a semiconductor absorbs a photon, it excites an electron from the valence band to the conduction band, resulting in an excess electron in the conduction band and an empty state (hole) in the valence band. This photogenerated charge carrier pair increases the amount of free carriers in the material.

The activity of TiO_2 towards surface reactions is not only affected by the crystal structure, but also the lattice orientations. For example, the {100} facets of anatase TiO_2 are more active than {001} and {101} facets [32]. Surface orientations also influence the surface energies of TiO_2 which leads to changes in the surface stability and reactivity [33]. The reactivity differences are observed during metal deposition, since metal particles are more likely to be deposited on the more reactive facets of TiO_2. The preferred deposition of materials on certain facets depends on the intrinsic surface charge [34, 35]. Intrinsic surface charges cause facets to have charge differences, resulting in the preferred adsorption of negatively charged metal ions to the more positive facets.

TiO_2 films can be fabricated by multiple deposition methods, including chemical vapor deposition (CVD) [36], sol-gel [37], sputtering [38], spray pyrolysis [39], liquid phase dispersion [40], and atomic layer deposition (ALD) [41]. Atomic layer deposition is one of the most intriguing methods, allowing thin film growth with great conformality and nanoscale thickness control [42]. In addition, ALD can be used to control the crystal structure of TiO_2 film by changing the deposition temperature. At low deposition temperatures (around 150 °C), TiO_2 is produced in amorphous form. If the TiO_2 film is deposited at temperatures of 200–300 °C, anatase is the most dominant phase, and with even higher temperatures rutile formation will take place [43]. In addition to the process temperatures, substrate selection also affects the growth of ALD-grown TiO_2. Crystal orientation of TiO_2 is dependent on the crystalline orientation and morphology of the substrate. The substrate can restrict the growth of TiO_2 crystallites, thereby determining the grain size of a deposited film [43].

2.2 The effects of defects

In this section, defects and their effect on the properties of TiO_2 are discussed. The focus is in the changes of electrical structure and surface properties caused by point defects in particular. At the end, a summary of defect synthesis methods is presented.

In reality, the TiO_2 lattice is never perfect because of various defects which complicate the structure. Lattice defects can be point defects, line defects, or planar defects. Based on previous studies, point defects have the most profound influence on the physical and electrical properties of TiO_2. TiO_2 lattice can contain multiple types of point defects, the most typical point defects being oxygen vacancies, and Ti^{3+} and Ti^{4+} interstitial atoms [44]. Because of the density of oxygen vacancies in TiO_2, titanium dioxide is actually a nonstoichiometric compound TiO_{2-x} in which x is approximately 0.01 [45, 46].

The properties of TiO_2 depend greatly on the lattice defects which are present in the bulk and the surface of TiO_2. The influence of defects to the material properties is greatly determined by their particular location. Surface defects are proven to serve as active sites for reactions [47], whereas intrinsic defects in the bulk modify the optical and electrical properties of TiO_2, changing its color from transparent to dark blue and resulting in n-type doping [48]. N-type semiconducting structure is created because the bulk defects enable the electron movement in the TiO_2 lattice. Both oxygen vacancies and Ti^{3+} interstitial atoms contribute to the n-type conductivity. Oxygen vacancies increase the electrical conduction by trapping electrons at defect states and donating them to the conduction band [49, 50]. Ti^{3+} atoms increase the n-type conductivity because of their ability to act as negative charge carriers compared to stoichiometric Ti^{4+} atoms [51].

Oxygen vacancies are caused by missing oxygen atoms in the TiO_2 lattice which leads to the redistribution of excess electrons around the vacancy sites. The redistribution of electrons occurs to minimize the energy used in the vacancy formation, causing one or two electrons to be localized in an oxygen vacancy state [52]. These electrons alter the electronic structure of TiO_2 and form defect states of which energy lies below the conduction band [53]. The defect states can participate in the electron excitation process by creating intermediate energy states in the band gap of the semiconductor, as shown in Figure 4. The intermediate defect states enable the absorption of lower energy photons [47]. The electrons in the defect states are then easily donated to the conduction band by thermal excitation. The redistribution of electrons in the oxygen vacancies also forms Ti^{3+} defects, as the electrons in the oxygen vacancies interact with surrounding Ti^{4+} [54]. Ti^{3+} defects affect the behavior of TiO_2 similarly as the oxygen vacancies, for example by creating defect states below the conduction band [47].

Oxygen vacancies promote charge transfer between TiO_2 phases. This has been credited to the formation of intermediate energy states below the conduction band [55]. The electron transfer efficiency between anatase and rutile depends on the ability of electrons to overcome the energy difference between the two conduction bands. Localized energy states below the conduction band of anatase matches the energy state with the conduction band of rutile, allowing easier electron transfer between

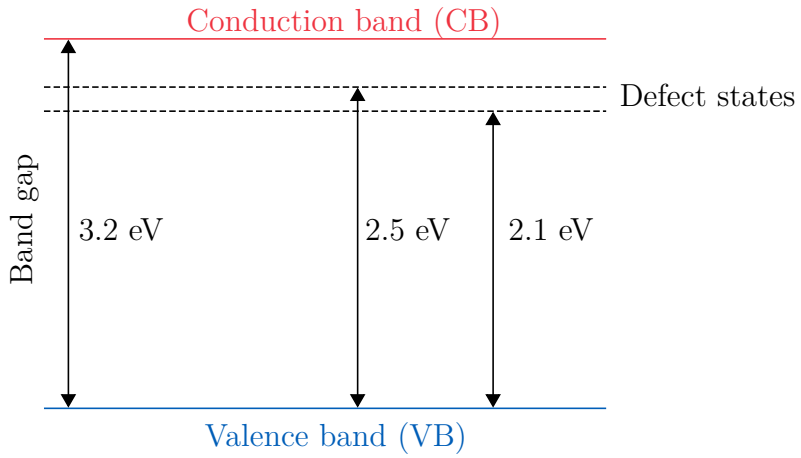

Figure 4: Band structure of TiO_2. Oxygen vacancies create defect states below the conduction band, allowing the absorption of lower energy photons.

the phases [55]. Without the vacancy states, the energy gap would be larger, and the transfer of low energy charge carriers would be hindered.

Oxygen vacancies also act as electron traps leading to a decreased recombination rate and a prolonged charge carrier lifetime [56]. Recombination is a competing process for charge transfer, in which electron-hole pairs are eliminated and thermal energy is released [9]. It can take place on the surface or in the bulk of the semiconductor. Recombination occurs at high rate in TiO_2 but can be decreased by electron trapping. Electron traps separate the photogenerated charges efficiently which increases the carrier lifetime [57]. With increased lifetime, charge carriers are more likely to reach the TiO_2 surface and participate in the surface reactions. Trapping of electrons is based on the charge difference between the oxygen ions (O^{2-}) and oxygen vacancies in the TiO_2 lattice. Oxygen vacancies have a divalent positive charge compared to oxygen ions, allowing the capturing of photoinduced electrons [56]. Especially surface defects are proven to be efficient electron traps while bulk defects are more likely to serve as recombination centers [56, 58]. Reports that claim the opposite also exist, proposing that the recombination occurs specifically at the surface trapping sites [59].

Oxygen vacancies also affect the surface properties of TiO_2. Oxygen vacancies on the surface can be utilized as active sites for reduction reactions involving metal ions. Metal particles are more easily reduced at oxygen vacancy sites due to their high electron density and higher adsorption energy [60, 61]. The positive metal ions are more likely to be attracted to the vacancies with high electron density. The surface electrons in TiO_2 can then participate in a reduction reaction with the adsorbed species. The amount of electrons available for the reduction reactions can be increased by electron excitation, such as UV-illumination. However, the metal reduction reactions can occur also spontaneously without any external electron excitation if the semiconductor surface is highly defected [62].

Bonds between oxygen vacancies and gold have especially intrigued researchers. Oxygen vacancies act as active nucleation sites for gold particles due to a high

adsorption energy, creating a stronger bond between TiO_2 and noble metal [61]. If TiO_2 surface is stoichiometric, Au-TiO_2 bond is formed from the polarization of the atoms [63]. Polarizated bonds are formed when electrons of gold and oxygen atoms are redistributed, causing the formation of positive and negative areas creating an electrostatic attraction. These polarized bonds are weak compared to Au-Au bonds, leading to creation of larger Au particles with small adhesion to TiO_2 surface. Existence of oxygen vacancies in the lattice changes the dynamics of the bonds, as demonstrated in Figure 5. On a defected surface, a single Au atom is in its most stable configuration when it is adsorbed to an oxygen vacancy, forming a covalent bond with minimal charge transfer [63]. When the amount of Au atoms is increased, the dynamics of Au-TiO_2 bonding changes, since individual oxygen vacancies cannot stabilize larger metal clusters. A single oxygen vacancy can bind approximately 3 to 5 gold atoms to itself, making larger metal clusters more unstable [63]. When the size of the cluster increases, a single oxygen vacancy cannot stabilize it, and diffusion occurs. During diffusion, the vacancy-cluster complex can cross paths with another metal cluster or a vacancy site. When two clusters confront each other, a larger cluster is formed that continues to diffuse. If the complex faces a vacancy site, for example at step edges, it can be stabilized on the surface. [63] As a consequence, larger metal clusters are more likely to be found at areas with high oxygen vacancy concentration.

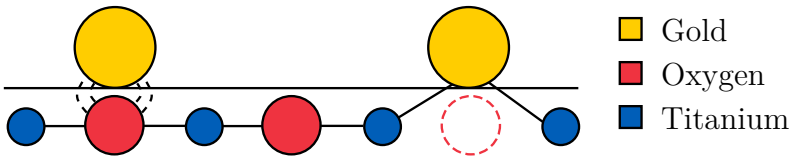

Figure 5: Schematic figure of interactions between gold atoms and TiO_2. A weak polarized bond is formed between stoichiometric TiO_2 surface and gold atom (left). An oxygen vacancy allows the forming of covalent bonds between TiO_2 and gold (right).

Stoichiometric TiO_2 can be easily reduced by creating oxygen vacancies. Synthesis of oxygen vacancies is a highly studied subject, and multiple solutions have been proposed. The five most commonly used methods are heat treatment, particle bombardment, plasma treatment, doping and vacancy generation under reaction conditions. The control of the created oxygen vacancy densities and the process conditions differ between these methods.

Heat treatment to introduce oxygen vacancies to TiO_2 lattice is conducted in a reductive atmosphere. Typically, hydrogen atmosphere is used. In H_2 thermal treatment, hydrogen atoms interact with the adsorbed oxygen and donate electrons to it, creating H_2O molecules and oxygen vacancies to TiO_2 [47]. The creation of oxygen vacancies can be controlled by the reaction temperature. Liu *et al.* [64] propose three types of temperature dependent interactions that occur during H_2 heat treatment:

1. At temperatures below 300°C, hydrogen interacts with adsorbed oxygen in the TiO_2 lattice.

2. At temperatures over 300°C, electron transfer occurs from hydrogen to oxygen atoms. H_2O is formed and oxygen vacancies are left in the lattice.

3. At temperatures over 450°C, electrons are transferred from hydrogen atoms to TiO_2, forming Ti^{3+} defects from stoichiometric Ti^{4+}.

High temperature annealing can also create oxygen vacancies in the absence of H_2. Oxygen vacancies can be synthesized by oxygen deficient annealing of TiO_2 at temperatures higher than 400°C in He [47], N_2 [65], Ar [66] or vacuum environment [67]. The concentration of created vacancies increase with decreasing O_2 pressure [47]. However, the vacancies created with this method are unstable, and the reaction is reversible even at room temperature [68]. All of the heat treatments are conducted in elevated temperatures which limits the selection of the substrate.

Another way to create oxygen vacancies to the TiO_2 lattice is to bombard it with electrons or ions [69, 70]. When accelerated particles interact with the lattice they desorb neutral atoms and oxygen ions from the surface. Electron bombardment at moderate energies (around 500 eV) causes only small damages to the surface, and it exclusively produces oxygen vacancies [67]. Because of the moderate energy used, vacancies produced by electron bombardment are localized only in the surface region [65].

Instead of electrons, argon ions (Ar+) can be accelerated on TiO_2 surface to create oxygen vacancies [61]. Ion bombardment is a more aggressive method than electron bombardment and it is done with higher energies (around 1000 eV) [67]. Unlike electron bombardment, argon ion sputtering leads to creation of oxygen vacancies in both the bulk and surface of TiO_2 [65].

The third way to create oxygen vacancies is plasma treatment. Plasma is defined as ionized gas that contains freely moving ions and electrons, and it can be produced by applying electrical discharges through gas [71]. Plasma treatment creates oxygen vacancies to the TiO_2 lattice if it is done in reducing atmosphere (typically in H_2) [53, 72, 73]. Reaction occurs due to highly reactive and unstable high-energy radicals, electrons and ions that are present in the plasma [47]. These particles are much more reactive than the molecular precursors used in thermal treatments. Plasma treatment allows careful control of the oxygen vacancy content since the vacancy concentration increases with increasing treatment time [74]. Plasma treatment requires a lower processing temperature compared to the thermal treatments. Because of the mild conditions, the created oxygen vacancies are formed mostly on the surface layer of TiO_2 instead of the bulk [47].

Oxygen vacancies can be introduced to the lattice also by impurity atoms. TiO_2 can be doped with other metal or nonmetal ions in order to create oxygen vacancies. Oxygen vacancies are introduced to the lattice when doping with cations that have lower valance than Ti^{4+} (for example trivalent cations M^{3+}) [75]. Fe^{3+} is a typical metal ion used in oxygen vacancy creation [68], whereas fluorine [76] and nitrogen ions [77] are typical nonmetal dopants.

Lattice oxygen can also participate in a reaction occurring at the TiO_2 surface. An oxidation reaction consumes the oxygen atoms from the TiO_2 structure and produces surface oxygen vacancies [78]. The oxidated species is typically an organic compound, such as dimethyl methylphosphonate. The variety of options for oxygen vacancy creation increases the range of available materials and fabrication methods for processes in which the properties of reduced TiO_2 would be beneficial.

2.3 Titanium dioxide as a photocatalytic material

The focus of this section is in photocatalytic reactions. First, the phenomenon of photocatalysis is explained, followed by introductions to photoelectrochemical cells, and photochemical air and water purification. The potential of TiO_2 as a photocatalyst is discussed. Finally, methods for improving photocatalytic efficiency are presented.

Photocatalytic materials can absorb light, creating an electron-hole pair which then drives a reaction that occurs on the surface of the photocatalyst. Generally, catalysis is defined as an action in which the reaction rates of chemical reactions are affected by a catalyst material [79]. Catalysis consists of five separate reactions: transfer of reactants to the surface, reactant absorption, reaction, product desorption and transfer of products away from the interface [7]. The difference between classical catalysis and photocatalysis is that photocatalytic reaction is activated by photon absorption, whereas classical catalysis is activated thermally. TiO_2 has been extensively studied as a photocatalytic material ever since it was found to have the ability to split water [24]. Currently, TiO_2 is used as a material for photocatalysis in multiple applications, such as the production of renewable fuels [80], air purification [81] and water decontamination [82].

Water-splitting is one of the most intriguing applications for photocatalytic materials. Water-splitting reactions can be conducted in a photoelectrochemical cell (PEC), which uses solar energy to produce hydrogen (H_2) and oxygen (O_2) in a clean and safe process. Hydrogen can be used as a renewable fuel to decrease carbon emissions generated by the growing energy production [83]. The basic structure of PEC consists of an electrolyte solution and two electrodes which are connected with a conductive wire, as shown in Figure 6. One or both of the electrodes are fabricated from a photoactive material. The photoactive electrode(s) absorb sunlight generating electron-hole pairs. The negative electrons accumulate on the positive electrode, called a cathode, and the positive holes accumulate on the negative electrode, called an anode. The electrodes are immersed in the electrolyte solution. The electrolyte solution contains the chemical species which participate in the oxidation and reduction reactions on the surfaces of the anode and cathode, respectively. In PECs, the electrolyte solution is water with added salts to increase its the electrical conductivity. The electrical conductivity in the electrolyte is needed to achieve a flow of current in the system [84].

The operation of PEC is based on the photoactivity of semiconductors. A photoactive semiconductor acts as a photocatalyst, absorbing photons with equal or greater energy than its band gap energy and creating electron-hole pairs [7]. Photogenerated

charges participate in oxidation reactions (holes) or reduction reactions (electrons). These reactions take place on anode and cathode, respectively, and can be expressed as

$$2\,H_2O + 4\,h^+ \longrightarrow O_2 + 4\,H^+, \tag{2}$$
$$2\,H^+ + 2\,e^- \longrightarrow H_2. \tag{3}$$

Holes on the photocatalyst surface oxidize donors (O^{2-}) to O_2 gas by combining with an electron of a water molecule, dissociating it to an oxygen molecule and hydrogen ions. Electrons, on the other hand, reduce electron acceptors (H^+), formed in the water oxidation reaction, to H_2 gas. [3] If the anode and cathode are separated in the PEC, as seen in Figure 6, the O_2 and H_2 gases are formed on different sides of the cell, facilitating gas separation [83].

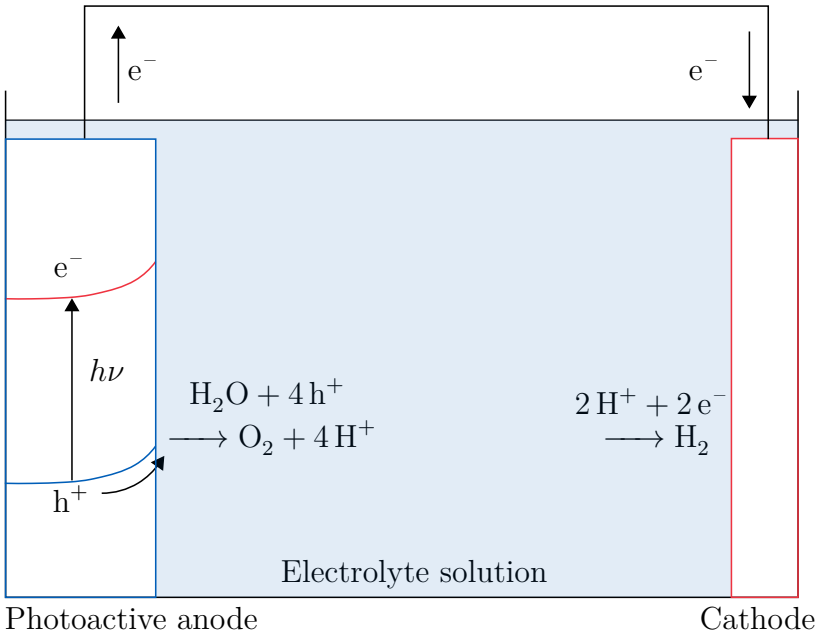

Figure 6: Schematic figure of a photoelectrochemical cell with photoactive anode. The positive holes accumulate at the anode whereas the negative electrons are driven to the cathode.

Other intriguing applications for photocatalytic TiO_2 are air purification [85] and water purification [5]. This photocatalytic purification allows the removal of organic compounds from air and water by using either sun light or UV-light as the source of energy. Air and water purification rely on similar principles as photocatalytic water splitting. In all of these cases, the photocatalyst is illuminated, and the absorbed photons generate electron-hole pairs. The photogenerated electrons and holes participate in reduction and oxidation reactions, respectively. The reactions caused by the charge carriers differ in water splitting and purification applications. In air and water purification, the photogenerated holes participate in an oxidation reaction in which the holes react with water molecules and create active hydroxyl

radicals ($OH^{\bullet}$). These radicals then react with organic compounds, decomposing them into carbon dioxide and water [5, 85]. The photogenerated electrons, on the other hand, are scavenged by oxygen molecules forming O_2-radicals.

TiO_2 has excellent properties that make it accessible to photocatalytic reactions. All phases of TiO_2 are chemically and thermally stable, as well as Earth-abundant and non-toxic but highly photosensitive and resistant to photocorrosion [29, 47]. However, anatase is often the preferred allotrope because it is chemically more active than rutile. The higher activity results from a higher surface area and longer carrier lifetime [7, 73]. The higher activity of a material is beneficial since it determines the reaction kinetics and the efficiency of the reactions. TiO_2 has also a suitable band structure for water splitting reactions, meaning that the bottom level of the conduction band is more negative than the redox potential of H_2 evolution, and that the top of the valence band is more positive than the redox potential of water oxidation (O_2 evolution), as seen in Figure 7. This band structure allows the spontaneous charge transfer from conduction and valence bands to H_2 and O_2 evolutions, respectively.

A large disadvantage of TiO_2 is the large band gap, which is 3.23 and 3.02 eV for anatase and rutile, respectively. Amorphous TiO_2 has an even larger band gap of 3.66 eV [30]. Large band gap limits the light absorption range to the UV region (wavelengths shorter than 400 nm) of solar radiation, corresponding to only around 5% of the available solar spectrum, as shown in Figure 1 (see p. 1) [29]. TiO_2 is still used as a photocatalyst even though small-band gap semiconductors could absorb a larger range of the visible light spectrum. The problem with small-band gap semiconductors (such as Cu_2O and Si) is that they tend to be unstable and photodegrade over time [9]. The use of TiO_2 as a photocatalyst is also hindered by the high recombination rate of charge carriers and the difficulty to achieve significant improvements in photocatalytic performance [6, 86].

Some improvement can be achieved in photocatalytic efficiency of TiO_2 with oxygen vacancies. As stated previously in Section 2.2, oxygen vacancies introduce shallow donor levels to the electronic band structure of TiO_2. Localized oxygen vacancy states below the conduction band allow the absorption range of TiO_2 to expand [47]. If the localized states are located above the reduction potential of the reducible species, the defect states can be utilized in the reduction reactions. For example, shallow donor levels below the conduction band of TiO_2 are still above the H_2/H_2O redox potential and thus increase the photocatalytic activity of TiO_2 in water splitting reaction [87].

Another way that oxygen vacancies in TiO_2 can improve the photocatalytic efficiency is their role in interfacial electron transfer. Although there are reports that oxygen vacancies can act as recombination centers for charge carriers [88], some studies indicate that they can also function as electron donors, increasing the donor density in TiO_2 surface [55]. More recent studies have shown, that the location of vacancies determines their role in charge interactions [58]. Defects that are located in the bulk are more likely to act as recombination centers [56]. Conversely, TiO_2 surface defects can trap electrons leading to decreased recombination rate.

Recombination rate can be further decreased by extracting photogenerated electrons or holes from the semiconductor surface. In reduction reactions initiated by

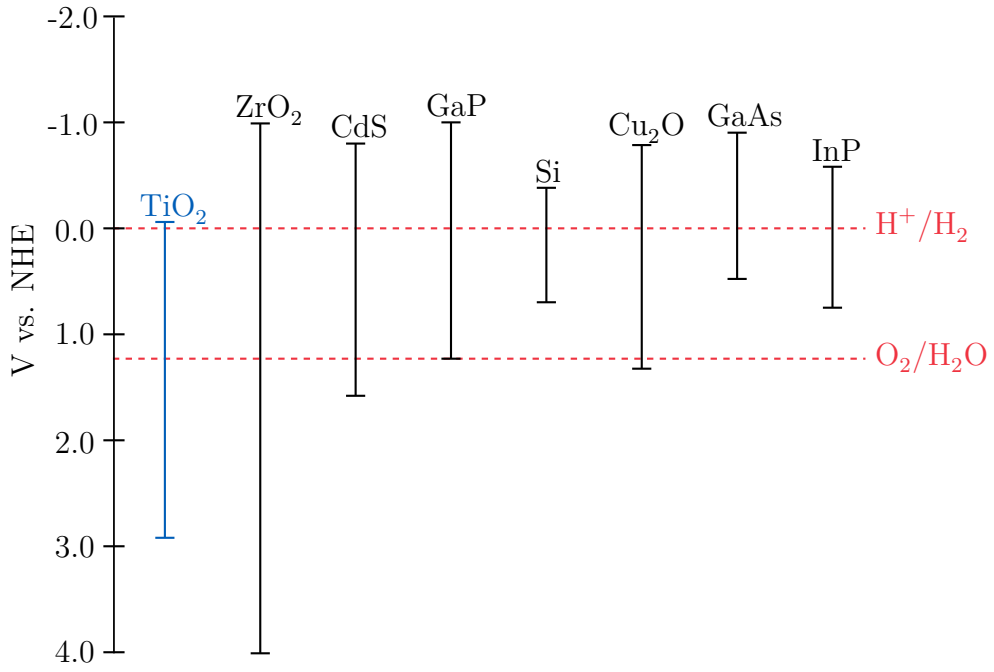

Figure 7: Comparison of semiconductor conduction band and valence band positions to redox potentials of water splitting reactions with normal hydrogen electrode (NHE) at ph 0. TiO_2 conduction band is at a more negative potential than the H_2 evolution reaction, and valence band is at more positive potential than the water oxidation reaction.

electrons, adding a hole scavenger to the electrolyte will remove the excess holes accumulated to the semiconductor surface and decrease the recombination rate [89]. Without a hole scavenger, the photogenerated holes are driven to the TiO_2-electrolyte interface since the electrolyte surface is negatively charged. The negative charge is formed when electrons from the conduction band of the n-type semiconductor, such as TiO_2, are drifted to electrolyte in order to align the Fermi levels of the system. This negative charge of the electrolyte surface attracts positive holes and repulses the negative electrons. The hole scavenger decreases the positive charge at the surface so that electrons are more easily trapped by the surface oxygen vacancies and donated to reduction reactions [47].

Other defects than oxygen vacancies also affect the photocatalytic efficiency of TiO_2. As stated earlier in Section 2.2, interstitial Ti^{3+} ions create donor levels below the conduction band. These donor levels will decrease the optical band gap of TiO_2, enabling absorption of lower energy photons [47]. There are some differences between these two point defects. Ti^{3+} defects are proven to be less stable than oxygen vacancies [64]. Air can oxidize Ti^{3+} defects located in the surface of TiO_2, restoring the stoichiometry [64, 90]. Thus, a more permanent improvement in photocatalytic activity is achieved with oxygen vacancies.

Photocatalytic efficiency of TiO_2 can be increased by adding a catalyst for the photocatalytic reaction. Typically, noble metals are utilized as the cocatalyst for photocatalytic reactions. In air and water purification, gold and platinum are utilized

to capture photogenerated charge carriers [5]. For water splitting, the most common cocatalysts for H_2 and O_2 evolutions are platinum (Pt) and ruthenium oxide (RuO_2), respectively [91]. A schematic of the water splitting reactions over a semiconductor particle loaded with cocatalysts is presented in Figure 8.

There are three ways in which cocatalysts can improve the activity and reliability of the photocatalyst. Firstly, the efficiency of the reactions can be increased by lowering the activation energy of H_2 or O_2 evolution [16]. Active sites are needed especially in H_2 evolution, because many of the metal oxide semiconductors do not have sufficiently high conduction band levels for water reduction [1]. Figure 7 shows the small energy gap between the energy levels for TiO_2 conduction band and H_2 evolution. Because of the decreased activation energy, the reactions occur more likely at these active sites where cocatalysts are present [91].

Secondly, cocatalyst can promote the charge separation at the semiconductor-cocatalyst interface [16]. Electrons from the conduction band of the photocatalyst are transferred to the cocatalyst for the reduction reaction. Photogenerated holes from the valence band are transported to the cocatalyst for the oxidation reaction. Cocatalyst-semiconductor interface creates a heterojunction (a so-called Schottky junction) that leads to charge separation and a decreased recombination rate [16]. The direction and efficiency of carrier separation is dictated by the Fermi level. The Fermi levels of cocatalyst and semiconductor differ when they are electrically neutral and isolated from each other. When the materials are connected, electrons migrate from higher energy level to lower, in order to align the Fermi levels [9]. If the cocatalyst has lower Fermi level than the semiconductor, the electrons are trapped by the cocatalyst. In Figure 8, the water-splitting reactions are given as examples of the reduction and oxidation reactions. The electrons are then consumed by the reduction reaction. If the electrons are not consumed by the reaction, the cocatalyst becomes negatively charged and carrier mobility decreases [92]. Because of their low Fermi levels, noble metals, such as gold and platinum, have received considerable amount of attention as cocatalysts [93–96]. Especially platinum has been studied extensively, since it possesses the lowest Fermi level among metals, making it the best candidate for electron trapping [91]. On the other hand, the electrons from the Fermi level of the oxidation cocatalyst (RuO_2 in Figure 8) migrate to the valence band of the photocatalyst causing the hole migration to the opposite direction. The holes are trapped by the oxidation cocatalyst and are used in the oxidation reaction.

Thirdly, cocatalysts can increase the stability of a photocatalyst by suppressing photo-corrosion of the photocatalyst [16]. In photo-corrosion, the photogenerated holes will oxidize the photocatalyst resulting in a decomposition of the structure. Photo-corrosion is a problem especially in small-band gap semiconductors [9]. Co-catalysts can extract these photogenerated holes for oxygen evolution and inhibit the decomposition of the photocatalyst [16].

When photocatalytic activity is improved with cocatalysts, the particle size and loading amount of the cocatalyst should be carefully considered. Particle size of the cocatalyst should be small (around 10 nm) for it to function efficiently [60]. Larger particles on photocatalyst surface shadow the photoactive sites, decreasing the light absorption at the semiconductor surface. With increasing particle size, the cocatalyst

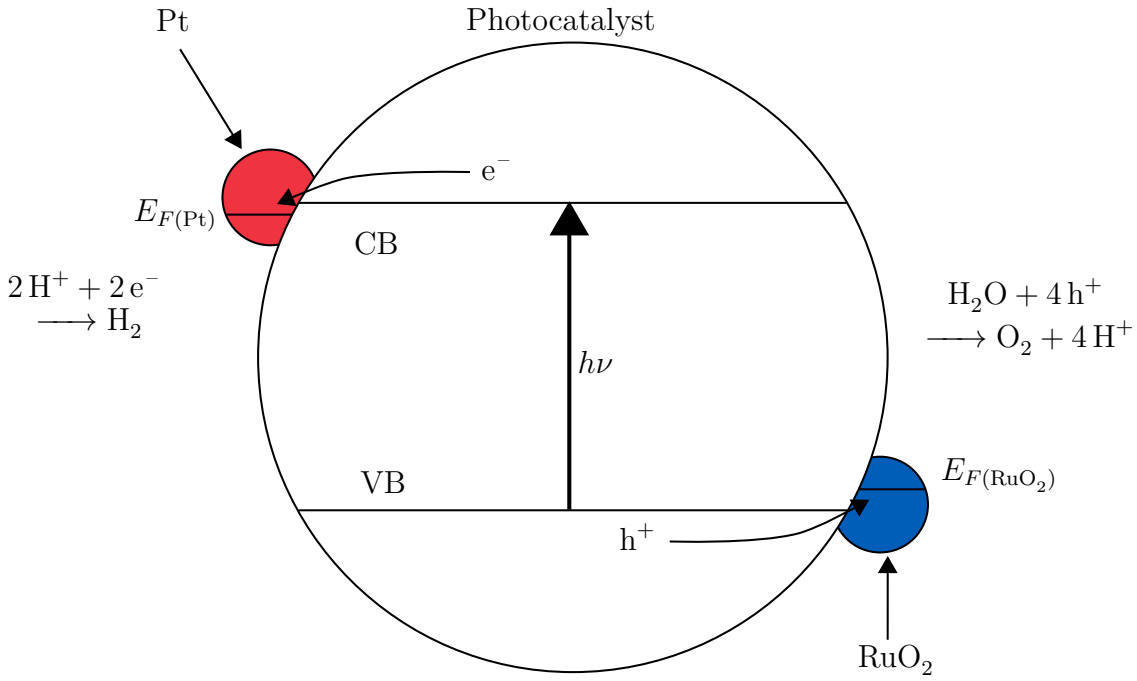

Figure 8: Schematic figure of photocatalytic reactions over a photocatalytic semiconductor with platinum and ruthenium dioxide cocatalysts deposited for H_2 and O_2 evolutions, respectively. The charge trapping is based on the Fermi level differences of the cocatalysts and the photocatalyst. Platinum has a lower Fermi level ($E_{F(\mathrm{Pt})}$) than the photocatalyst leading to electron trapping in the Pt cocatalyst. Ruthenium dioxide has higher Fermi level ($E_{F(\mathrm{RuO_2})}$) than the valence band of the photocatalyst so the holes are trapped in RuO_2 cocatalyst.

is also more likely to serve as a recombination center for charge carriers instead of acting as a beneficial electron trap. [29] Similar results have also been demonstrated with increasing cocatalyst mass. The influence of increasing cocatalyst loading to photocatalytic efficiency of TiO_2 particles was studied by Reichert *et al.* [97]. They found out that the smallest measured cocatalyst loading of 0.17 wt-% resulted in the highest activity. The increased loading has shown to increase the particle size hindering the photocatalytic activity [16, 97].

2.4 Titanium dioxide as a passivation layer

In this section, the potential of TiO_2 as a passivation layer for other photocatalytic materials is discussed. The reasons for using a passivation coating on a small-band gap semiconductor are presented and justified based on the literature survey. Finally, the fabrication of thin TiO_2 layers is discussed.

The efficiency of a photocatalyst can be improved by broadening the light absorption range. This can be achieved by utilizing small-band gap semiconductors as photocatalysts. Photocatalysis typically occurs in a liquid phase, so the semiconductor must be stable in aqueous environments and under highly oxidative potentials

needed for the chemical reactions to occur [10]. As stated previously in Section 2.3, typical small-band gap semiconductor materials do not satisfy these conditions. In order to stabilize the semiconductor, a thin protective layer can be deposited to passivate the surface.

Various studies have shown, that TiO_2 possesses multiple promising qualities as a passivation layer for small-band gap semiconductors. TiO_2 has the correct band structure as an n-type oxide, which allows the flow of electrons so that it does not electrically insulate the underlying semiconductor [11]. In water splitting reactions, the band structure also allows the hydrogen evolution to be the favored reaction on the electrolyte surface [11]. A passivating TiO_2 layer can also improve the photocatalytic efficiency of the photocatalyst by decreasing the recombination rate [98]. The amount of recombination sites is reduced as TiO_2 layer passivates the trap and defect sites in the photocatalyst surface.

TiO_2 has been shown to increase the stability of multiple promising small-band gap photocatalytic materials. On Cu_2O, the photocurrent has been shown to drop only 22% after 20 min with the help of a 11 nm thick TiO_2 layer, and actually it would be already nonexistent without the passivation layer [11]. For a Si-based photoanode, a 2 nm TiO_2 layer extended the operation time from 30 min to at least 24 h and inhibited the growth of an insulating silicon dioxide layer [12]. Encouraging results have also been obtained with TiO_2 passivation of InP nanopillar photocathodes [13], GaAs and GaP photoanodes [14], as well as phosphate-based catalysts [15]. In addition, TiO_2 passivation layers are known to increase the sample lifetime significantly in both acidic and basic solutions [12].

A passivating film has to be extremely thin for it to function properly. Precise thickness control of the passivating layer is needed so that the migration of the charge carriers to the solution interface is possible. TiO_2 layer thickness determines the mechanism that transports the charge carriers through it [12]. For extremely thin (< 2 nm) passivating TiO_2 layers, the charge transportation occurs through tunneling. With thicker oxides (> 4 nm) current densities show a more pronounced temperature dependency which can be credited to more thermally-active conduction mechanisms like trap-assisted tunneling and Frenkel-Poole conduction. In trap-assisted tunneling, charge carrier traps in the TiO_2 can capture and emit charge carriers, resulting in a tunneling current through the thin layer [99]. Frenkel-Poole conduction results from thermal excitation of trapped electrons to the conduction band of TiO_2 [100]. When the TiO_2 layer thickness reaches 10 nm, efficient tunneling-mediated electron transport starts to become reduced [12].

Passivating TiO_2 coatings are typically deposited by ALD since it is known to produce highly conformal coatings with nanoscale thickness control. If these criteria are not met, the electrical conductivity decreases and resistance towards carrier transport is increased [12, 98]. In addition to creating a passivation layer, a uniform ALD-grown TiO_2 thin film can function as a thin heterojunction separating the photogenerated charge carriers more efficiently [10]. ALD-grown TiO_2 can have a valuable role in photocatalysis even though the photocatalytic properties of TiO_2 are not optimal.

3 Photodeposition of nanoparticles

This chapter concentrates on photodeposition of metal and metal oxide particles for cocatalysts in photocatalytic reactions. The chapter is divided to three sections. First, Section 3.1 describes the phenomena occurring during the photodeposition, and conducts a short discussion on the advantages of photodeposition compared to other cocatalyst deposition methods. The physics of photodeposition are also presented. Then, Section 3.2 examines available photodeposition variables and their influences on the process kinetics. Finally, Section 3.3 describes the photodeposition of cocatalysts relevant in this thesis.

3.1 Theory behind photodeposition

This section describes the photodeposition process, and the reactions that occur take place in there. The efficiency of depositing efficient cocatalysts with photodeposition process is discussed. The phenomena occurring during the photodeposition are thoroughly explained. The section starts with a short summary of cocatalysts in photocatalytic reactions.

Adding cocatalysts is an important way to increase the efficiency of photocatalytic reactions. As discussed in the previous chapter, there are three ways in which a cocatalyst can function in photocatalysis: by decreasing the activation energy of the reactions, by promoting photogenerated charge carrier separation or by improving the stability of the photocatalyst [16]. These beneficial effects are achieved mainly because of efficient charge trapping due to lower energy states of metal compared to the photocatalyst. In order to improve the photocatalytic efficiency and stability, a special consideration towards the cocatalyst deposition is required.

Cocatalysts can be deposited by multiple methods, such as electrodeposition [17], ALD [101], chemical reduction [102], sputtering [18], impregnation [19], physical mixing [20], and photodeposition [23]. Compared to the other methods, photodeposition provides an environmentally friendly alternative for material deposition. Photodeposition is activated by light absorption, whereas other methods typically need applied bias or elevated temperatures. Other advantages of photodeposition are the ability to precisely control geometrical distribution, size and oxidation state of nanoparticles which makes it the prominent method for cocatalyst deposition [23]. Studies have also shown that photodeposited cocatalyst achieve higher photocatalytic efficiencies than cocatalysts fabricated using other deposition methods [20, 103, 104], even though contrary reports also exist [105, 106].

Photodeposition was first performed by Clark and Vondjidis already in 1965 [21], and the first for cocatalyst deposition was demonstrated by Kraeutler and Bard in 1978 [22]. The photodeposition process is activated by light absorption after which electron-hole pairs are created in a photocatalyst. The photogenerated charge carriers are consumed in a reaction with metal ions which are in close proximity to the semiconductor surface. The metal ions are introduced to the system as precursors in a fluid, typically as salts dissolved in aqueous solution. The reactions occur in the illuminated area, so the deposition area can be localized by scanning and focusing of

light [107].

Photodeposition is typically conducted in a liquid form as an aqueous solution, but it can also be done in gaseous or even in solid phase. Liquid-phase photodeposition is a simple process, in which a solution with the cocatalyst precursor is placed on a photocatalyst and illuminated. When working in the liquid phase, the temperatures are typically low and atmospheric pressures are used, enabling the possibility to use even organic materials. Compared to gas-phase photodeposition, liquid-phase deposition has significantly higher deposition rates due to higher precursor concentration. Liquid-phase precursor solutions are also easier to store and keep usable for several years. [107] Gas-phase photodeposition is slower and expensive process but can be used when high purity levels are required. Solid-phase photodeposition has also been demonstrated [108, 109]. In a solid-phase photodeposition process, the sample is first coated with the metal salt and then illuminated to reduce the metal. This thesis concentrates only on liquid-phase photodeposition since it is the most widely used and easiest to conduct.

In liquid phase photodeposition, the precursor salt is dissolved in an aqueous solution. As the precursor dissolves, it forms positive and negative ions in an electrolyte which causes electrical conduction in the solution. Because of these charged ions, the behavior of energy bands in the semiconductor-solution interface is altered, as charge transfer occurs to align the Fermi levels of the semiconductor and the electrolyte. The behavior of the energy bands is demonstrated in Figure 9, in which the Fermi level of the semiconductor ($E_{F,S}$) is adjusted to match the Fermi level of the electrolyte ($E_{F,E}$). The Fermi level of the electrolyte is located at the intersection of two distribution curves D_{ox} and D_{red}, which are similar to the conduction band and the valance band of a semiconductor, respectively. Electron states in electrolyte cannot be described with a band structure, because the electrons in electrolyte are not as free to move as in semiconductors [110]. Instead, the electron energy levels in electrolyte are described with oxidation and reduction states, in which electrons are localized on redox ions. The energy levels are not sharp because they interact with the charge carriers in the solvent, causing the energy levels to fluctuate [110]. This energy level fluctuation causes the possible energy range of the charge carriers to expand. The oxidation state distribution (D_{ox}) gives the energy levels for empty states and reduction state distribution (D_{red}) the energy levels for occupied states. Alignment of the Fermi levels of semiconductor and electrolyte occurs by charge transfer in which electrons from TiO_2 conduction band migrate to the oxidation state of the electrolyte [111].

The electron migration creates a space-charge layer, also known as the depletion layer, to the semiconductor surface in which the majority carriers are depleted. For n-type semiconductor, this causes a surplus of positive charges at the material surface which attracts a surplus of negative charges from the electrolyte. An equilibrium is achieved when the negative ions in the electrolyte solution will repel the electrons at the TiO_2 surface so that the net charge flow is zero. The charge transportation causes upward band bending of the conduction band (CB) and valence band (VB). Band bending occurs because negative ions at the electrolyte interface repel the electron transportation from the semiconductor to the electrolyte [111]. This increases the

energy barrier of the electron transportation which is detected as upward band bending. The amount of band bending is equal to the Fermi level difference between the semiconductor and electrolyte in order to align the Fermi levels at the equilibrium state. The energy difference between the vacuum level (the energy of an electron in free space) and the Fermi level of a material is called the work function (ϕ), and it stays constant for the semiconductor (ϕ_S) and electrolyte (ϕ_E) leading to the bending of the vacuum level energy band.

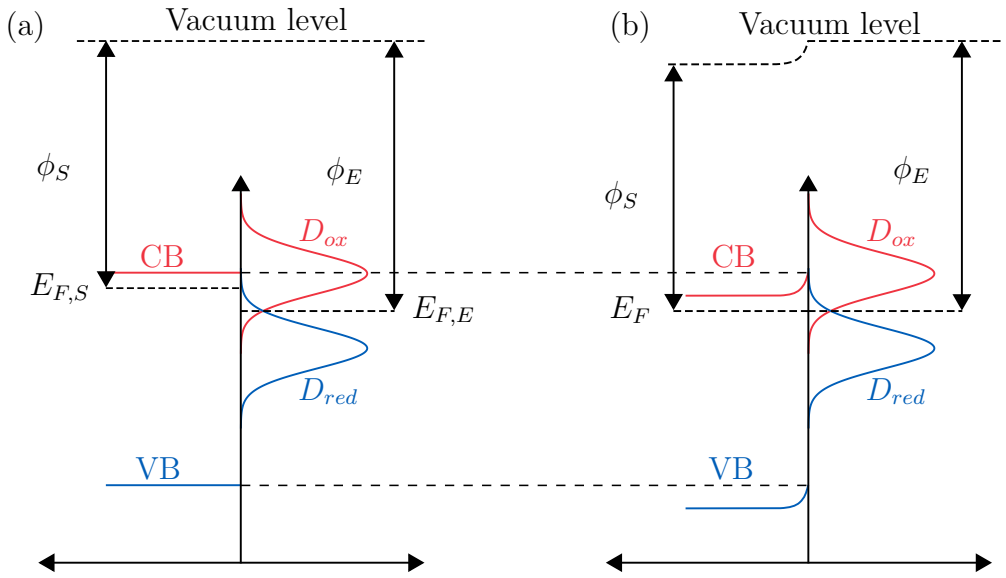

Figure 9: Energy diagram of TiO_2-electrolyte solution interface: (a) before charge transfer, when the Fermi levels are not aligned, (b) at equilibrium state after charge transfer. The Fermi levels have been aligned.

When the Fermi levels are aligned, the system is in thermal equilibrium:

$$np = n_i^2, \tag{4}$$

where n is the electron concentration at the conduction band, p is the hole concentration on the valence band and n_i is the intrinsic carrier concentration. In equilibrium, the recombination rate and the thermal generation rate of electron-hole pairs are equal. Both, n and p, cannot be large or small numbers simultaneously compared to n_i. There either is an excess of electrons (high concentration of electrons in conduction band and low number of holes in valence band) or holes (vice versa) if the concentrations differ from the intrinsic value. Charge carrier concentrations determine the location of the Fermi level

$$p = N_V e^{\frac{-(E_F - E_V)}{k_B T}}, \tag{5}$$

$$n = N_C e^{\frac{-(E_C - E_F)}{k_B T}}, \tag{6}$$

where N_V is the density of states in the valence band, N_C is the density of states in the conduction band, E_F is the Fermi level energy, E_V is the valence band energy,

k_B is the Boltzmann constant, and T is the temperature [110]. From these equations, the position of the Fermi level is solved:

$$E_F = E_V - k_B T \ln \frac{p}{N_V}, \tag{7}$$

$$E_F = E_C + k_B T \ln \frac{n}{N_D}. \tag{8}$$

If Equation (4) holds, the E_F values calculated from Equations (7) and (8) are equal, and the electrons and holes are in equilibrium with each other. For example, in n-type silicon the Fermi level energy is around 0.16 eV below the conduction band for typical values of $T = 300$ K, $n = 1.45 \cdot 10^{10}$ cm^{-3} and $N_D = 6 \cdot 10^{16}$ cm^{-3}.

The energy band structure changes even more when the sample is illuminated and charge carriers are photogenerated. Because of the generation of charge carriers the system is no longer in thermodynamic equilibrium. Illumination creates excess holes in the valence band (p') and excess electrons in the conduction band (n'), so that Equation (4) does not hold [112]. Since a single photon creates an electron-hole pair, the numbers of photogenerated charge carriers are equal:

$$n' \equiv p' \tag{9}$$

Because of the excess carriers, the Fermi level cannot describe both energy bands, and it is divided to two quasi-Fermi levels corresponding to the quasi-Fermi level of electrons (E_{Fn}) and the quasi-Fermi level of holes (E_{Fp}) [111]. The formation of quasi-Fermi levels is illustrated in Figure 10. The positions of the quasi-Fermi levels depend on the electron and hole concentrations under illumination:

$$E_{Fp} = E_V - k_B T \ln \frac{p + p'}{N_V}, \tag{10}$$

$$E_{Fn} = E_C + k_B T \ln \frac{n + n'}{N_D}. \tag{11}$$

In an n-type semiconductor, such as TiO_2, the majority carrier concentration does not increase significantly due to photogeneration of carriers, and the electron quasi-Fermi level E_{Fn} stays practically equal to the equilibrium Fermi level. However, the concentration of the minority charge carriers (holes) experiences a significant increase, and the hole quasi-Fermi level (E_{Fp}) is shifted close to the valence band. The position of the hole quasi-Fermi level depends on the amount of generated holes [110]. The photon absorption and the following charge carrier generation occurs near the semiconductor surface, so the maximum difference between the quasi-Fermi levels occurs close to the semiconductor surface [111]. When going deeper into the bulk, the amount of photogenerated carriers decreases, and the quasi-Fermi levels align.

In photodeposition, the semiconductor is immersed in the precursor solution under illumination. Both of the above-mentioned concepts, band bending and formation of quasi-Fermi levels, take place simultaneously. The charge carrier photogeneration occurs at the surface of the semiconductor in which the energy bands are bent, as

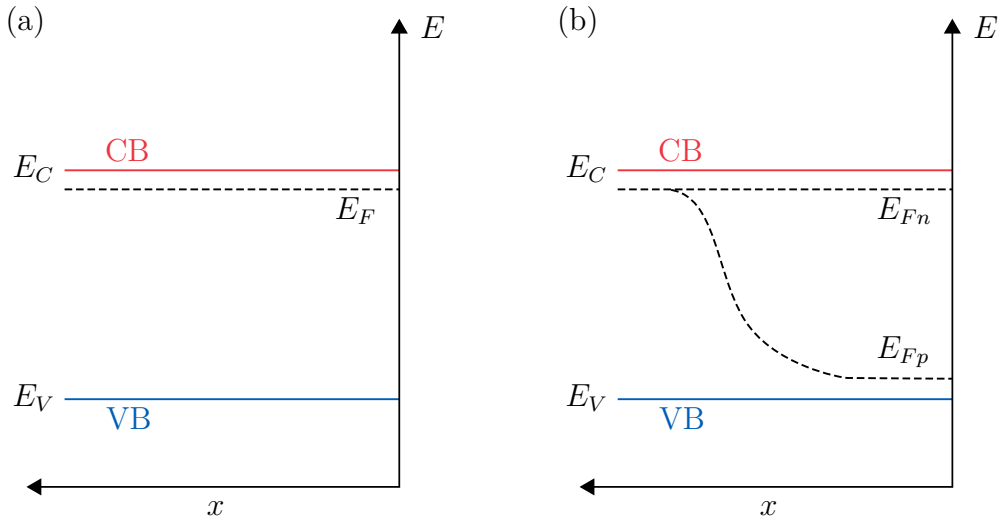

Figure 10: The Fermi level of TiO_2 (a) in equilibrium state (b) under illumination. When illuminated, the photogeneration of charge carriers occurs at the surface, leading to creation of quasi-Fermi levels (E_{Fn} and E_{Fp}). The photon absorption and carrier photogeneration occurs near surface, so the Fermi levels unite and equilibrium condition holds deeper into the structure.

illustrated in Figure 11. The upward band bending in TiO_2, due to the potential gradient at the interface, drives the photogenerated electrons towards the bulk and holes to the surface of the semiconductor [111]. The holes are available for oxidizing reaction at the interface if there is a suitable redox species adsorbed to the surface. The oxidizing power of the photogenerated holes is determined by the position of hole quasi-Fermi level [110]. Similarly, the electron quasi-Fermi level determines the reduction power of electrons. Electrons can participate in reduction reactions at the semiconductor surface if they are transferred to electron acceptors or if they are trapped by shallow traps [89]. Electrons in shallow traps can be thermally excited to conduction band from which they can be trapped by another shallow trap, leading to more efficient charge transport [113]. As stated previously in Section 2.2, oxygen vacancies have a large role in electron trapping at the TiO_2 surface [56].

If the migration of the charge carriers is not efficient or they are trapped in deep traps, charge carriers will recombine. Recombination is defined as an annihilation of electron-hole pair that releases energy. There are three typical recombination mechanisms for semiconductors: band-to-band recombination, Shockley-Read-Hall (SRH) recombination and Auger recombination (Figure 12). In band-to-band recombination, the energy is released as radiation (photon). It is more common for direct band gap semiconductors, in which the minimum of the conduction band and the maximum of the valence band are at the same position in k-space [112]. This allows the electron to be shifted from the conduction band to the valence band without transferring any momentum. This is not the case in indirect band gap semiconductors, such as TiO_2, making the radiative recombination highly unlikely [89]. In indirect band gap semiconductors, nonradiative recombination is the more common recombination

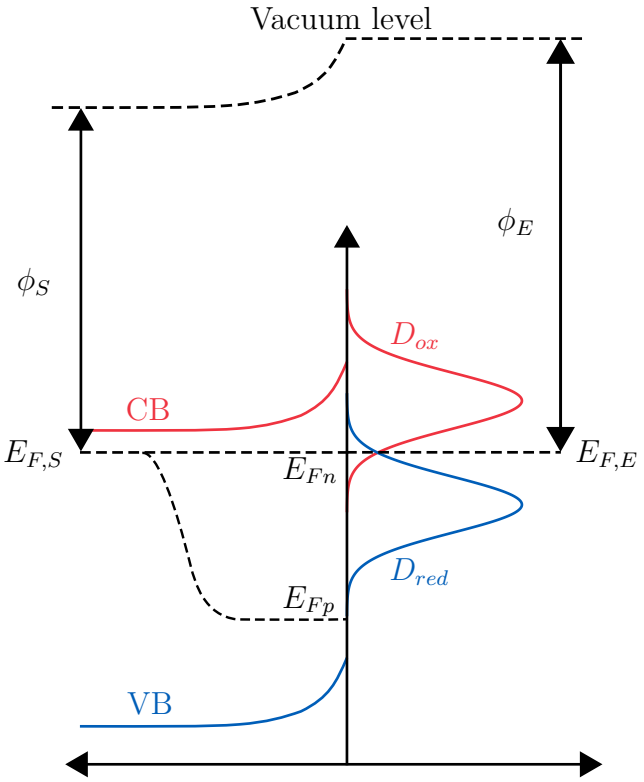

Figure 11: Schematic of the energy bands of illuminated TiO_2 surface immersed in electrolyte solution.

path. Two possible nonradiative recombination pathways are SRH recombination (also known as trap assisted recombination) and Auger recombination [114]. In SRH recombination, deep level defect sites act as traps (E_t) for electrons and holes, and recombination occurs at the trap site. The charge carrier energy is released as lattice vibrations (phonons). In Auger recombination, the energy released in recombination is transferred to another electron which is excited to a higher energy level.

For photocatalytic oxidation and reduction reaction to take place, photogenerated charge carriers need to migrate to the surface before recombination takes place. Before the recombination takes place, charge carriers can on average diffuse a distance called the carrier diffusion length L:

$$L = \sqrt{D\tau} = \sqrt{\frac{k_B T}{q}\mu_m \tau}, \tag{12}$$

where D is the diffusion coefficient, τ is the carrier lifetime in bulk, q is the elementary charge and μ_m is the carrier mobility [110]. For example, the diffusion length for holes in n-type single crystal silicon is around 300 μm for typical values of $D = 12.5$ cm^{2}s^{-1} and $\tau = 8 \cdot 10^{-5}$ s. Charge carriers which are generated at depths greater than L cannot participate in surface reactions because the recombination occurs before they can reach the electrolyte interface. To avoid recombination, charge carriers need to be efficiently separated. The positive charge of the n-type semiconductor surface and negative charge of the electrolyte create an electric field $\mathcal{E}$. The electric field

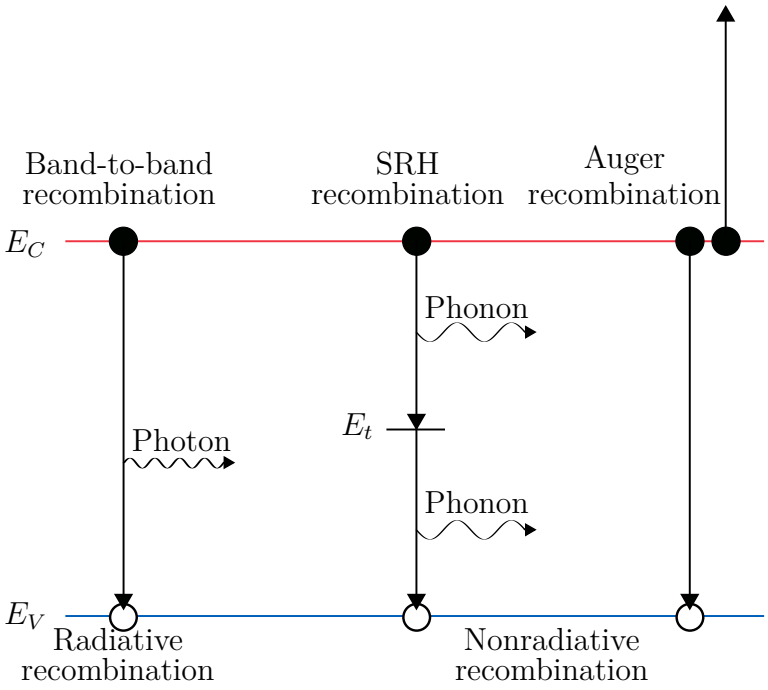

Figure 12: Different recombination mechanisms in semiconductors. In band-to-band recombination process, electron from conduction band fills a hole in the valence band, and a photon is emitted. SRH recombination occurs at a trap site E_t in the band gap and the energy is released in phonons. The arrow illustrates the movement of an electron, causing a hole to be transported to the opposite direction. In Auger recombination, the energy is transferred to another electron which is excited to a higher energy state.

enhances the separation of charge carriers by increasing the drift velocity

$$v = \frac{q\mathcal{E}\tau_m}{m_{ef}}, \tag{13}$$

where τ_m is the mean free time of a charge carrier between collisions and m_{ef} is the effective mass of a charge carrier [112]. For electrons, the velocity is negative since they drift to the opposite direction to the electric field. With high drift velocities, the charge carriers are efficiently separated and the recombination can be decreased.

In photodeposition, the metal precursor is either reduced or oxidized on the semiconductor surface. The reactions depend on the energy-band positions of the metal precursor and the semiconductor. Reduction reactions result in the deposition of metallic nanoparticles whereas oxidation reactions result in a metal oxide deposition. General examples of reductive and oxidative metal (M) photodeposition reactions are given by Wenderich [23]:

$$\mathrm{M^{n+}(aq) + ne^- \longrightarrow M(s)}, \tag{14}$$

$$\mathrm{M^{n+}(aq) + nh^+ + nH_2O \longrightarrow MO_n(s) + 2\,nH^+}. \tag{15}$$

In reductive photodeposition (Equation (14)), oxygen vacancies in the semiconductor lattice have a large role because of their ability to act as electron traps. When photogenerated electrons are trapped to oxygen vacancies, local electron density increases at the defect site. Positive metal ions are attracted to the negative sites and adsorbed to the photocatalyst surface [115]. Electrons in oxygen vacancies migrate to the adhered metal ion if the metal has a lower Fermi level than TiO_2. Electron migration causes the metal reduction reaction to occur.

After the initial metal reduction, the photogenerated electrons can either migrate to new active sites in TiO_2 or to existing metal nanoparticles. Study by Hidalgo *et al.* [60] showed that electrons are more likely to migrate to existing metal particles causing them to expand rather than creating new nucleation centers. Two reasons for this behavior were found. Firstly, the electron migration to the metal deposits creates an electric field which induces adsorption of aqueous metal ions to the existing metal deposition sites. Secondly, the illumination of the solution forms OH radicals which can partially oxidize and dissolve the existing small Au deposits and causing the re-deposition.

Most of the existing photodeposition studies utilize metal reduction reactions for nanoparticle deposition. However, there are some studies also concentrated on the oxidation reactions of photodeposition (Equation (15)) [116]. In metal oxidation reactions, the metal ions are oxidized by photogenerated holes enabling the deposition of metal oxide nanoparticles.

In the case of photodeposition from liquid precursor, nanoparticles are formed by heterogeneous nucleation. In heterogeneous nucleation, the ions dissolved in the precursor solution nucleate at a solid surface [117]. Alternatively, in homogeneous nucleation the nucleation occurs throughout the precursor phase. When the particles nucleate, their growth depends on the ratio of surface free energy and crystal free energy. Surface free energy describes the energy required to create a new surface. On small particles, the surface free energy dominates, making the particles unstable, which leads to the redissolution of the particles. When the particle size increases over a critical radius, the crystal free energy has a larger impact on the total energy of the particle, stabilizing it and enabling further particle growth. This effect is called the Ostwald ripening, and it is the main cause of size variations of nucleated particles [117].

In addition to Ostwald ripening, there are other theories for the nanoparticle nucleation and growth that can be applied to different materials. The nucleation and growth of gold particles have been shown to have three different phases [118]. First, the gold particles nucleate rapidly from the precursor and grow further through Ostwald ripening or coalescence. In coalescence, two or more particles merge without any preferred orientation and form a single larger particle [117]. In the second phase, the gold particle size increases due to growth by diffusion [118]. In this stage, the growth rate of the particles depends on the flux of precursor salt supplied for the existing particles. The final phase includes a more rapid growth of the particles due to an autocatalytic reduction, in which the gold nanoparticles catalyze the reduction of gold ions from the precursor. In the same study, it is acknowledged that polydispersity decreases during particle growth, as the growth of existing particles

is more likely than the nucleation of new particles. In contrast, the nucleation and growth of platinum occurs via a two step mechanism, sometimes referred as the Finke-Watzky mechanism [117]. In this case, the first step is a slow nucleation of platinum nanoclusters [119]. Once a sufficient amount of Pt particles are nucleated, they act as catalysts for faster autocatalytic surface growth.

3.2 Process variables in photodeposition

In this section, a literature survey is conducted related to the process parameters of photodeposition. The parameters are presented and their effects to photodeposition are discussed. This Section focuses on the photodeposition of platinum and gold.

Although liquid-phase photodeposition seems like a simple process, the process has many variables that depend on the photocatalyst (such as recombination rate and amount of defects as active sites) and the process conditions (pH, sacrificial donors, precursor, deposition time, dissolved oxygen, and the intensity of light). The parameters need to be optimized in order to achieve the required particle size and density on the photocatalyst surface. The influence of different parameters has been widely studied, and a summary of the results is gathered below. Most of the studies on photodeposition have concentrated on platinum precursors, even though similar effects could be expected with other noble metals, as well.

The pH of the solution affects the kinetics of photodeposition. According to multiple studies on the photodeposition of platinum on TiO_2, low pH solutions ($pH < 5$) result in deposition of metallic Pt^0 particles [120–122]. At higher pH, the valence state of deposited platinum is larger resulting in deposition of PtO, PtO_2 or $Pt(OH)_2$ depending on the pH and sacrificial agent used [120, 121]. In the absence of a sacrificial agent, photodeposition of platinum at low or neutral pH results in $Pt(OH)_2$, whereas PtO_2 formation occurs at higher pH [120].

pH also affects the dispersion of photodeposited metal. This has been explained with pH dependent interactions between platinum and TiO_2 [111]. The interactions change depending whether pH is higher or lower than the isoelectric point of TiO_2. Isoelectric point (IEP) is the pH value in which immersed surface of a solid oxide has no net charge [123]. If the solution is more acidic than the IEP, the metal oxides have a net positive charge. Conversely, more basic solution yields a net negative charge. This is possible because in acidic pH, the bridging oxygen atoms in the TiO_2 lattice can adsorb H^+ ions, resulting in a positively charged surface [111]. Conversely, in basic solutions OH^- ions are adsorbed by Ti atoms in the lattice, causing a negative charge to the surface. Zhang *et al.* [121] studied the effect of pH to the photodeposition of platinum on TiO_2 particles above and below the IEP (6.25 for TiO_2). At lower pH values (< 5), the TiO_2 surface attracts platinum complexes ($PtCl_6^{2-}$), which leads to increased local concentration of platinum ions. This results in a high deposition rate and a large particle size. Above the isoelectric point (> 7), the interaction is repulsive resulting in lower deposition rate, higher dispersion and smaller particle size. If the pH is near the isoelectric point, TiO_2 particles agglomerate and the area of available surface decreases. Because of the decreased surface area, there is more platinum per TiO_2 area, and large agglomerates

are deposited. Contrary studies also exist where Pt agglomeration was not detected in acidic solutions, but only at pH values close to neutral (pH range of 5–9) [124].

The effect of pH has also been studied in the photodeposition of gold on TiO_2 [93]. Similar to platinum, gold particle size was found to decrease with increasing pH. In basic solutions (pH 9), precursor $HAuCl_4$ precipitates quickly to $Au(OH)_nCl_{4-n}$, which decreases the amount of available gold for the deposition reaction. Contrary to the photodeposition of platinum, pH does not affect the oxidation state of deposited gold, as it is always mostly metallic (Au^0) [60, 93].

Another typical way to control the photodeposition is the selection of precursor and its concentration. Photodeposition can be conducted from a wide range of precursors. Different precursors can have individual properties that lead to differences in photodeposition. Herrman *et al.* [125] compared photodeposition kinetics of multiple platinum precursors. It was detected that adsorption of the precursors to the photocatalyst surface decreases if the precursor is nonionic (for example $Pt(NO_2)_2(NH_3)_2$). Some of the differences could be explained with a change of pH of the solution when the precursor dissolved. For example, $H_2Pt(OH)_6$ has six hydroxyl groups that can increase the pH value of the solution once dissolved. Stability of the precursor was the third variable that was detected to affect the deposition rate. More stable complexes experienced lower deposition rates.

In the same study, dependency between precursor concentration and deposition rate was observed [125]. Photodeposition rate was found to be linearly dependent on the initial precursor concentration, when the concentration is small. When the concentration increases, reaction rate becomes independent of the precursor concentration and dependent on other variables. At this point, the reaction rate is not anymore limited by the ion diffusion to the photocatalyst surface. Upon further increase of the concentration, the reaction rate becomes more dependent on the deposition setup, as it is determined by parameters such as radiant flux of light, reactor geometry and photon absorption efficiency.

The selection of deposition time and illumination intensity affect the photodeposition process significantly. Photodeposition rate is initially linearly dependent on the incident photon flux [125]. Photodeposition rate is higher with higher intensity but as the deposition time increases, the deposition rate changes. With longer deposition times, the precursor concentration in the solution will decrease because part of the precursor is already reacted. This leads to a decrease in the deposition rate. Thus, the initial parameters change, and the deposition rate will decrease even with a constant photon flux.

Photodeposition time can be used to control the particle size of the deposited metal. Longer illumination time yields a larger particle size and smaller dispersion [126]. The development of average platinum particle diameter as a function of time measured by Murcia *et al.* [126] is presented in Figure 13. As stated previously in Section 2.2, platinum particles nucleate at oxygen vacancy sites due to their higher electron density. The deposited platinum particles trap photogenerated electrons from the photocatalyst, and the trapped electrons reduce more platinum complexes increasing the particle size. As the illumination time increases, more photons are absorbed, and more electrons are generated for the reduction reactions. The existing platinum

particles are preferred sites for further metal reduction, as the trapped electrons increase the local electron density, attracting the positively charged metal ions.

In similar studies with the photodeposition of gold, the intensity of the light was found to have a more profound influence on the amount of deposited gold than the deposition time [60]. Particle size was found to increase with increasing intensity. Alternatively, Chang *et al.* [127] observed, that the gold nanoparticles agglomerate and particle size increases when the photodeposition time is increased. Similarly to the study by Hidalgo *et al.* [60], lower light intensity yielded smaller and highly dispersed gold particles. Photodeposition of small gold nanoparticles with diameters less than 5 nm has also been demonstrated with short deposition times (3–5 min) [128].

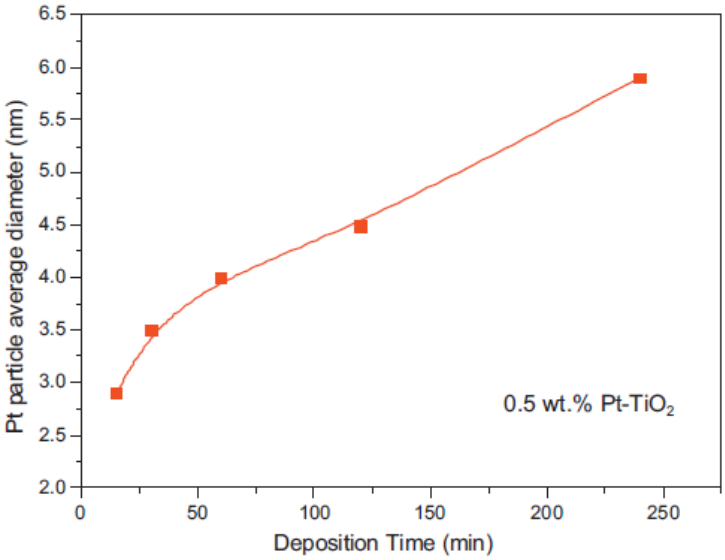

Figure 13: Average platinum particle size as a function of photodeposition time, as measured by Murcia *et al.* [126].

Photodeposition often requires existence of a sacrificial donor in the precursor solution. The sacrificial donor is typically an organic molecule that takes part in the deposition reaction. Donors scavenge the photogenerated holes from the photocatalyst by donating electrons to the TiO_2 lattice [89]. When the excess holes are removed, the photogenerated electrons can participate in metal reducing reactions because they are less likely to recombine [115]. In the absence of sacrificial donors, hole accumulation on the surface could also lead to the corrosion of the photocatalyst [9]. Sacrificial donors used in photodeposition are typically alcohols, such as methanol [93], ethanol [129], or butanol [115]. The reaction between methanol and a photogenerated hole forms a radical ($C^{\bullet}$) which donates an electron to the TiO_2 and an aldehyde is formed [89]:

$$CH_3OH + O^{2-} \longrightarrow C^{\bullet}H_2OH + e^- + OH^- \longrightarrow CH_2O + 2\,e^- + H_2O. \qquad (16)$$

Similar reactions can be presented for other alcohols as well. Hole scavenging and

electron donating leads to a downward band bending at the TiO_2 surface which allows the reduction reactions to take place at the semiconductor-electrolyte interface [89]. In contrast to reductive photodeposition, sacrificial donors are not used in oxidative photodeposition because the photogenerated holes are needed for the metal oxidation reaction.

Sacrificial agents have been found to affect the oxidation state and the dispersion of the photodeposited metal. The oxidation state of the metal can be controlled by sacrificial donor concentration. When photodepositing platinum on TiO_2, absence and low concentrations of sacrificial donor yield higher valance states of platinum (Pt^{II} or Pt^{IV}) whereas metallic Pt^0 is achieved with higher donor concentrations [122, 130].

Dispersion of the deposited metal has also been detected to be dependent on the type of sacrificial agent. Nakamatsu *et al.* [131] showed that highly dispersed platinum is achieved with ethanol, and the dispersion decreases sequentially with methanol, 2-propanol, acetic acid and 2-methyl-2-propanol. It is proposed that the effect of sacrificial agent is based on the formation of radicals. The radicals can provide electrons for the reduction reaction of the metal but the ability of radicals to reduce metals depends on the sacrificial agent. The existence of radicals with higher reducing power results in a finer dispersion of metal particles.

Typically, photodeposition is conducted in aqueous solution but it can also be done in fully organic solutions. If the photodeposition is conducted in a sacrificial donor solution, the properties of the solvent have more profound effect to the deposition kinetics. This was detected by Fernando *et al.* [115] who studied the dispersion of photodeposited gold particles with seven different sacrificial agents (cyclohexane, toluene, tert-butanol, 1-butanol, ethanol, methanol and acetonitrile). They found out that the reaction rate is determined by the relative permittivity (ϵ) of the solvent. Typically, solvents with higher ϵ experience lower reaction rates than the ones with lower ϵ. Solvents with high ϵ have a potential gradient that affects the charge transfer in a greater radius which results in deposition of fewer larger gold particles. If the ϵ of a solvent is low, interfacial electron transfer occur faster, leading to the deposition of multiple small Au nanoparticles. Two exceptions to this theory were butanol and t-butanol. The differences to other measurements were explained by their high viscosity. In low viscosity solvents, such as aqueous solutions, the rate is determined by the electron transfer at the semiconductor-solution interface. High viscosity changes the photodeposition process to be diffusion limited instead of charge transfer limited. With high viscosity solvents, the decreased diffusion rate limits the amount of reactive ions available at the photocatalyst surface, decreasing the overall reaction rate.

Dissolved oxygen in the precursor solution also affects the deposition. Dissolved oxygen can act as a photoelectron scavenger affecting the electron transfer process [115]. Electron scavenging is a competing reaction with the reduction of metal ions. When electrons are scavenged by oxygen, it decreases the electron accumulation on the surface of the semiconductor. Without dissolved oxygen, electrons will accumulate on the conduction band of a semiconductor creating a potential gradient between the solution and semiconductor [115]. This potential gradient would attract metal complexes which are then reduced to metallic clusters. Thus, presence of

dissolved oxygen leads to decreased reaction rate and creation of smaller spherical nanoparticles instead of larger clusters. Dissolved oxygen can also oxidize the surface oxygen vacancies which are active sites for metal reduction reactions [47]. Removing the dissolved oxygen is especially important when the precursor solutions consist mainly on organic solvents. Organic solvents have around 10 times larger dissolved oxygen content compared to water [115]. Dissolved oxygen is typically removed from the solution by purging the solution with inert gas such as N_2 [86] or Ar [115].

3.3 Photodeposition of cocatalytic materials

In this section, the photodeposition of cocatalytic materials is discussed. The focus of this section is on the photodeposition of gold and platinum but examples of other available cocatalytic materials are given. The available precursors are presented for the photodeposition of Au and Pt.

Photodeposition allows the nanoparticle deposition of multiple materials, from metals to metal oxides and even non-metal nanoparticles. Photodeposition is typically used for the deposition of noble metals, such as platinum [132], gold [60], and copper [133]. Noble metal oxides, such as ruthenium dioxide, have also been successfully photodeposited [134]. An example of non-metal nanoparticle that can be photodeposited is CoPi, a cobalt-phosphorus compound that is also used as a cocatalyst [135]. In this thesis, photodeposition experiments are conducted with gold and platinum.

Noble metals, such as gold and platinum, are efficient cocatalyst for photocatalytic reactions because of their ability to trap electrons. Both of these metals improve the photocatalytic efficiency significantly. Iliev *et al.* [86] proved, that gold can improve the photocatalytic efficiency of TiO_2 even in small quantities. On the other hand, platinum has been superior cocatalyst for photocatalysis compared to gold [20, 29]. This is expected, since the Fermi level of platinum is lower than that of gold. As discussed earlier, the Fermi levels of metal and semiconductor will align when brought in contact. Alignment occurs, when the electrons are transferred from the higher Fermi level (TiO_2) to the lower Fermi level (metal) and an equilibrium state is achieved. Since the Fermi level difference between TiO_2 and platinum is larger than the one between TiO_2 and gold, more electrons are needed to transfer across the semiconductor-metal junction in Pt-TiO_2 interface to align the Fermi levels. However, the Fermi level difference is not the only variable affecting the photocatalytic efficiency. The photocatalytic efficiency also depends greatly on the particle size and loading of the cocatalyst, as discussed earlier.

The photodeposition of gold and platinum allows the use of multiple different precursors. Gold is typically deposited from chloroauric acid ($HAuCl_4$) [136, 137] but also $NaAuCl_4$ has been used [97]. Platinum photodeposited offers more possibilities for precursors such as H_2PtCl_6, Na_2PtCl_6, $H_2Pt(OH)_6$, $Pt(NO_2)_2(NH_3)_2$ [125] and K_2PtCl_6 [131]. As previously discussed, precursors affect the kinetics of the deposition because of their influence on the pH, nonionic character, and stability differences.

Ruthenium dioxide is another promising cocatalytic material which can be photodeposited. It can be reduced in oxide form but there are also reports of oxidative

deposition of RuO_2 [116, 138]. In the latter case, $Ru_3{}^+$ is oxidized to RuO_2 by photogenerated holes. This photodeposition reaction is also known as a photohole-oxidation-assisted method [116].

Ruthenium dioxide has a different role in photocatalysis compared to gold and platinum cocatalysts. Au and Pt cocatalysts trap electrons during photocatalysis, whereas ruthenium dioxide is used as a hole scavenger. The photogenerated holes are trapped in the RuO_2 nanoparticles and are then extracted to the oxidation reaction. The O_2 evolution requires cocatalysts as it is the more challenging reaction compared to H_2 evolution. In O_2 evolution, four holes react with two water molecules creating four protons and the oxygen-oxygen double bond, as was previously presented in Equation (2). The O_2 evolution dominates the activation energy of the overall water-splitting reaction [91]. This creates a need for a cocatalyst that can efficiently decrease the activation energy of this reaction. RuO_2 is considered as one of the most active cocatalyst for O_2 evolution [16]. It will also improve the durability of the photocatalyst as it decreases the oxidative decomposition by trapping the holes [139].

4 Materials and methods

In this section, the photodeposition procedure is described in detail as it is conducted in this thesis. The parameter selection is presented and justified based on previous studies. Next, the Taguchi technique is introduced as an effective method for minimizing the number of samples. Finally, this chapter describes the sample characterization methods used to determine the success of the photodeposition process.

4.1 Photodeposition procedure

This section describes the photodeposition procedure of noble metals as conducted in this thesis. All the materials and equipment are presented. The parameters studied in this work are discussed based on earlier studies. The physics behind the process is also summarized.

Photodeposition is based on the photogeneration of charge carriers in a photocatalytic semiconductor under illumination. The charge carriers can either recombine and produce thermal energy or migrate to the surface of the sample and react with adsorbed species. These species are brought to the semiconductor surface by the liquid medium in which the precursor is dissolved. Depending on the Fermi levels of the semiconductor-metal ions system, the adsorbed ions can be reduced or oxidized on the semiconductor surface. In this thesis, noble metals with high work functions are reduced to the photocatalyst surface. The area in which the reduction reactions occur can be controlled by masks, since the electron excitation occurs only at the illuminated area.

The sample preparation process started with ALD deposition of TiO_2 on a fluorine-doped tin oxide (FTO) coated glass sample (Figure 14a and 14b). The FTO layer functions as a conductive layer to allow sample characterization, which is discussed later on. The TiO_2 ALD growth was conducted at a temperature of 250°C to promote the growth of the anatase phase. The thickness of the TiO_2 layer was 250 nm to ensure sufficient photon absorption.

After the TiO_2 deposition, the surface was covered with a photoresist to ensure the cleanliness of the surface during storage. The photoresist was removed with acetone before the sample was used. The sample was then ultrasonicated (Elmasonic S 30 H) in acetone. After the ultrasonication, the sample was rinsed with acetone (ACE), isopropyl alcohol (IPA), and de-ionized water (DIW) to remove the organic solvents from the surface. Finally, the sample was blow-dried with N_2.

The preparation of the precursor solution started with adjusting the pH of the DIW. Samples were prepared in two different pH, in natural pH 7 and in acidic pH 4. The acidity was adjusted with sulfuric acid (H_2SO_4). The solution was purged with N_2 gas in order to remove dissolved oxygen. Purging was conducted before precursor or sacrificial donor were added to efficiently control their concentrations. It was noted that the possibility of spilling or evaporation during N_2 purging could affect the critical concentrations of the metal salt and donor.

Stock solutions with precursor concentration of 10 mg/ml were prepared for

gold and platinum precursors. The gold stock solution was prepared by measuring 20 mg of $HAuCl_4 \cdot xH_2O$ in a 4 ml bottle and dissolving it with 2 ml of DIW. The gold precursor contains an unknown amount of crystallization water, denoted by xH_2O. According to provider (Sigma-Aldrich), the most common number of water of crystallization for $HAuCl_4$ is 3 (and 4). The approximation of $x \approx 3$ yields the total mass of gold ion in the solution to be roughly half of the mass of the chloroauric acid, since the molar mass of $HAuCl_4 \cdot 3H_2O$ is 393.804 g/mol and the molar mass of Au is 196.967 g/mol. The amount of crystallization water does not affect the molar mass drastically since the molar mass of water (18.016 g/mol) is small compared to the molar mass of the chloroauric acid (339.759 g/mol).

The platinum precursor used in this thesis is an 8 wt-% aqueous solution of H_2PtCl_6 ordered form Sigma-Aldrich. Similar stock solution was prepared from it measuring 50 µl of the 8-wt% solution (with density of 1.05 g/ml) to a 2 ml bottle and diluting it with 370 µl of DIW. The final concentration of the platinum stock solution was 10 mg/ml. The molar mass of the precursor is 409.81 g/mol so the platinum (molar mass of 195.084) ion content is around 48%, which is similar to the gold ion content in $HAuCl_4 \cdot xH_2O$.

The stock solutions were diluted to the desired final concentration with N_2 purged DIW with the desired pH. After the dilution of the stock solution, a sacrificial donor was added to the solution. The sacrificial donor used in this thesis is methanol (CH_3OH). Methanol was added to the solution right before the deposition in order to minimize the chance of methanol evaporation. Total volume of the precursor solution for each sample was 200 µl in order to standardize errors between different samples.

After the preparation of a solution, 20 µl of it was measured to the cleaned TiO_2 surface (Figure 14c). The solution was covered with a cover slip manufactured by Arrayit corporation (LifterSlip Microarray Glass Coverslips 22 x 25 mm^2), that has a cavity with a volume of 20 µl (Figure 14d). The cavity is prepared with thin printed Teflon lines near two opposite edges of the slip. The surface tension of the water solution will keep the fluid inside the cavity. The cavity is sealed with Teflon tapes on all four edges of the slip (14e). The sealed sample is then taped to a sample holder which also acts as a mask for the light. There is an aperture in the sample holder with a diameter of 4.4 mm that determines the illuminated area on the sample.

The sample holder is placed in front of a light source so that the generated light travels through the deposition mask, as illustrated in Figure 15. A 1000 W xenon lamp (Oriel model 66021) is paired with a monochromator (Oriel MS257), which is used at wavelength of 360 nm. The intensity of the light was changed by changing the distance of the sample stage to the monochromator lens. The intensity of the light decreases with increasing distance because the beam diverges as it leaves the monochromator, and the same intensity is distributed to a larger area. The optical power of the light was measured with a Thorlabs PM100D using a S130VC Slim Sensor detector. Two positions were selected for the sample holder based on optical power measurements. The measured power for the closer position was around 70 µW and 35 µW for the other, corresponding to irradiances around 460 µW/cm^2 and 230 µW/cm^2, respectively. The power was measured through the aperture in the sample holder so the diameter of the measured spot is approximately equal to the

diameter of the aperture (4.4 mm).

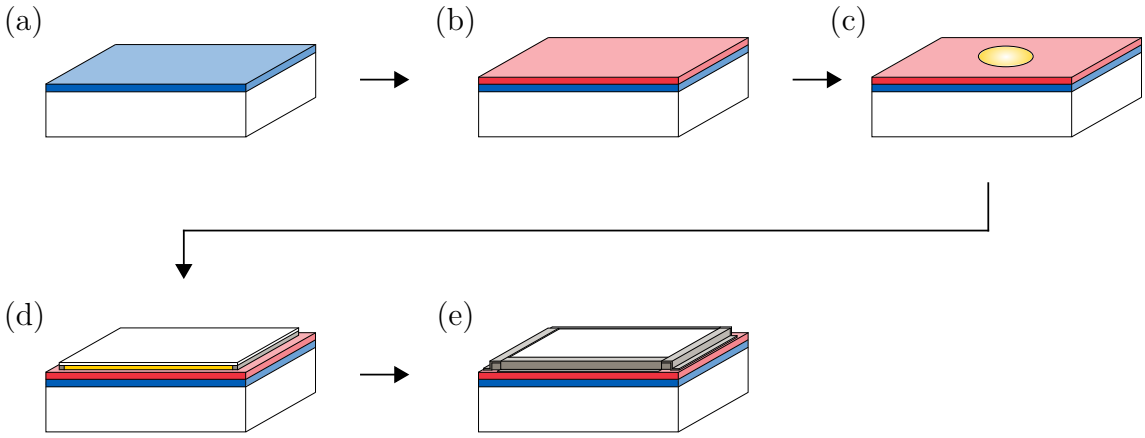

Figure 14: Sample preparation procedure. (a) The samples used in this thesis are fabricated onto FTO-coated (blue) glass substrates. (b) A photocatalytic anatase TiO_2 layer (red) is grown on the substrate by ALD. (c) 20 µl of precursor solution (yellow) is measured on top of the clean TiO_2 surface. (d) A cover slip with a 20 µl cavity is placed on top of the solution, spreading it. The cavity is formed by Teflon spacers (gray) which are printed on two edges of the slip. (e) The solution is sealed inside the cavity with Teflon tapes on all four sides of the cover slip.

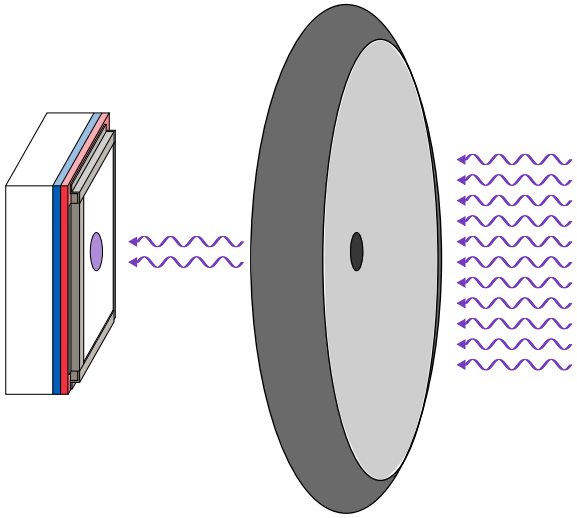

Figure 15: UV-illumination of the sample through a mask with an aperture. The aperture determines the illuminated area.

The 1000 W xenon lamp stopped working after the first four samples so the remaining samples were fabricated with another light source placed in the same configuration. The replacement lamp was a 100 W xenon lamp which is also manufactured by Oriel. In order to acquire the same irradiance from the replacing light source, the monochromatic light was focused with two lenses to a smaller area. The irradiance was measured with the same device as with the first configuration,

and the sample stage and the lenses were adjusted until identical irradiances were achieved. A sample with identical process was prepared with the 100 W lamp and compared to the sample prepared with the 1000 W lamp. The results were identical, validating the similarities of the two different light sources.

After the deposition, the illuminated spot was marked with a marker on the back side of the glass substrate. The sample was then detached from the sample holder, and the Teflon tape seals and the cover slip were removed. In order to find the deposition area also from the front side of the substrate, small scratches were made based on the marker sign on the back side to indicate the illuminated area. The remaining solution was removed by dipping the substrate to DIW, ACE and IPA. After IPA, the sample was cleaned with DIW to minimize the amount of IPA residues. The substrate was blow-dried with N_2 and stored for characterization.

4.2 Taguchi method for parameter variation

This section describes the Taguchi process, which is used for decreasing the number of samples. All of the different steps needed in conducting a Taguchi optimization run are discussed. The parameters used in this thesis are presented. Finally, this section presents the statistical methods used to analyze the parameters.

The amount of samples was minimized by using the Taguchi process, as presented in a book by Ross [140]. It allows minimizing the sample size while enabling the detection of multiple variable interactions and the separation of the effects caused by the main factors. In the Taguchi approach, the variables are assigned to independent orthogonal arrays which determine the variable combinations being tested. In order to conduct a Taguchi process, a total of 12 steps are needed:

1. Stating the problem.
2. Stating the objective.
3. Selecting the quality characteristics and measurement systems.
4. Selecting the influential factors considering the quality characteristics.
5. Identifying the control and noise factors.
6. Selecting levels for the factors.
7. Selecting the appropriate orthogonal arrays.
8. Selecting the influential interactions considering the quality characteristics.
9. Assigning the factors to orthogonal arrays and locating the interactions.
10. Conducting the tests as orthogonal arrays describe.
11. Analyzing the results.
12. Conducting a confirmation experiment.

In this thesis, the aim is to achieve a densely packed noble metal nanoparticle (diameter less than 20 nm) coating by varying the photodeposition parameters. This should be achieved with room-temperature processes without external biases and the deposition area should be defined by UV-illumination. The process parameters need to be determined so that the optimal fabrication procedure can be predicted and conducted. The quality of the samples is evaluated by scanning electron microscopy, followed by image analysis. Details of the sample characterization procedure are discussed in Section 4.3. The image analysis concentrates on the particle size and the density of the particles. The parameters selected for the study are based on a literature study followed by a series of test samples, confirming the results from literature and guaranteeing the reproducibility of the results.

As stated previously in Section 3.2, multiple parameters affect the kinetics of photodeposition. Seven different control factors were identified and selected to be studied in this thesis: the effect of surface treatment (oxygen vacancy concentration), N_2 purging time, solution pH, precursor concentration, sacrificial donor concentration, light irradiation and deposition time. In addition, there are multiple noise factors that could affect the results, for example solution temperature, age of the solution, cleanliness of the TiO_2 surface, that time the solution stays on the substrate before the deposition, intensity distribution of the xenon lamp and possible wavelength variations.

In order to clearly indicate the influence of the aforementioned seven variables with reasonable amount of samples, two levels were selected for each factor, the other being twice the first one. The variables and their values are gathered in Table 1. The variables were selected based on the literature study presented previously in Section 3.2 as well as experimental tests conducted before the actual sample series. Two levels are used for continuous parameter testing since it allows interpolation and extrapolation of the data [140]. All the variables are continuous, except the surface treatment which is the only discrete parameter studied. Same variables are used for the photodepositions of gold and platinum with the exception of deposition time, which is longer for the platinum samples. The noise factors are minimized by keeping track of the times and using the same exact procedure with each of the samples.

Table 1: The variables used in this thesis.

Variable	Value 1	Value 2
H_2 thermal treatment	No	Yes
Solution pH	4	7
Time for N_2 purge	15 min	30 min
Precursor concentration	1 mg/ml	2 mg/ml
Methanol concentration	5 vol-%	10 vol-%
Light intensity	35 µW	70 µW
Deposition time (Au)	15 min	30 min
Deposition time (Pt)	60 min	120 min

The hydrogen thermal treatment was conducted with PEO-601/ATV furnace

using forming gas (mixture of nitrogen and hydrogen) as the hydrogen precursor. The flow rate of forming gas was 600 l/min. The samples were heated with the constant heating rate of 10°C/min until the desired temperature of 400°C was reached. According to earlier studies, the temperature of 400°C is sufficient for the creation of oxygen vacancies [64]. The temperature was held constant at 400°C for 2 h followed by a cooling of the sample with N_2 purge. After the H_2 treatment, the samples were stored in N_2 atmosphere until the deposition took place to reduce the probability of re-oxidation of the created oxygen vacancies.

The pH of the solution was differed between natural pH 7 and acidic pH 4. Acidic pH value was selected so that it was below the isoelectric point of TiO_2 (pH 6.25). As discussed previously in Section 3.2, the isoelectric point determines the surface charge of the substrate, which affects the adsorption of the precursor ions to the surface. The pH of the solution was adjusted with H_2SO_4. The gold and platinum precursor salts are both acidic salts, and they will decrease the pH slightly. Due to the low concentrations of the salts in the precursor solutions, their influence to the pH is neglected.

According to Taguchi method, data needed to determine the influence of a single parameter in the case of seven two-level variables can be achieved with 8 samples. The samples form a so-called *L8 Standard Orthogonal Array Matrix* seen in Table 2 for the gold deposition and Table 3 for the platinum deposition. In order to study individual variables, each of the two possible values are assigned to four samples. However, the parameter combinations differ for each of the samples making all of the samples unique. Because of the small amount of samples, the resolution of this analysis is low. To achieve a higher resolution analysis, there should be empty arrays for parameter interaction testing. However, the low resolution approach is always recommended to be the first experiment [140]. From now on, the samples with gold deposition are referred to samples 1.1 to 1.8 according to Table 2. Similarly, the samples with platinum deposition are referred to samples 2.1 to 2.8 according to Table 3.

Table 2: Parameters used for the gold samples in this thesis.

	Sample							
Parameter	1	2	3	4	5	6	7	8
H_2 treatment	No	No	No	No	Yes	Yes	Yes	Yes
CH_3OH vol-%	5	5	10	10	5	5	10	10
Illumination P [µW]	70	70	35	35	35	35	70	70
Deposition t [min]	30	15	30	15	30	15	30	15
Precursor C [mg/ml]	1	2	1	2	2	1	2	1
N_2 purging t [min]	30	15	15	30	30	15	15	30
pH	7	4	4	7	4	7	7	4

Tests were conducted according to Tables 2 and 3 for gold and platinum samples, respectively. The samples are divided into two halves, the non-H_2 treated and the

Table 3: Parameters used for the platinum samples in this thesis.

	Sample							
Parameter	1	2	3	4	5	6	7	8
H_2 treatment	No	No	No	No	Yes	Yes	Yes	Yes
CH_3OH vol-%	5	5	10	10	5	5	10	10
Illumination P [µW]	70	70	35	35	35	35	70	70
Deposition t [min]	120	60	120	60	120	60	120	60
Precursor C [mg/ml]	1	2	1	2	2	1	2	1
N_2 purging t [min]	30	15	15	30	30	15	15	30
pH	7	4	4	7	4	7	7	4

H_2 treated. This allowed easier scheduling of the sample preparation, because the H_2 treatment could then be conducted simultaneously for samples 5–8 and the actual deposition for these samples could be performed the following day. A confirmation experiment was conducted by re-fabricating one of the samples and analyzing the results.

The statistical analysis in this thesis is conducted as follows. The results from photodeposition are collected in tables. Since the parameter combinations are orthogonal based on the Taguchi method, it is possible to evaluate the effect of different parameters on particle densities, sizes, and nearest neighbor distances by creating a table and arranging these properties from the smallest value to the largest (or vice versa). If the majority of one of the parameter values (1 or 2), presented in Table 1, are located at the top half of the table, it suggests that the parameter has an effect on the property.

The influences of single parameters on the particle densities, sizes, and nearest neighbor distances are further evaluated by calculating the averages of these properties for parameter values 1 and 2. By connecting the property values of parameters with a straight line and calculating the resulting slopes, the influence of the variable is evaluated. Thus, positive slope indicates a rise in the property value when the parameter value is changed from 1 to 2.

In order to achieve better understanding of the results, the probability that the variables affect the properties (particle density, particle size, and nearest neighbor distance) are evaluated. The evaluation is conducted as follows. Based on the average value and the standard deviation of a property, 10000 normally distributed random points were generated. The points generated for the parameter value 1 were connected to the points generated for parameter value 2 and the slopes of all 10000 lines were calculated. A negative slope indicates that changing the parameter value from 1 to 2, the value of the measured property (for example the particle density) decreases. The positive value of slope indicates the opposite.

The probability of the slopes to be negative, *i.e.* the probability that the property value decreases when changing the parameter value from 1 to 2, can be calculated by plotting the values of the slopes to a histogram. By numerically integrating the area

of negative slopes (negative x-axis) of the histogram and dividing it with the total area covered by the same histogram, a ratio between 0 and 1 is obtained. Values close to zero indicate that the probability of the slopes to be positive is higher, and values close to one indicate the opposite. For this study, the variable is considered to be statistically significant if the probability of it affecting the property is over 70%. The values from 0 to 0.3 indicate that an increase in the property value is probable when increasing the variable value. The decrease in the property value occurs at a significant probability when the values range from 0.7 to 1.

4.3 Characterization

This section describes the characterization method used in this thesis. The working principles are presented and discussed thoroughly and the equipment used are introduced. The further data processing conducted in this thesis is also described.

4.3.1 Scanning electron microscopy

Scanning electron microscopy (SEM) is a widely used surface and compositional characterization method. An electron beam is used to scan the sample surface, and the scattered electrons are detected and analyzed. The electrons are created, accelerated and focused by the SEM system. The electron creation and acceleration occurs in an electron gun. The electrons are emitted as an electron beam which is narrowed down and focused with electromagnetic lenses and apertures to enable high resolution imaging. Electromagnetic lenses can be divided to two condenser lenses and an objective lens, which is sometimes considered as the third condenser lens. Condenser lenses are needed to reduce the diameter of the emitted electron beam whereas objective lens focuses it. Final focused spot size can be as small as 1–100 nm. Apertures in SEM limit the divergence of the electron beam. SEM imaging is done in high-vacuum environment, to minimize the electron scattering while it travels from electron gun to sample and finally to the detectors. Once the electrons have interacted with the sample, they are detected and amplified so that an image can be generated for further analysis.

Scanning electron microscope has the ability to detect signals from secondary electrons (SE) and backscattered electrons (BSE), which give different information about the sample. Secondary electron imaging is used to investigate topography of the sample surface, whereas backscattered electrons give information about the composition of the sample.

Secondary electrons are electrons that are ejected from the atoms of the sample. Secondary electrons are ejected when the high-energy electrons from an electron gun interact with the electrons on the surface of the sample. The incident electrons transfer some of their energy to the secondary electrons causing them to detach. The secondary electrons only possess a small percentage of the original beam energy so the SE generation is considered to be inelastic. Because of the low energy of SEs, they originate close to the sample surface, as seen in Figure 16. The typical depth of SE signals is around 5–50 nm. Signals that are generated deeper cannot escape from

the sample due to the low energy. The low energy of SEs enables a small interaction volume, leading to a high spatial resolution.

SE imaging gives information about the topography of the sample surface. The contrast differences due to the surface features arise from surface orientations and surface profiles. The surface orientation affects to the amount of signal electrons because there is only one electron detector for secondary electrons. The electrons which scatter from surfaces facing the detector are more easily collected and appear brighter, compared to the surfaces not facing the detector. The surface profiles can also create contrast differences. Edges and inclined surfaces appear brighter because they allow the lower energy SEs to escape from larger area.

Backscattered electrons are electrons that are elastically scattered when they interact with the atoms in the sample. Only a small portion (20–40%) of the incident electron energy is lost. Because of the high energy of the scattered electrons, they can escape from deeper levels of sample surface. Typical interaction zone for BSEs reaches up to 300 nm (Figure 16). BSEs are generated in a much larger volume, which also decreases the spatial resolution of the signals.

BSE image contrast arises from variations in chemical composition. More backscattered electrons are generated when the atomic number of the studied chemical element increases. Thus, the areas with higher atomic number appear brighter in BSE image, allowing detection of different compositions of the sample. Small variations to the BSE image contrast can also be generated by crystallographic orientations of the sample because atomic packing density differs with crystallographic planes.

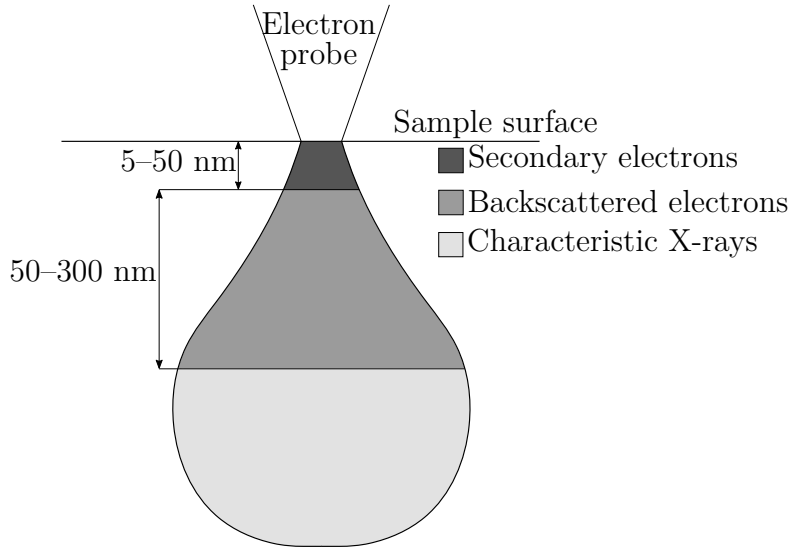

Figure 16: A schematic of the formation depths of different SEM signals.

The resolution of SEM depends on the electron beam used in scanning. With smaller beam diameter higher resolutions are achieved. The diameter of the scanning electron probe d_p can be approximated as

$$d_p = \left(\frac{4 i_p}{\beta \pi^2 \alpha_f^2} \right)^{1/2}, \tag{17}$$

where i_p is the probe current, β is the brightness of the beam, and α_f is the convergence angle of the probe. According to the equation, the resolution can be improved by increasing the beam brightness or convergence angle or by decreasing probe current. Convergence angle depends on the diameter of the final aperture, and the distance between aperture and the sample surface (known as working distance). Large aperture size and short working distance are favored for high resolution imaging, but they will decrease the depth of field significantly and vice versa.

Increasing beam brightness is another way to improve the resolution. Beam brightness can be increased by using a field emission gun as an electron gun instead of a thermonic gun. Thermonic gun operation is based on high temperature heating of a filament, which provides the electrons enough kinetic energy to escape the filament surface. In contrast, field emission guns operate by applying a strong electric field to a sharp metal tip, which pulls out the electrons from the conduction band of metal. Field emission gun can improve the brightness by a factor of 1000 compared to commonly used tungsten thermonic guns. In both cases, the brightness can be further controlled with acceleration voltage V_o of the used electron gun according to

$$\beta \propto qV_o, \tag{18}$$

where q is the electron's charge. Higher voltage will also increase the interaction volume of the signal electrons, decreasing the spatial resolution. Thus, field emission guns are an efficient way to increase the resolution without any tradeoffs.

Resolution of the image depends also on the amount of signal electrons created during scanning which is controlled by the probe current. Small current improves the resolution but there is a minimum value in the electron signals that needs to be generated in order to differentiate them from the background noise. Background noise is generated by signal amplification and current fluctuation of the electron beam. The probe current needs to be high enough because the amount of signal electrons generated is proportional to the amount of incident electrons. According to the Rose visibility criterion, an object is visible if it generates at least five times more signals than the noise level [141].

In this thesis, surface characterization and imaging are conducted with field emission scanning electron microscopes (FE-SEM) by JEOL (JSM-6335F) and by Zeiss (Supra 40). Both of the FE-SEMs have designated detectors for SE and BSE signals. The samples were attached to the sample holder with copper tape or with copper pins, which provides a conductive path to the ground. FE-SEMs were selected for this thesis, since the improvement of resolution provided by the field emission gun allows more accurate detection of the deposited nanoparticles. JEOL JSM-6335F allows imaging at the magnifications less than 50000, after which the vibrations of the building started to show in the images. For magnifications 75000 and higher a newer FE-SEM EBL Zeiss Supra 40 was used. Higher magnifications are achieved because of the more stable platform and significantly smaller working distance. The shorter working distance increases the resolution, as shown in Equation (17).

SEM is the optimal surface characterization since it enables high resolution imaging for conductive samples. The FTO coated glass substrates used in this thesis allow SEM imaging as the conductive FTO layer provides sufficient electrical

conductivity for the imaging. The metals deposited were easily visible in SE images due to the flatness of the underlying ALD-grown TiO_2 coating. The metals used had also high atomic numbers compared to the substrate, which allows the characterization with BSE detector.

4.3.2 Image processing with ImageJ

Particle size distributions and the nearest neighbor distances were analyzed from SEM images with ImageJ, an open source program that is widely used in image analysis in scientific context. With gold particles, one representative SEM image with 50000x magnification was selected for each of the samples (Figure 17a). The SEM images were slightly modified before the analysis, so that the particles are distinguished more accurately. A built-in bandpass filter in ImageJ is used to increase the contrast between the TiO_2 surface and the metal nanoparticles. Once the contrast is improved, the image is made binary, as seen in Figure 17b, with the particles showing as black and the TiO_2 surface as white. The binary mode allows a visual estimation of the image processing to evaluate the accuracy. Once the image is in binary mode, the ImageJ software can analyze the particle size and the nearest neighbor distance from the coordinates of each particle.

With the small platinum particles, the contrast from the SEM images was not strong enough for automatic identification with ImageJ. In order to increase the contrast of the nanoparticles, the brightness value was decreased to remove the small contrast irregularities that occur at the TiO_2 grains. The particles could also be highlighted to increase the contrast between the nanoparticles and the TiO_2 grain edges. Next, the bandpass filter is applied and the image is made binary. In the binary image, the ImageJ allows further modification of the image by removing the false particles which originate from the bright grain edges. Since the deposited particles are approximately round, the possibility of adjusting the circularity of the analyzed particles is also used to decrease the amount of false particles.

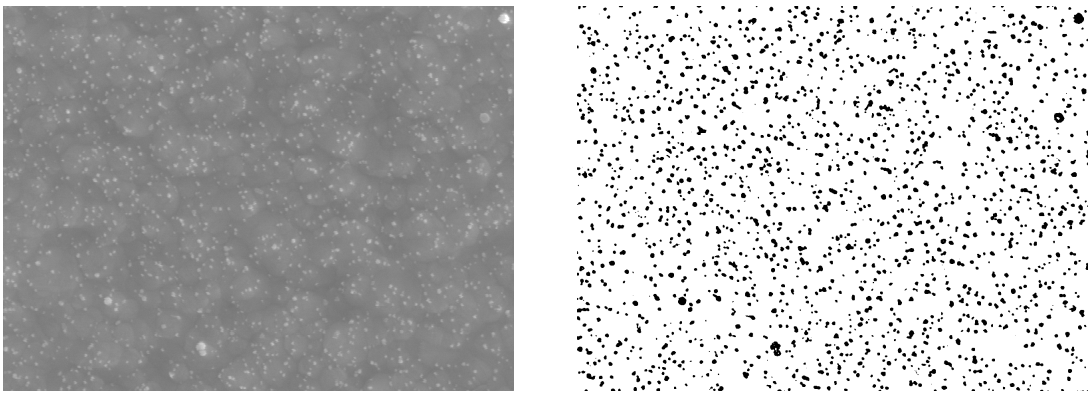

(a) Before ImageJ processing. (b) After ImageJ processing.

Figure 17: SEM image processing with ImageJ. (a) The SEM image before any image processing. (b) SEM image after ImageJ processing to a binary image. Dark areas are the particles that the program analyzes.

4.3.3 Data analysis with MATLAB

In order to understand trends in the particle size distributions and the nearest neighbor distances, the data from ImageJ is further analyzed with MATLAB software. This section describes the analysis conducted for the processed SEM images. Suitable distributions were fitted to both data sets, and characteristic parameters, such as means, medians and standard deviations, are calculated.

The size distributions of nanoparticles are typically found to be log-normally distributed [142]. A log-normal distribution is fitted to the measured particle sizes. The probability density of the log-normal distribution can be written as

$$f(x|\mu\sigma^2) = \frac{1}{x} \cdot \frac{1}{\sigma\sqrt{2\pi}} e^{-\frac{(\ln x - \mu)^2}{2\sigma^2}}, \tag{19}$$

where μ is the mean of the distribution, σ is the standard deviation and σ^2 is the variance. The goodness of the fit is evaluated with the coefficient of determination, called R^2. The value of R^2 ranges from 0 to 1, 1 indicating a perfect fit between the measured data and the fitted distribution.

Nearest neighbor distance statistics are used to evaluate the distribution of the reduced nanoparticles. It allows the comparison of the particle positioning and reduction patterns between the samples. Preferred reduction patterns can be detected by comparing the measured values of nearest neighbor distances to the models of completely spatially random processes. Depending on the similarities of the measured data and random distribution, conclusions of the possible interactions between the particles can be drawn.

Two different techniques for evaluating the spatial randomness were selected. Firstly, the random spatial distribution is modeled with a homogeneous Poisson process in 2-dimensional space. Poisson (point) process is the simplest and the most important pattern that can be used in studying completely random processes [143]. The Poisson process is considered homogeneous if (1) the average density of the points in the underlying space is constant and independent of the location, and (2) the density of points in disjoint areas are described by independent random variables [143]. A homogeneous Poisson process can be presented as a probability function following the Poisson distribution

$$P(N, L(A)) = \frac{[\Lambda L(A)]^N}{N!} e^{-\Lambda L(A)}, \tag{20}$$

where $P(N, L(A))$ is the probability of exactly N points to exist in area $L(A)$ defined by set A and $\Lambda L(A)$ is the Poisson parameter where Λ is a parameter defining the amount of points per area [144]. By defining the area to be circle ($L(A) = \pi r^2$), the probability of finding Nth inside the area defined by radius r can be solved. On the other hand, the probability of finding the Nth nearest point inside an area defined by radii r and Δr is

$$P(N, \pi r^2) = P(N, \pi(r + \Delta r)^2) - P(N, \pi r^2). \tag{21}$$

By letting $\Delta r \to 0$ and by differentiating with respect to r, the probability density function $f(r, N)$ can be computed [144]. It provides the likelihood of the Nth neighbor to be inside the distance determined by r:

$$f(r, N) = \frac{2(\pi\Lambda)^N}{(N-1)!} r^{2N-1} e^{-\pi\Lambda r^2}, \quad r > 0, N = 1, 2, \ldots. \tag{22}$$

In the case of a particle distribution, Λ is equivalent to the amount of particles in analyzed area ρ. When searching for the nearest neighbor ($N = 1$) the function simplifies accordingly:

$$f(r, 1) = 2\pi\rho r e^{-\pi\rho r^2}. \tag{23}$$

This probability density function can be fitted to the nearest neighbor distance data by calculating the event density ρ from the SEM image and by varying variables a and b

$$f(r) = 2a\pi\rho(r-b)e^{-\pi\rho(r-b)^2}. \tag{24}$$

Variable a scales the fitted curve, determining its height. Variable b moves the fitted curve along the x-axis, which compensates for the dimensions of the particles. Without the parameter b, the distribution illustrates spatial randomness of dimensionless points but in a real case the nearest neighboring distance depends on the radii of adjacent particles, resulting in a minimum nearest neighboring distance of particles 1 and 2 to be $r_1 + r_2$. The goodness of the fit is evaluated with R^2 value, where the perfect fit results in R^2 value of 1.

Second way to evaluate the spatial randomness is the so-called Clark-Evans test. In the Clark-Evans test, the values of the average nearest neighbor distance $\bar{r_A}$ calculated from the data are compared to the mean nearest neighbor distance of completely randomly distributed particles $\bar{r_E}$ [145]. The mean nearest neighbor distance can be calculated from the measured distances r by

$$\bar{r_A} = \frac{\sum_{i=1}^{N_A} r}{N_A}, \tag{25}$$

where N_A is the number of particles in the analyzed area. The mean distance between randomly placed neighboring particles can be derived from the homogeneous Poisson process (Equation (20)), giving the probability of finding N points in area $L(A)$. By substituting Poisson parameter $\Lambda L(A)$ to the equivalent expression of $\rho\pi r^2$, the equation can be written as

$$P(N, A) = \frac{[\rho\pi r^2]^N}{N!} e^{-\rho\pi r^2}. \tag{26}$$

The first term in this equation ($[\rho\pi r^2]^N/N!$) determines number of the particles in the area. The second term ($e^{-\rho\pi r^2}$) determines the probability that the area πr^2 contains no points besides the point of origin, which results from $N = 0$. This second term can be concerned as a function of r, giving the proportion of nearest neighbor distances (r_{NND})

$$g(r) = e^{-\rho\pi r^2}, \quad r_{\mathrm{NND}} \geq r. \tag{27}$$

Consequently, the equation can be written as

$$G(r) = 1 - e^{-\rho\pi r^2}, \quad r_{\mathrm{NND}} \leq r. \tag{28}$$

The probability distribution of r can be found from the derivative of $G(r)$

$$G'(r) = \frac{\mathrm{d}G(r)}{\mathrm{d}r} = 2\rho\pi r e^{-\rho\pi r^2}. \tag{29}$$

The mean of nearest neighbor distances of the Poisson process $\bar{r_E}$ can then be integrated from the product of r and $G(r)$ accordingly

$$\begin{aligned} \bar{r_E} &= \int_0^\infty rG'(r)\mathrm{d}r = \int_0^\infty 2\rho\pi r^2 e^{-\rho\pi r^2}\mathrm{d}r \\ &= \frac{1}{2\sqrt{\rho}}. \end{aligned} \tag{30}$$

The relation of $\bar{r_A}$ and $\bar{r_E}$ gives a value R_{CE} which can be used to evaluate the spatial randomness of the particles.

$$R_{CE} = \frac{\bar{r_A}}{\bar{r_E}}. \tag{31}$$

Completely random distribution of particles results in R_{CE} value of 1. If $R_{CE} < 1$ the particles are more aggregated than in random distribution, and if $R_{CE} > 1$ the particles are more widely spaced [145].

The standard error associated with $\bar{r_E}$ can be computed from the second moment of r, called $E(r^2)$

$$E(r^2) = \int_0^\infty r^2 G'(r)\mathrm{d}r = \frac{1}{\rho\pi}. \tag{32}$$

The standard error σ_{rE} is then the square root of the variance $E(r^2) - r_E^2$, that is

$$\sigma_{rE} = \sqrt{\frac{1}{\rho\pi} - \left(\frac{1}{2\sqrt{\rho}}\right)^2} = \sqrt{\frac{4-\pi}{4\pi\rho}}. \tag{33}$$

5 Results and discussion

In this section, the sample characterization and analysis are presented and discussed. First, Section 5.1 describes the development of the photodeposition process during this thesis. Then, Section 5.2 addresses the platinum oxide formation during the photodeposition of platinum. Sections 5.3 and 5.4 introduce and discuss the results from the gold and platinum analysis, respectively. Finally, Section 5.5 compares the differences in the photodeposition of gold and platinum.

5.1 Development of photodeposition parameters

This section describes the phases that led to the utilized process parameters. The possible sources of error during the sample preparation and analysis are discussed. Finally, the effectiveness of the photodeposition mask is analyzed for determining the deposition area.

As discussed earlier, a xenon lamp was used as a light source in this thesis. The xenon lamp was paired with a monochromator that enables the use of a narrow bandwidth of the light. However, the intensity distribution of the incident beam is not well defined. This could affect the kinetics of the deposition as higher intensity of light should result in a larger amount of electron-hole pairs generated. The illuminated areas did not have completely uniform contrast under the SEM which could indicate an irradiation difference inside the illuminated spot. For example, in sample 1.2 at least three areas with different contrasts are observed (Figure 18).

The light source was changed after the first four gold samples (1.1 – 1.4) were fabricated. The change of the light source should not affect the results since the wavelength was determined by the same monochromator and the irradiances were identical. However, the focusing of the light with lenses in the less powerful setup will change the irradiance distribution. In this thesis, it is assumed that the distribution will not affect the photodeposition results significantly, and that the light sources are identical due to the monochromatic light and similar intensities.

The SEM images were analyzed with ImageJ. The image processing with ImageJ is kept as constant as possible through this thesis. This maximizes the repeatability of the sample analysis, and decreases the probability of user errors during image processing. Some errors could occur due to the contrast differences in the TiO_2 surface caused by the grain boundaries. Especially, with smaller particle size the contrast differences between the edges of TiO_2 grains and the nanoparticles are almost negligible. However, by comparing the processed binary image showing the analyzed particles and the original SEM image, the reliability of the analysis can be evaluated. Based on the evaluation, the image processing is made more accurate by adjusting the contrast and/or the brightness of the SEM image. A larger contrast difference resulted in a more reliable particle recognition.

The platinum particles were found to be significantly smaller than the gold particles. Even though the platinum samples were imaged with the more advanced FE-SEM setup, the contrast between the particles and the TiO_2 surface is small. Because of the small contrast difference, the platinum images required more modifying

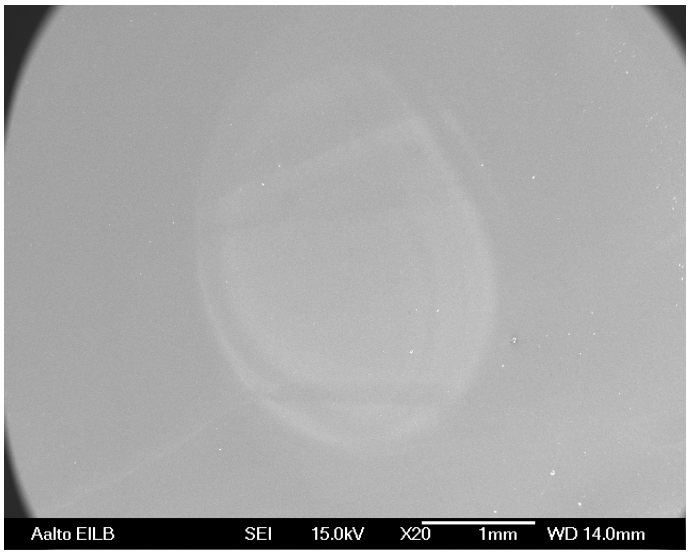

Figure 18: A contrast difference seen in the SEM image of sample 1.2 which could originate from an uneven irradiation from the xenon lamp.

which could result in increased errors. However, it is assumed that the errors are similar for all of the platinum samples, since the particles in all of the samples were equally difficult to detect.

The ALD process was selected for the TiO_2 deposition due to its great conformality and thickness control. However, the ALD process used in this thesis did not produce perfectly uniform coatings. The thickness of the TiO_2 film changed significantly between gas inlet and outlet ends of the ALD reactor. The TiO_2 thickness at the inlet end was close to the desired thickness of 250 nm whereas the thickness in the outlet end was practically zero. A clear indicator of the thickness variation was a colorful line that was visible even to the naked eye. The color of the line was blue/purple turning to red and yellow. The thickness of the TiO_2 layer can be evaluated based on the color. Earlier studies suggest that the blue color indicates thicknesses around 55 nm, and the thickness of the TiO_2 film decreases going towards red and yellow colors (corresponding to thicknesses of 32 nm and 20 nm, respectively) [146].

A SEM image of the substrate cross section was analyzed to evaluate the thickness of the TiO_2 layer (Figure 19). Cross sectional imaging was conducted to a substrate in which the colorful line was visible. The sample was cut for the cross sectional image a few millimeters before the colorful line. The thickness of the TiO_2 layer was around 200 nm. Photodeposition was conducted in this area for the analyzed samples with the visible line. A successful photodeposition was also conducted on top of the colorful line with similar results compared to a sample with thicker TiO_2. The samples which were located closer to the outlet and were bounded by the colorful line were disqualified as the decreased TiO_2 thickness could have affected the photodeposition results.

As the focus in this thesis is in the noble metal photodeposition, there were no resources for the optimization of the ALD process. After obtaining similar results with samples both closer to the inlet and outlet, errors due to variations in TiO_2

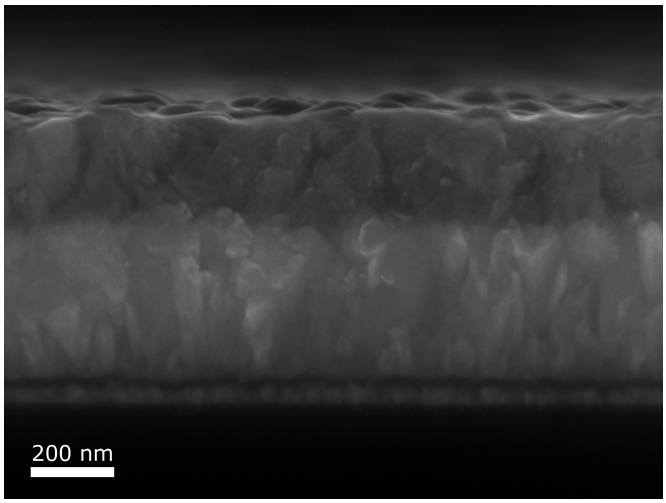

Figure 19: Cross section SEM image of the ALD grown TiO_2 layer. The TiO_2 layer thickness is around 200 nm. Under the TiO_2 layer, the FTO layer, adhesion layer, and the glass substrate are also visible.

thickness were neglected. However, for further studies, the ALD process should be optimized.

Focusing on the photodeposition process, the non-uniform thickness enables the evaluation of the photodeposition kinetics. Based on the photodeposition results on the thinner TiO_2 film, one can conclude that most of the relevant light absorption occurs at the topmost 50 nm of the TiO_2. This implies that the diffusion length of a photogenerated carrier in ALD grown TiO_2 is less than 50 nm. Even as the light travels to greater depths generating electron-hole pairs, the diffusion length of the photogenerated charge carriers is so short, that only the charge carriers generated in the topmost layer can reach the precursor solution and initiate the reduction reaction. Charge carriers that are generated deeper in the TiO_2 recombine before reaching the semiconductor surface.

Sample cleaning before the deposition was found to be a crucial step in order to achieve successful noble metal photodeposition. In the presence of impurity particles on the sample surface, the reduced gold particles nucleate at the edges of the impurities, as seen in Figure 20. SE image allows the detection of singular impurity particles (20a) whereas the contrast difference between gold and impurities, such as dust, is clear on the BSE image (Figure 20b). This is an expected result, since impurities act as active centers for nucleation [117]. Larger impurities can even be completely coated with noble metal, resulting in micrometer-sized gold-coated particles (Figure 21).

In order to prevent this phenomenon from occurring, a substrate cleaning procedure was implemented to the process flow. First, the samples were protected during the storage with a photoresist layer to decrease the amount of impurity particles on the sample surface between the ALD growth and the photodeposition. This also enabled storing the samples for longer times without compromising the cleanliness of the TiO_2 surface. Before the actual sample cleaning was conducted, the photoresist

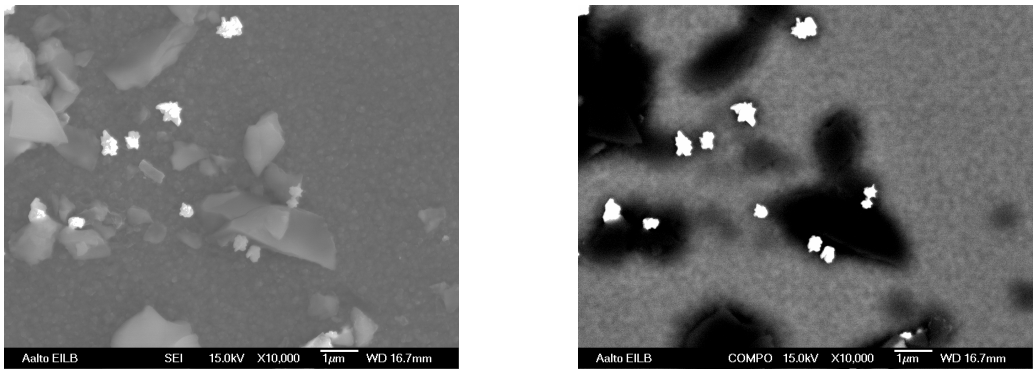

(a) Secondary electron image. (b) Backscattered electron image.

Figure 20: Gold particles nucleate to the edges of impurity particles. (a) Secondary electron image shows the topography of the impurities on top of the substrate. (b) Backscattered electron image highlights the gold particles at the edges of the impurities.

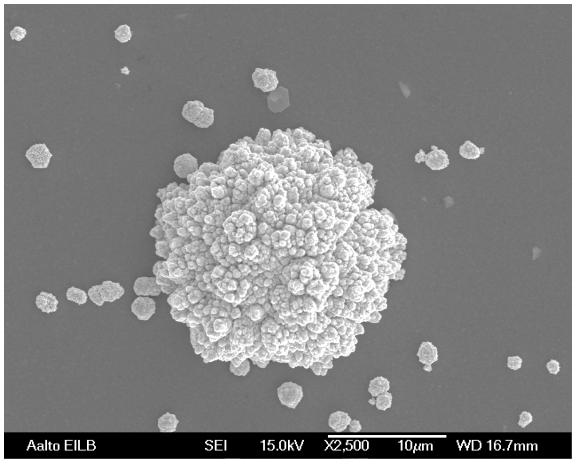

Figure 21: A large impurity particle coated with gold during the UV-illumination.

was removed with acetone. The bare TiO_2 surface cleaning procedure started with acetone ultrasonication followed by ACE, IPA and DIW rinse. This was found to be sufficient for decreasing the amount of impurities on the sample surface.

The UV-wavelength used in the photodeposition is another parameter that needs to be optimized for successful metal reduction. Wavelength of the light should be closely matched with the band gap of the photocatalyst. If the wavelength is too long, the energy of the photons is not sufficient to generate electron-hole pairs. Conversely, if the wavelength is shorter than needed, the extra energy of the photon is lost. The deposition rate of gold was found to be low when using the wavelength of 380 nm. Test samples were prepared with 380 nm wavelength and deposition time of 180 min, resulting in a deposition of a few gold particles, as seen in Figure 22a. The irradiance of the light with the wavelength of 380 nm was around 105 $\mu W/cm^2$. Photodeposition was successful with similar irradiances using a wavelength of 360 nm, using a fraction of the initial deposition time (30 min) (Figure 22b).

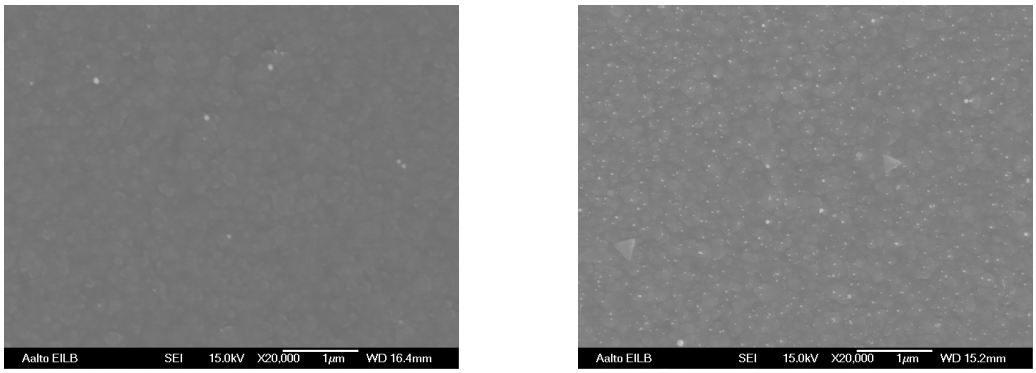

(a) $\lambda = 380$ nm. (b) $\lambda = 360$ nm.

Figure 22: The influence of wavelength to the gold deposition. (a) Deposition with wavelength of 380 nm for 180 min. Only a few reduced particles are found. (b) Deposition with the wavelength of 360 nm for 30 min. The amount of particles clearly increased and the particle size is more uniform.

Based on Figure 22, light with a wavelength of 380 nm does not possess enough energy for efficient photodeposition of metal nanoparticles on TiO_2. Ideally, the wavelength of 380 nm has high enough energy to be absorbed by TiO_2. As discussed before, anatase has a band gap of 3.23 eV, corresponding to the wavelength of 380 nm. The polycrystallinity of the ALD film could affect the light absorption. However, the band gap of ALD grown anatase has been measured to be nearly identical to the band gap energy of single crystal anatase at 3.26 eV [147]. Also, the slow growth of thin films with thickness over 10 nm results in a bulk-like TiO_2 structure so the band gap of the TiO_2 should be comparable to the band gap of bulk TiO_2 [148]. However, the samples presented in Figure 22 imply that the wavelength of 380 nm at the irradiance of 105 $\mu W/cm^2$ was not sufficient enough to generate charge carrier pairs for the photodeposition process. The photon absorption at 380 nm could be so weak that the majority of the absorption occurs deeper in the TiO_2 layer. As the charge carriers are generated at greater depths, they recombine before reaching the TiO_2-electrolyte interface and cannot participate in the reduction reactions. By increasing the photon energy well above the assumed band gap energy, the photodeposition was successfully conducted, while still managing to achieve sufficient irradiance from the xenon lamp.

Even when using the 380 nm wavelength, some gold reduction took place on the substrate (Figure 22a). However, similar particles were also found outside the illuminated area, implying that some spontaneous reduction occurred. Spontaneous reduction of gold on TiO_2 has been reported earlier and it has been attributed to the activity of oxygen vacancies [62]. In this study, spontaneously reduced gold particles, found from the non-illuminated areas of the samples, were typically single isolated particles. The amount of these particles was found to increase with increasing deposition time. In a test sample with a deposition time of 180 min, gold reduction in the non-illuminated area was already distinctive, as seen in Figure 23a. With 30 min deposition time, the amount of spontaneously reduced gold particles decreased significantly (Figure 23b). With 15 min deposition time, the reduction occurred even

less. For the gold samples analyzed in this thesis, the longest deposition time was 30 min so the effect of light on the deposition could be clearly differentiated from the spontaneous deposition. The total time the solution stayed on the substrate was less than an hour for all of the gold samples. For spontaneous gold reduction to be significant, the deposition time should be longer than 180 min. With platinum samples, spontaneous reduction in the non-illuminated area was not detected with deposition times of one or two hours.

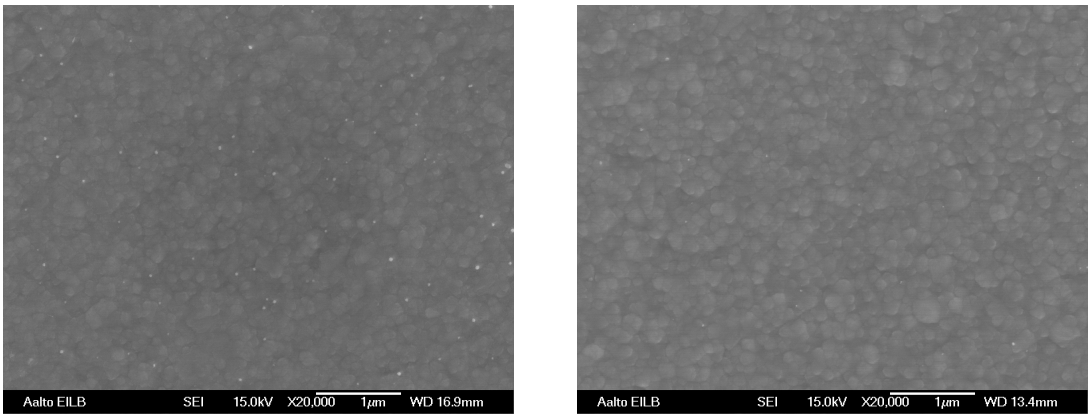

(a) Deposition time: 180 min. (b) Deposition time: 30 min.

Figure 23: Spontaneously reduced gold particles outside the illuminated area. (a) Spontaneous reduction is clearly visible with a deposition time of 180 min. (b) No spontaneous reduction occurs with a deposition time of 30 min.

In Figure 23, the polycrystallinity of the TiO_2 surface is clearly visible. The placement of the spontaneously reduced gold nanoparticles implies that the reduction reaction is more likely to take place at the edges of the brighter areas. The contrast difference originates from the grain structure of the TiO_2 coating, in which the darker areas are grain boundaries between the lighter TiO_2 crystals. Reduction reaction occurs at the grain boundary because nucleation in the grain boundaries requires a smaller activation energy compared to crystalline surfaces [117]. The effect of the grain boundaries diminishes with increasing number of particles. When the number of particles increases, the selectivity of the preferred gold nanoparticle reduction sites seems to decrease, and particles are reduced on both lighter and darker areas, as seen in Figure 22b.

Once the photon energy is sufficient enough to generate charge carriers, deposition occurs only under the illuminated spot. Figure 24a–b compares the illuminated and the non-illuminated areas in the gold deposition, and Figure 24c–d similarly for the deposition of platinum. The figures confirm that the photodeposition process can be confined spatially by using masks, offering an alternative to lithography in nanoparticle deposition. However, if masks are used to define the deposition area, the edge of the illuminated spot is not sharp. The number of particles decreases gradually at the pattern edge until it reaches the point at which only occasional spontaneously deposited particles can be found. The spreading of the deposition pattern occurs due to the diffraction of light at the aperture. The evaluation of the diffraction

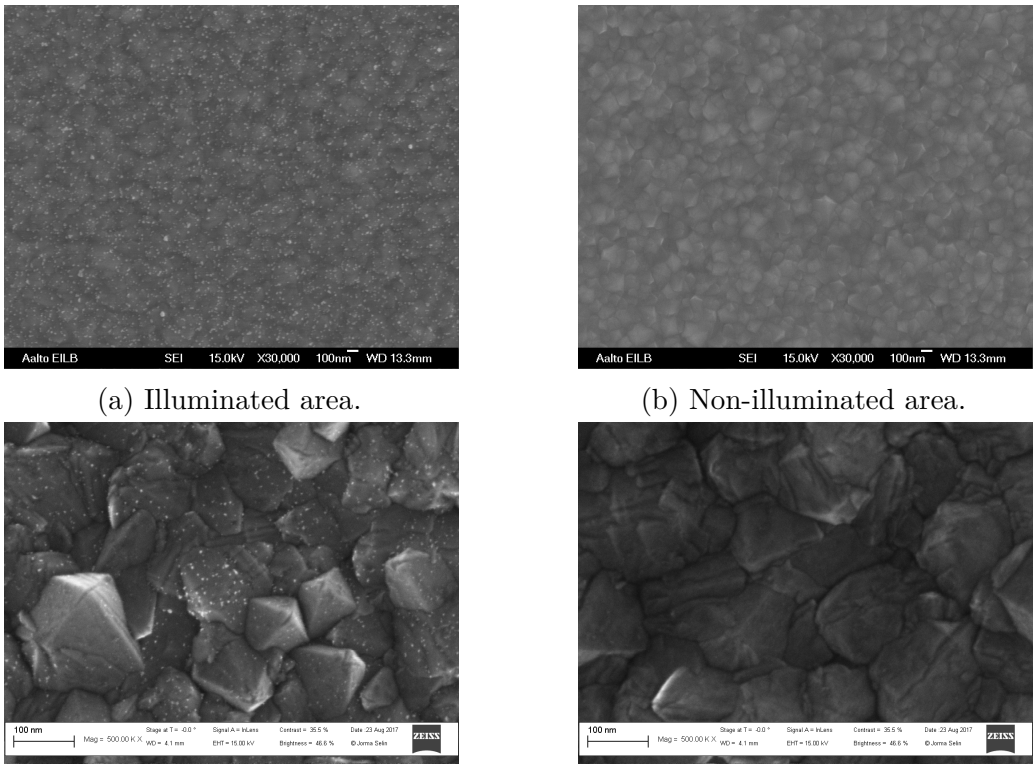

(a) Illuminated area. (b) Non-illuminated area.

(c) Illuminated area. (d) Non-illuminated area.

Figure 24: The comparison of the illuminated and non-illuminated areas in gold (a and b) and platinum (c and d) photodeposition. Magnification in the gold images is 20000 and 500000 in the platinum images. The noble metal reduction occurs only in the illuminated spot, so masks can be efficiently be used to determine the deposition area.

effect is difficult because the light source does not provide uniformly distributed irradiation, leading to intensity variations also inside the spot area. The deposition pattern is further spread by electron diffusion [149]. However, with polycrystalline TiO_2 coatings, electron diffusion lengths are presumably short, as dislocations and grain boundaries increase the recombination rate of charge carriers.

5.2 Oxidation of photodeposited platinum

In this section, the oxidation of the platinum during the photodeposition is addressed. The circumstances that lead to the deposition of platinum oxide are presented. Lastly, the oxide formation reactions and kinetics are analyzed.

Platinum photodeposition in the pH of 7 resulted in two distinctly different phases which are metallic and oxidized phase, seen in Figure 25. Similar results have been reported earlier [120–122]. The oxidized phase resembled mycelia that covered wide areas in the illuminated spot (Figure 25a–c). The metallic phase contains separate platinum particles, similar to the photodeposited gold particles (Figure 25d). According to earlier studies, the platinum oxide at pH 5–7 is in the form of PtO [121].

When the pH is increased to the range of 7–9, the oxides form a mixed phase of PtO and PtO_2. The precursor solution used in this thesis is slightly acidic due to the acidic precursor salt, making PtO the most likely oxide. Oxide formation is observed on every platinum sample that was prepared at pH 7. According to Zhang *et al.* [121], the PtO is formed from the hydrolysis of the precursor

$$PtCl_6{}^{2-} + 2\,OH^- \longrightarrow Pt(OH)_2Cl_4{}^{2-} + 2\,Cl^-, \tag{34}$$

which then reacts with photogenerated electrons

$$Pt(OH)_2Cl_4{}^{2-} + 2\,e^- \longrightarrow PtO + H_2O + 4\,Cl^-. \tag{35}$$

The amount of platinum oxide is found to depend on the process parameters. In some samples, the oxidized platinum is gathered in large round shapes that could be seen brighter in the SEM images. With naked eye, the areas with platinum oxide can be seen as darker spots in the illuminated area. For the samples with less platinum oxide, the oxide is found everywhere in the illuminated area as small islands. Metallic platinum is also found on all of the samples. Oxidized metal is only found in the platinum samples prepared at pH 7, not in the lower pH platinum samples or in any of the gold samples which is also in line with previous studies [93, 150].

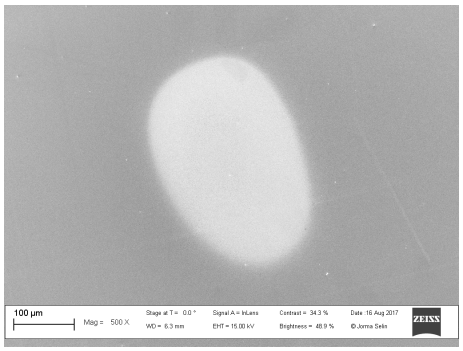

(a) Platinum oxide.

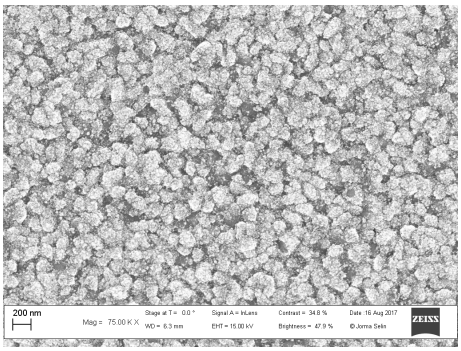

(b) Platinum oxide.

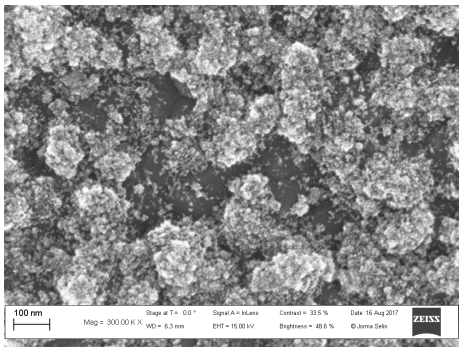

(c) Platinum oxide.

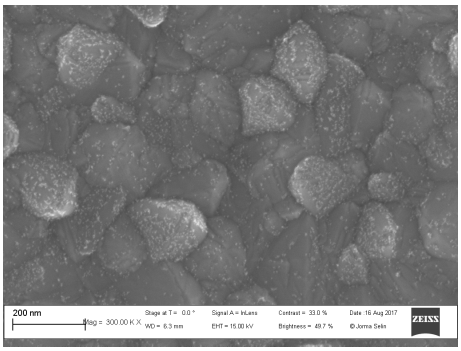

(d) Metallic platinum.

Figure 25: The oxide formation in platinum sample 2.1 prepared at pH 7. (a) The oxidized area appears brighter in the SEM image. (b) The platinum oxide forms grows densely on the TiO_2 surface. (c) The platinum oxide covers the TiO_2 grains efficiently. (d) Metallic particles found outside the bright area.

Two different paths of platinum oxide formation are detected in the samples (Figure 26). The oxides can grow in a mycelium type growth, in which long lines of platinum oxide is formed (Figure 26a). The oxide can also form small clusters which will then start to spread, as seen in Figure 26b. However, the determination of the oxide growth mechanism is not in the scope of this study.

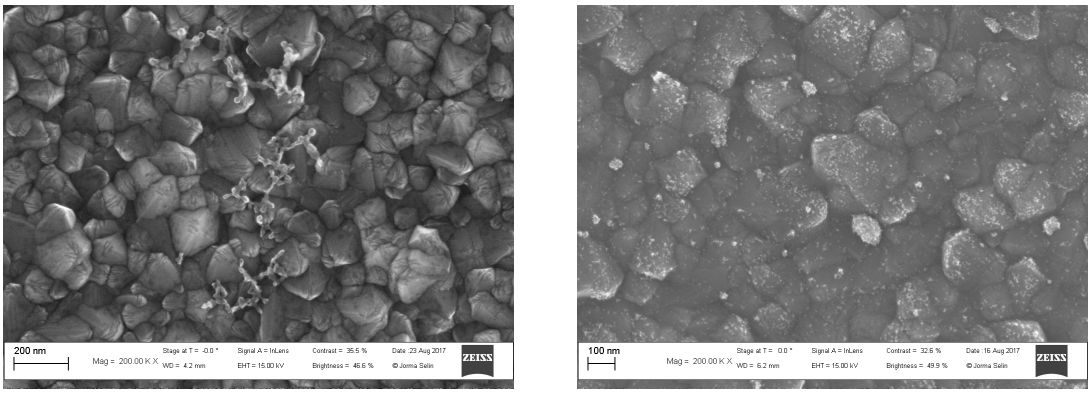

(a) Mycelium growth. (b) Cluster growth.

Figure 26: The two different types of oxide growth observed in the platinum samples. Both of the images have the same magnification of 200000x.

The formation of platinum oxide decreases the accuracy of the platinum analysis significantly. In order to conduct the analysis for the samples, the oxidized platinum samples and metallic platinum samples are processed as if they were identical. This is justified, since previous studies have proven that the oxidized samples also contain metallic platinum [121]. The analysis is conducted on areas without the oxidized platinum. However, there is no certain way to determine whether the platinum nanoparticles in the analyzed area are actually metallic. Characterization method selection for detecting the oxygen bonded to the platinum is limited by the small size of the particles. For surface active methods, the difficulty is also to distinguish the oxide peaks between the oxygen bonded to platinum and the oxygen bonded to titanium dioxide.

The oxidized areas are visible in the SEM images for samples 2.1, 2.4 and 2.7 (Figures 27a, b and d, respectively). For sample 2.6 (Figure 27c), the platinum oxidation is not as distinct. However, with larger magnifications the faces of the TiO_2 grains appeared to be rough, which is not seen in any of the samples prepared at pH 4. This led to the conclusion, that the roughness originated from the early stages of oxide growth, since the oxide surface appears to be rough and mycelium-like.

As seen from the Figure 27, the amount of oxide is dependent on the process parameters. The area of visible platinum oxide is analyzed with ImageJ. The sample 2.1 has the largest area of the oxide at 1.87 mm^2. The second largest oxide formation is found in the sample 2.4 (0.28 mm^2), and the third largest at the sample 2.7 (0.19 mm^2). The sample 2.6 did not have any of the recognizable oxide at low magnification. The size of the illuminated area in each of the samples is 15.2 mm^2. The relative areas of the oxidized platinum appear to be small, but

the oxide formation is also found in smaller proportions in other areas. This causes challenges to the determination of the absolute amount of platinum oxide on the sample.

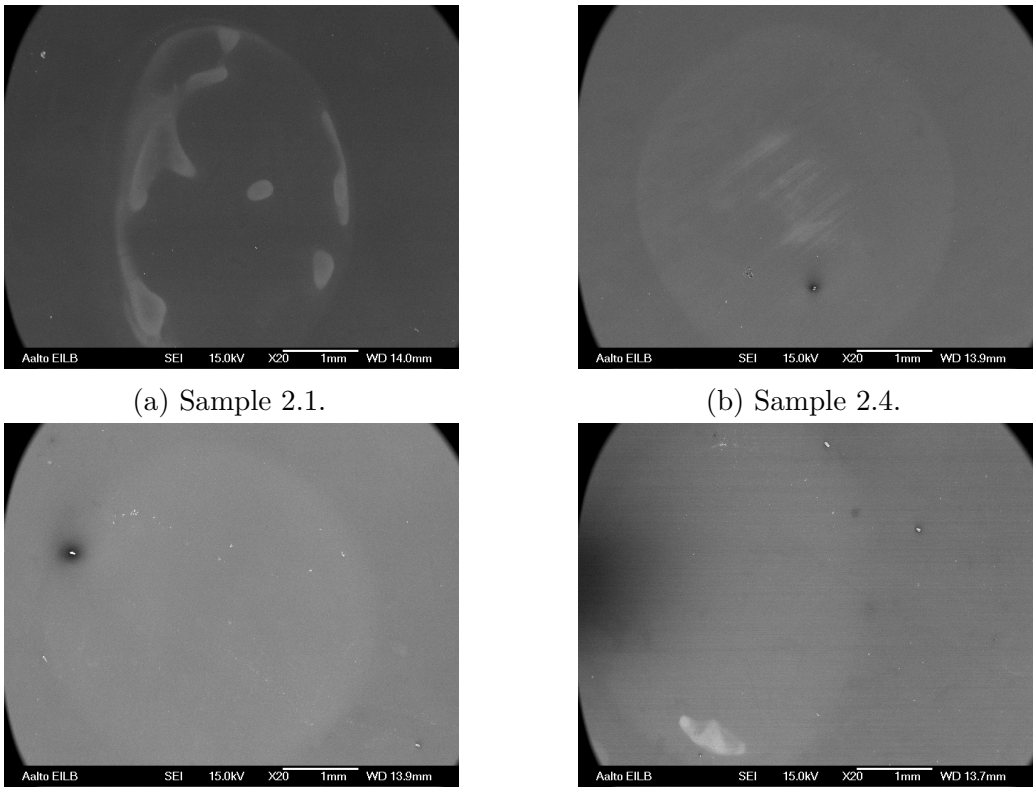

(a) Sample 2.1. (b) Sample 2.4.

(c) Sample 2.6. (d) Sample 2.7.

Figure 27: Platinum oxide formation on samples prepared at pH 7. The bright areas seen in the SEM images show the densely packed oxidized areas. The metallic platinum nanoparticles are found in the darker area of the spots.

The oxide formation seems to take place mostly at the edges of the pattern, as seen in Figures 27a and d. This could occur due to the intensity variation of the xenon lamp. The other possibility is, that the edges of the pattern can access to larger amount of platinum ions due to diffusion. The oxide formation seems to consume the platinum at higher rate than the metallic platinum formation. The edges could benefit from the fact that all of the photogenerated reactions occur at the illuminated area, while the solution is evenly distributed over the whole sample. As the platinum ions react under the illumination, their local concentration decreases at the illuminated area. This results in ion diffusion from the high concentration areas towards the illuminated spot. The diffusion brings more ions to the edges of the spot where they can react with photogenerated electrons and be reduced to PtO according to Equation (35).

5.3 Photodeposition of gold

In this section, the analysis of gold samples is conducted. The analysis is based on SEM images and data obtained from ImageJ image processing. Individual samples are characterized and analyzed first, followed by discussion on the influence of different variables used in this thesis.

5.3.1 Particle sizes and nearest neighbor distances

Figure 28 shows representative SEM images of the illuminated areas for samples 1.1 – 1.8 (28a – 28h, respectively). The influence of variables on the photodeposition is distinct even from the SEM images at 50000x magnification. Sample 1.5 (Figure 28e) has clearly the largest particle size of all the samples. On the other hand, it also has the least particles deposited along with samples 1.4 and 1.6 (Figures 28d and 28f). In sample 1.4 (28d), the photodeposition was not successful, and only two gold particles can be distinguished from the area. The parameters that led to the failure of sample 1.4 are discussed later on in Section 5.3.3.

SEM images shown in Figure 28 were analyzed with ImageJ, and the resulting particle size distributions are shown in Figure 29. Overall, the log-normal distribution fits to the particle size data well. Log-normal distribution cannot be fitted to the data of sample 1.4 because of the limited data. Only with sample 1.5 (Figure 29e), the fitted curve clearly differs from the data due to the small number of analyzed particles. When the particle density of the sample increases, the goodness of the fit increases. The largest differences between the data and the fit originate from the surplus of small particle diameters. This effect is most apparent with samples 1.2, 1.6 and 1.8 (Figures 29b, 29f and 29h, respectively). The average particle size can be approximated from the peak of the log-normal curve. Typical diameters for the particles are around 20 nm, with the exception of sample 1.5 in which the peak is around 40 nm.

Nearest neighbor distances are analyzed from the same SEM images as the particle size distributions, and the results are presented in Figure 30. The red lines represent the distribution of completely spatially random particles, as derived in Equation (23). The fitted curve seems to follow the data well, even though the peak frequencies on all samples exceed the fitted curve. The data points behave similarly to the fitted curve for the long distances. Also, the slope of the curve seems to fit the data well, as it is dependent on the particle density of the sample. This can be detected by comparing the data of samples 1.1 and 1.5 (Figures 30a and 30e). Sample 1.1 had the largest particle density, resulting in a steep rise to the peak value, while in sample 1.5 the density is low, as is the steepness of the fit. Similar to the particle size data, an increase in the amount of data points (*i.e.* the particle density) results in a better fit.

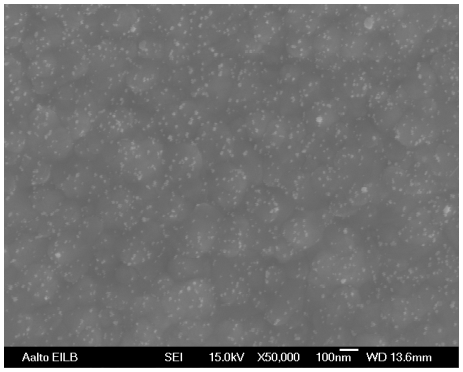

(a) Sample 1.1.

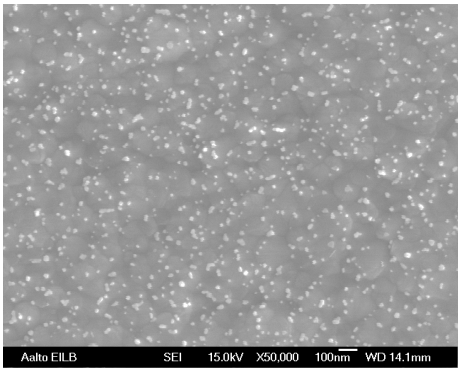

(b) Sample 1.2.

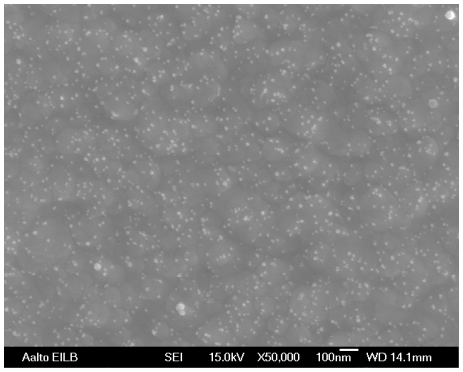

(c) Sample 1.3.

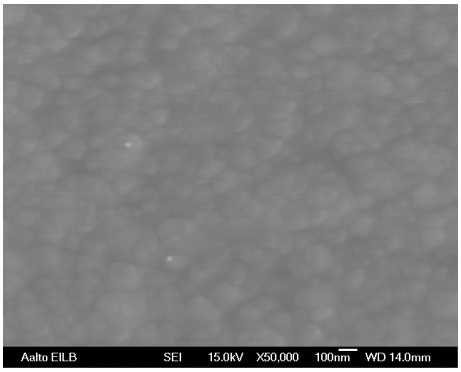

(d) Sample 1.4.

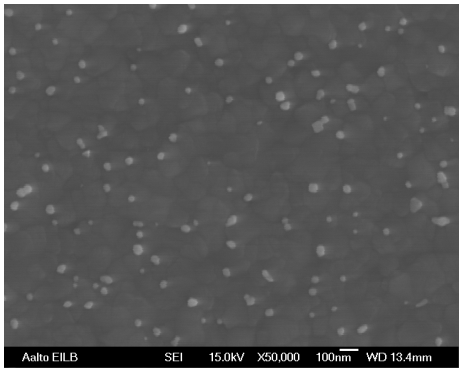

(e) Sample 1.5.

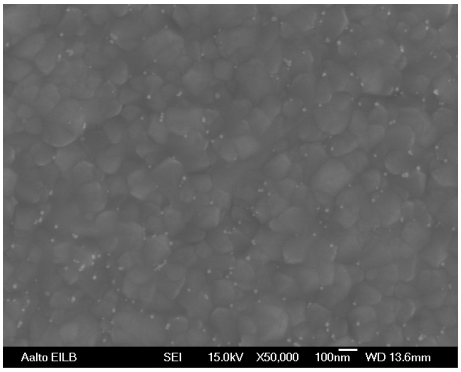

(f) Sample 1.6.

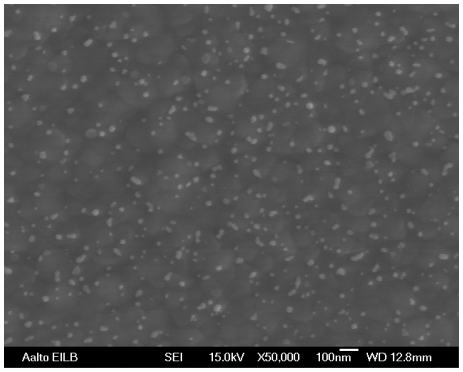

(g) Sample 1.7.

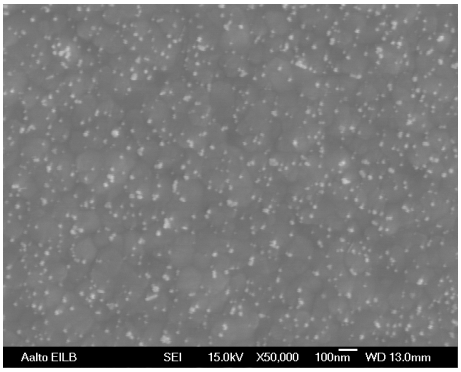

(h) Sample 1.8.

Figure 28: SEM images of the deposited gold particles.

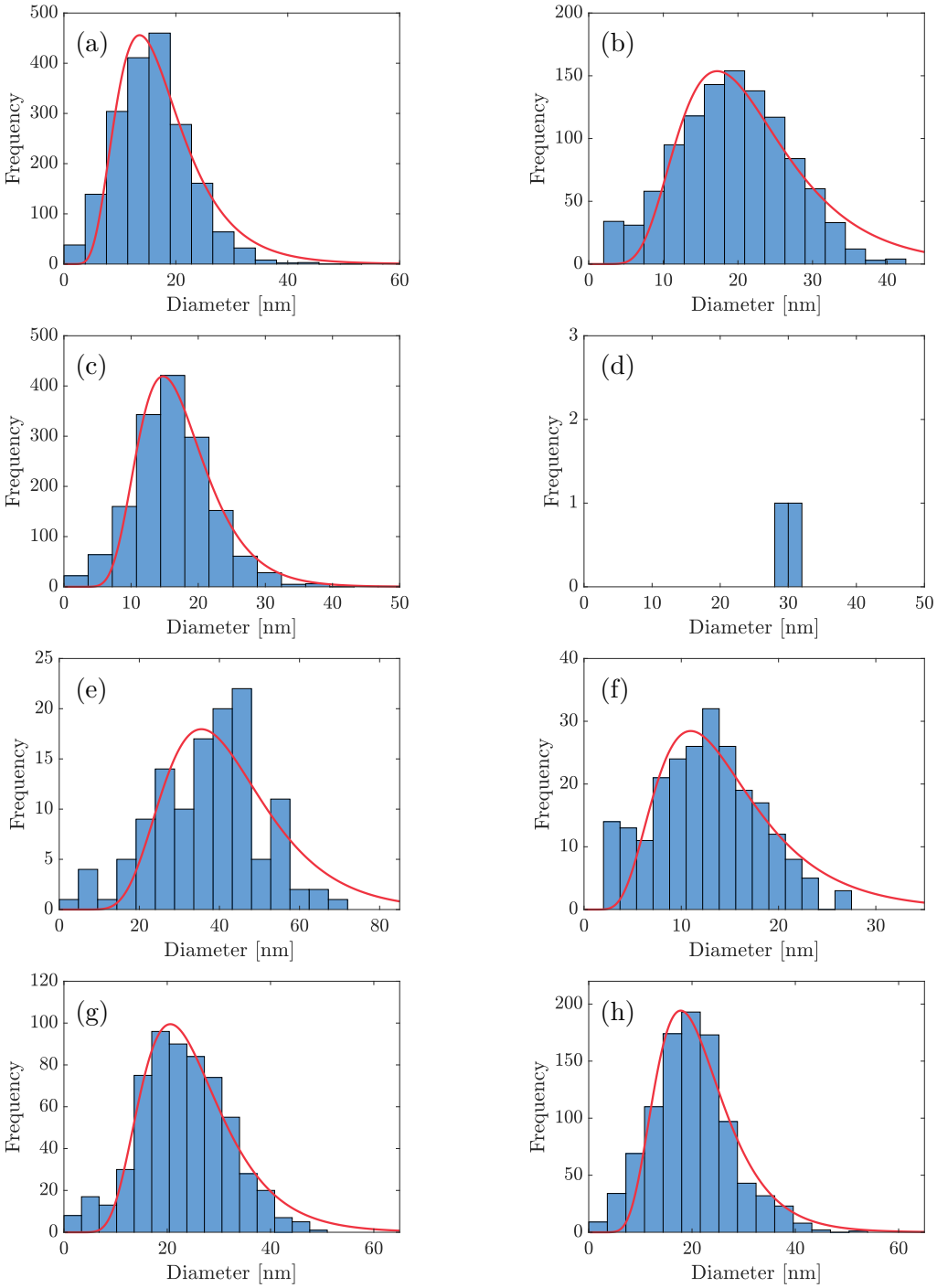

Figure 29: The particle size statistics of the deposited gold particles on samples 1.1–1.8 ((a)–(h), respectively). The log-normal distribution, seen in red, is fitted to the measured data.

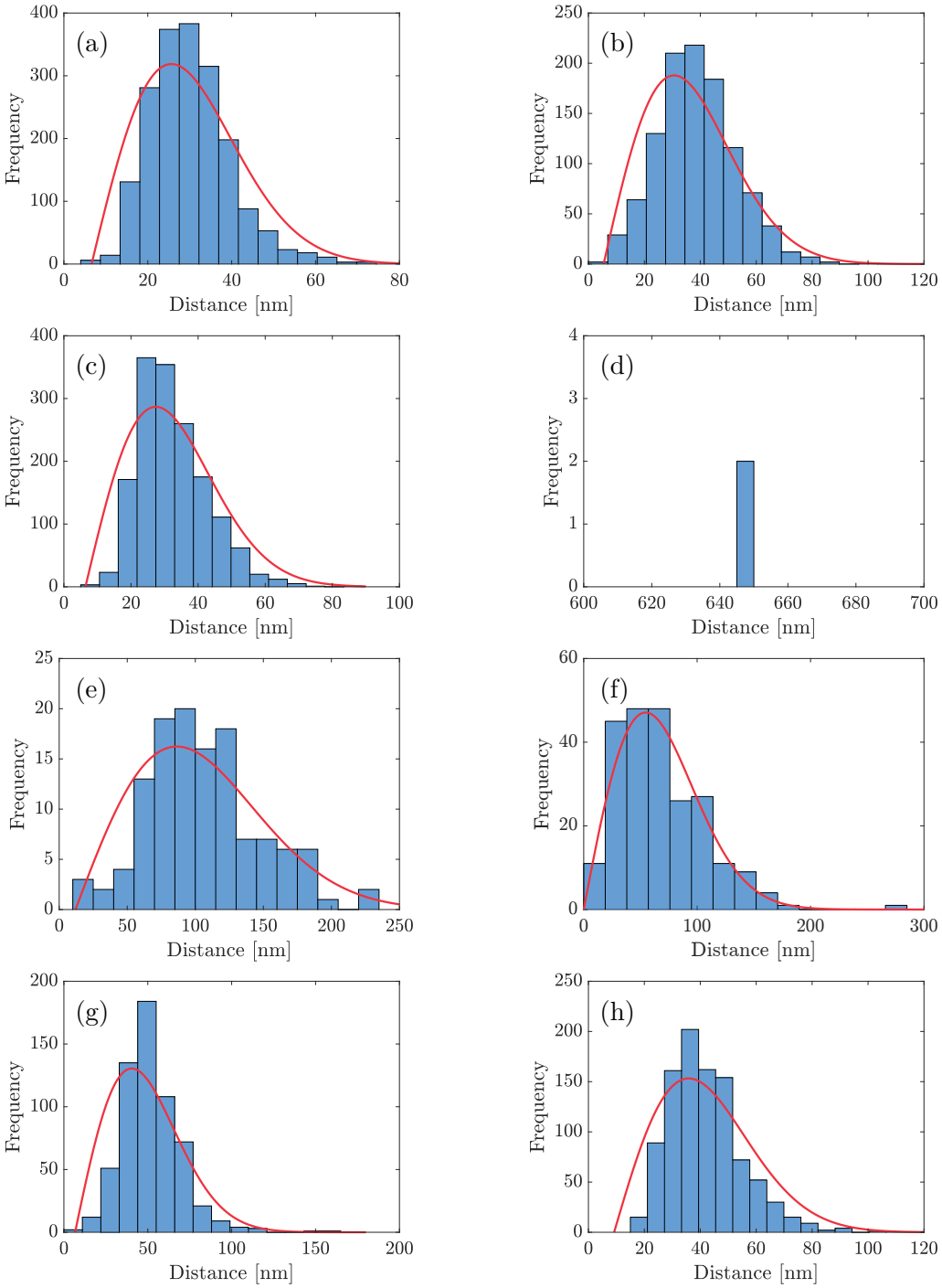

Figure 30: The nearest neighbor distance statistics of the deposited gold particles on samples 1.1–1.8 ((a)–(h), respectively). The spatially random distribution, seen in red, is fitted to the measured data.

5.3.2 Characteristic values in the photodeposition of gold

The parameters used in the photodeposition of gold are collected in Table 4. The results from the particle size analysis (Figure 29) and nearest neighbor distance (Figure 30) are collected in Tables 5 and 6, respectively. Indicator values are calculated from the same data which the histograms were plotted. Due to the unsuccessful photodeposition on sample 1.4, it is not comparable to the other samples, making the calculated statistics of sample 1.4 irrelevant in this context. The sample 1.4 will be analyzed later on, when the influence of different parameters is discussed.

Table 4: Parameters used for the gold samples in this thesis.

	Sample							
Parameter	1	2	3	4	5	6	7	8
H_2 treatment	No	No	No	No	Yes	Yes	Yes	Yes
CH_3OH vol-%	5	5	10	10	5	5	10	10
Illumination P [µW]	70	70	35	35	35	35	70	70
Deposition t [min]	30	15	30	15	30	15	30	15
Precursor C [mg/ml]	1	2	1	2	2	1	2	1
N_2 purging t [min]	30	15	15	30	30	15	15	30
pH	7	4	4	7	4	7	7	4

The density (ρ) differences achieved with different photodeposition parameters are significant. Sample 1.1 has clearly the highest gold particle density (440.05 μm^{-2}) whereas sample 1.5 has the lowest (28.70 μm^{-2}). Thus by changing the variables, the particle density can be adjusted in a wide range. As seen in Table 5, the mean particle diameter ($\bar{d}$) is considerably larger for sample 1.5 (37.25 nm), which could already be seen from the SEM images (Figure 28). The particles are indeed over one and a half times larger than the second largest average particle size (23 nm with sample 1.7). Sample 1.6 possesses the smallest average particle diameter. Average particle diameters are between 15 nm and 20 nm for the other samples. Apart from sample 1.6, the average diameters increase with decreasing particle density. This could indicate that gold particles grow through Ostwald ripening -type of effects, in which the small particles are dissolved over time to enable the growth of larger particles.

The mass of the gold per area m_A is calculated by approximating all of the particles to be hemispherical and multiplying the calculated volume with the density of gold. The masses are similar for samples 1.1, 1.2 and 1.8 even though the particle densities vary significantly. Otherwise, the masses of gold tend to decrease with decreasing particle density. The only exception to this is sample 1.3, which has the second highest particle density, but only the fifth highest mass.

For all samples, median particle diameters (M) were similar to mean particle diameters. This indicates that there is only a slight skewness on the data, as the log-normal fit suggests. Variance (σ^2) and standard deviation (σ) indicate the variation of the data from the mean value. As expected, the smaller average diameter yields a

smaller standard deviation and tighter distribution of the particle sizes. The standard deviation remains quite constant, at around one third of the average diameter for all of the samples, indicating that the shape of the distribution in photodeposition will stay constant, independent of the particle size.

Overall, most of the distributions are close to the log-normal distribution, indicated by R^2 values close to 1. It can be seen, that the R^2 values approach the value of 1 as the particle densities increase. For sample 1.5, the log-normal distribution is a bad fit ($R^2 = 0.689$) but the R^2 value increases with the density, and R^2 values close to or over 0.9 are achieved with the densely deposited samples. With high densities, the random variation of particle sizes is not as significant, resulting in a better fit.

Table 5: Comparison of the particle size statistics of the gold deposition.

Sample	ρ [μm^{-2}]	$\bar{d}$ [nm]	m_A [ng/mm^2]	M [nm]	σ^2 [nm^2]	σ [nm]	R^2
1.1	440.05	15.86	13.87	15.50	43.78	6.62	0.951
1.2	250.93	19.31	13.25	19.22	55.91	7.48	0.896
1.3	361.81	16.26	11.28	16.07	35.66	5.97	0.976
1.4	0.46	30.03	0.06	30.03	0.56	0.75	–
1.5	28.70	37.25	10.17	38.70	172.00	13.11	0.689
1.6	53.47	12.54	0.82	12.60	28.00	5.29	0.699
1.7	139.58	23.00	12.26	22.53	74.71	8.64	0.956
1.8	224.07	19.88	13.07	19.63	58.80	7.67	0.937

The nearest neighbor distance statistics are presented in Table 10. The average distance between neighboring particles ($\bar{r_A}$) decreases with increasing particle density, as expected. It indicates that the particles are distributed quite evenly throughout the samples. The median (M) values are systematically smaller than the mean distances, as the fitted completely spatially random distribution would suggest. The standard deviation (σ) is around one third of the average value, similarly to the particle size statistics. Samples 1.5 and 1.6 have larger standard deviations. However, this should be expected, since these samples have the smallest particle densities, so the nearest neighbor distances will have larger variations. The fitted curve does not match perfectly with the experimental data. R^2 values are below 0.9 for most of the samples except for the sample 1.3. Based on the plotted data (Figure 30), the peak values of the data exceed the peak of the fitted curve. The shape of the curve, however, is similar to the data. It can be deduced, that the particles are not completely randomly distributed, even though there is no clear indication of preferred reduction sites either.

In order to investigate the randomness of the particle distribution, a Clark-Evans test was conducted from the nearest neighbor data, as described in Chapter 4. The results of the Clark-Evans test are collected to Table 7. The most important value in the table is R_{CE} which is given by the ratio of the measured average nearest neighbor distance ($\bar{r_A}$) and the average nearest neighbor distance of completely randomly distributed particles $\bar{r_E}$. The value of 1 for R_{CE} would indicate a perfectly spatially random particle distribution. According to the measurements, complete randomness

Table 6: Comparison of the nearest neighbor distance statistics of gold particles.

Sample	ρ [μm^{-2}]	$\bar{r_A}$ [nm]	M [nm]	σ^2 [nm^2]	σ [nm]	R^2
1.1	440.05	30.16	28.96	91.72	9.58	0.878
1.2	250.93	38.67	37.48	190.14	13.79	0.893
1.3	361.81	32.42	30.72	105.99	10.30	0.996
1.4	0.46	645.28	645.28	0	0	–
1.5	28.70	106.17	103.41	1736.73	41.67	0.798
1.6	53.47	67.54	61.18	1469.77	38.34	0.851
1.7	139.58	51.84	49.18	307.92	17.55	0.833
1.8	224.07	41.79	40.11	168.09	12.97	0.853

can only be observed with the sample 1.6. With all the other samples, the R_{CE} value is larger than 1, indicating that the distances between neighboring particles are larger than in a completely random case. When the particle size increases, the particles are more evenly spread throughout the sample. There are two possible explanations for this. First, particle size focusing effects such as Ostwald ripening affects the particle distribution. As the deposition progresses, the small and unstable particles are dissolved, whereas the gold ions are reduced to the existing larger particles [117]. The reduction reactions are energetically favored on the existing particles since the gold particle growth is autocatalytic. The amount of gold ions available for the autocatalytic reaction increases if the distances to neighboring particles are long, as all the particles are competing for the same ions. Thus, particle growth benefits from long nearest neighbor distances.

Another explanation for the particle distribution in photodeposition of gold is the influence of oxygen vacancies at the TiO_2 surface. As discussed previously in Section 2.2, the oxygen vacancies have a large role as the active sites for metal reduction reactions. Large gold particles can only be stabilized by multiple oxygen vacancies [63]. As the vacancies are gathered as clusters to stabilize the large gold particle, the area around the particle is depleted from oxygen vacancies. This causes the distances between neighboring particles to be larger than in the case of randomly distributed particles, as the randomly distributed unstable gold clusters are diffused to a certain location with higher defect density.

The error for the R_{CE} in this analysis is small. Standard error σ_{rE} indicates the error of $\bar{r_E}$. Compared to the value of $\bar{r_E}$, the magnitude of σ_{rE} is insignificant and will not affect the value of R_{CE} (apart from the sample 1.4). Similar to the standard deviation, the σ_{rE} decreases with increasing particle density.

5.3.3 Comparison of photodeposition parameters

Results from the analysis conducted above indicate that the selected parameters have a distinct influence on the photodeposited gold nanoparticles. In order to distinguish the effects of single parameters, the results of the photodepositions are gathered to tables below, and organized based on particle density (Table 8), particle size

Table 7: Clark-Evans test statistics of the deposition of gold particles.

Sample	ρ [μm^{-2}]	$\bar{r_A}$ [nm]	$\bar{r_E}$ [nm]	R_{CE}	σ_{rE} [nm]
1.1	440.05	30.16	23.84	1.27	0.29
1.2	250.93	38.67	31.56	1.23	0.50
1.3	361.81	32.42	26.29	1.23	0.35
1.4	0.46	645.28	734.85	0.88	271.61
1.5	28.70	106.17	93.33	1.14	4.38
1.6	53.47	67.54	68.38	0.99	2.35
1.7	139.58	51.84	42.32	1.22	0.90
1.8	224.07	41.79	33.40	1.25	0.56

(Table 9), and nearest neighbor distance (Table 10). The influence of the parameters on density, particle size, and nearest neighbor distance can be evaluated based on the measurements, as presented previously in Section 4.2. The parameter values 1 for all of the variables are colored in blue. If the majority of one of the parameters is located at the top half of the table, separated by a dash line, one can conclude that the parameter is beneficial considering photodeposition of small particles and with high particle density.

In Table 8, the samples are arranged from the highest particle density to the lowest. According to the results, it seems that the most influential variables considering the particle density are H_2 thermal treatment, light intensity, precursor concentration and the solution pH. As was already evident from the SEM images, the H_2 treatment seems to decrease the particle density. In order to achieve densely reduced gold particles, the UV-light intensity should be high. The higher intensity light contains a larger number of photons, which generate electron-hole pairs resulting in gold reduction reactions on the semiconductor surface.

Increasing precursor concentration seems to decrease the particle density. This implies that the nucleation process is not limited by the amount of precursor available (diffusion limited) but rather by the reaction kinetics. Even with the lower precursor concentration (1 mg/ml), there are enough gold ions for the reduction reaction to occur efficiently. This result is in line with previous studies, where the reaction rate of photodeposition was found to be dependent on the precursor concentration only with small concentrations [125]. The lower pH value also seems to increase the particle density. As previous studies suggests, pH lower than the IEP of TiO_2 causes a positive charge to the surface, which attracts the negative ions to the surface [121].

In Table 9, the samples are arranged from the smallest particle diameter to the highest. Once again, four variables are found to have an effect to the particle size: H_2 treatment, sacrificial CH_3OH concentration, precursor concentration and N_2 purging time. H_2 pretreatment seems to increase the particle size. The larger particle size could also explain the decrease in the particle density after H_2 treatment. The oxygen vacancies created in the H_2 treatment could increase the gold reduction reaction rate, because of the increased amount of active sites [47]. As the reactions occur faster, the particles have more time for the actual growing process. As discussed before,

Table 8: Influences of variables to the gold particle densities.

		Variable						
Sample	ρ [μm^{-2}]	H_2	CH_3OH	Intensity	Time	Precursor	N_2 time	pH
1.1	440.05	1	1	2	2	1	2	2
1.3	361.81	1	2	1	2	1	1	1
1.2	250.93	1	1	2	1	2	1	1
1.8	224.07	2	2	2	1	1	2	1
1.7	139.58	2	2	2	2	2	1	2
1.6	53.47	2	1	1	1	1	1	2
1.5	28.70	2	1	1	2	2	2	1
1.4	0.46	1	2	1	1	2	2	2

the small nanoparticles are more unstable, making the nucleation of new particles unfavorable, and resulting in the growth of large gold clusters. Another possibility is that the large number of oxygen vacancies created by the H_2 treatment can stabilize large particles and make them more stable.

The masses of gold on the H_2 treated samples are actually slightly smaller compared to the non-treated samples, as shown earlier in Table 5. It is possible, that the photodeposition process will slow down after a certain loading. There are two possible reasons for the increased loading to decrease the light absorption: (1) the shadowing of the existing particles on the photocatalyst surface or (2) the tendency of larger gold clusters to act as recombination centers for the photogenerated charge carriers [16].

The particle size is also detected to increase with increasing amount of sacrificial donor. According to earlier studies, the sacrificial agent was found to form radicals during the photodeposition, which can provide even more electrons to the reduction reaction [131]. In the study, the dispersion of platinum nanoparticles increased with increasing sacrificial donor concentration but no conclusions considering the particle size were made. However, similar reaction can be assumed to occur in the photodeposition of gold, and it could result in the increase of particle size.

Increasing precursor concentration will also increase the particle size. Results with the precursor concentration are similar to the H_2 treatment considering the behavior of particle size and density. When the particle size increases with increasing precursor concentration, the particle density decreases. This could indicate that the photodeposition has proceeded further with the higher concentration, and only the larger and more stable particles remain on the semiconductor surface.

The fourth variable that seems to affect the particle size in photodeposition is N_2 purging time. According to the data, there is a difference between the purging times of 15 min and 30 min. The reason for the N_2 purge is to remove the dissolved oxygen from the solution to decrease the amount of electrons scavenged by dissolved O_2 [115]. The results suggest, that the dissolved oxygen was not sufficiently removed during the 15 min purge.

Table 9: Influences of variables to the gold particle sizes.

		Variable						
Sample	$\bar{d}$ [nm]	H_2	CH_3OH	Intensity	Time	Precursor	N_2 time	pH
1.6	12.54	2	1	1	1	1	1	2
1.1	15.86	1	1	2	2	1	2	2
1.3	16.07	1	2	1	2	1	1	1
1.2	19.31	1	1	2	1	2	1	1
1.8	19.88	2	2	2	1	1	2	1
1.7	23.00	2	2	2	2	2	1	2
1.4	30.03	1	2	1	1	2	2	2
1.5	37.25	2	1	1	2	2	2	1

In Table 10, the samples are arranged from the shortest nearest neighbor distance to the longest. The table is identical to the particle density table presented earlier (Table 8). This is expected, since there were no significant differences in the nearest neighbor distance distributions between the samples. With similar distributions, larger particle densities will result in shorter nearest neighbor distances. There were some difference in the distributions when evaluating it with R_{CE} value determined in the Clark-Evans test (Table 7) for samples with lower particle densities, but the density differences were so large that the possible variations in particle distributions will not show on the NND data. Additionally, the differences seen in R_{CE} value for sample 1.4, 1.5 and 1.6 are most probably due to small sample size rather than actual distribution difference. Based on the nearest neighbor distance it can be concluded that the photodeposition variables do not effect the particle distribution.

Table 10: Influences of variables to the nearest neighbor distance of the gold particles.

		Variable						
Sample	$\bar{r_A}$ [nm]	H_2	CH_3OH	Intensity	Time	Precursor	N_2 time	pH
1.1	30.16	1	1	2	2	1	2	2
1.3	32.42	1	2	1	2	1	1	1
1.2	38.67	1	1	2	1	2	1	1
1.8	41.79	2	2	2	1	1	2	1
1.7	51.84	2	2	2	2	2	1	2
1.6	67.54	2	1	1	1	1	1	2
1.5	106.17	2	1	1	2	2	2	1
1.4	654.28	1	2	1	1	2	2	2

In order to further evaluate the influence of a single variable, averages of particle density, particle size and nearest neighbor distance are calculated for both parameter values for each variable, as presented previously in Section 4.2. These values were plotted on Figures 31–33, respectively. The figure allows the detection of the

magnitude of the change when each variable value is changed. Sample 1.4 is dismissed from the data, since the averages would be skewed by this unsuccessful sample.

Figure 31 presents the dependence between the variables and particle densities. As it can be seen, similar trends can be observed as in Table 8 presented earlier. The largest changes occur when H_2 thermal treatment, precursor concentration or light intensity is changed. H_2 treatment has the most significant effect on the particle density, decreasing it from around 350 μm^{-2} to 110 μm^{-2}. The magnitudes of change for the precursor concentration and light intensity seem to be quite similar, but the directions are opposite. Increasing deposition time, donor concentration and N_2 purging time appear to slightly increase the particle density. In contrast to the previous analysis, the pH of the solution seems to have no effect on the average particle densities. However, the particle density values change on a large scale throughout the analysis, so even one sample with low particle density affects the average density significantly. The pH values show no change in the particle density because the highest particle density is achieved with the higher pH of 7 and the lowest analyzed particle density is achieved with the lower pH of 4.

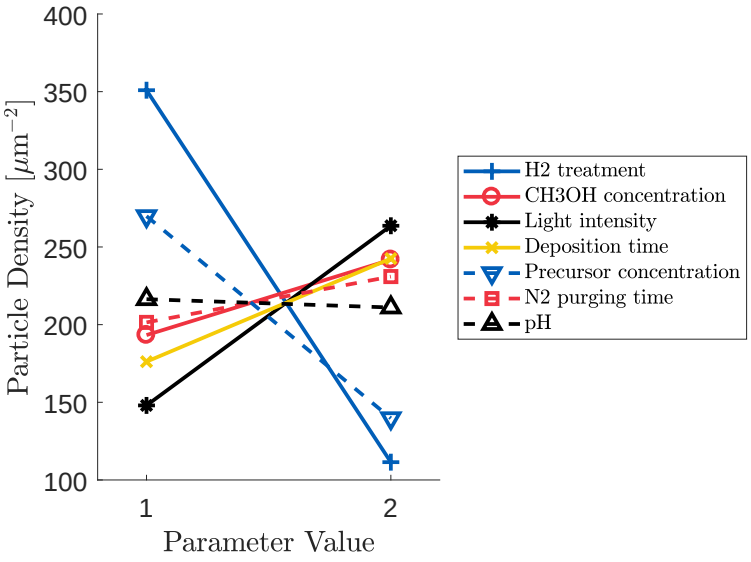

Figure 31: Influence of the variables to the particle density of gold.

Figure 32 presents the dependence between the variables and particle sizes. The trends are similar to the once observed earlier in Table 9. The increasing precursor concentration seems to have the largest effect on the growing of the particle size. The N_2 purging time, deposition time and the H_2 treatment have almost identical effects to the growth of the particle size. Light intensity and the sacrificial donor concentration have no influence to the particle size.

Figure 33 presents the dependence between the variables and nearest neighbor distances. The order of the lines is similar (but opposite) to the one presented in the particle density figure (Figure 31), as expected. However, the methanol concentration seems to have a larger effect to the nearest neighbor distances compared to the particle densities.

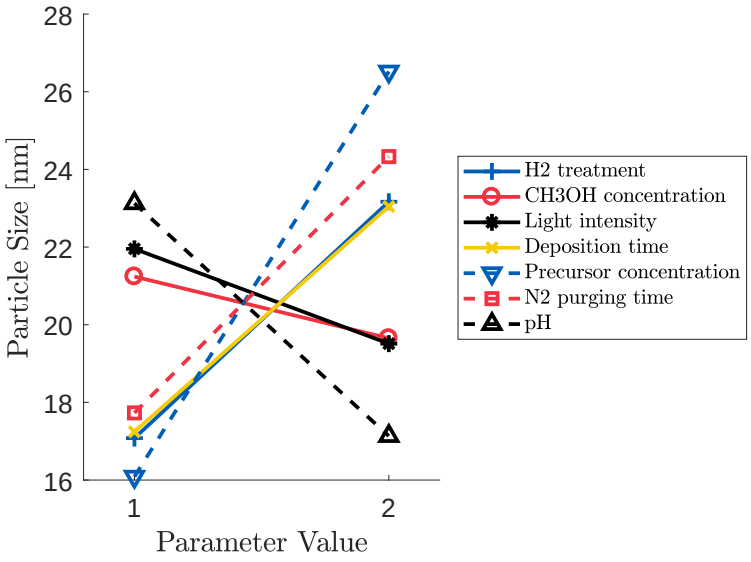

Figure 32: Influence of the variables to the particle size of gold.

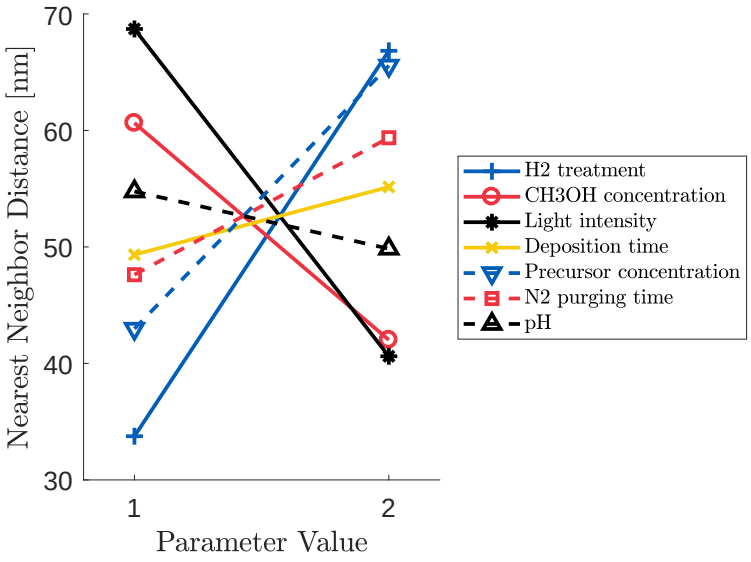

Figure 33: Influence of the variables to the nearest neighbor distance of the gold particles.

In order to achieve a better understanding of the results, the probability that the variables affect the properties (particle density, particle size and nearest neighbor distance) are evaluated. 10000 normally distributed random points were generated based on the average value and the standard deviation of a property, as presented previously in Section 4.2. A histogram is generated based on the slopes between the points, and the sign of the slope is analyzed. A negative sign indicates that changing the parameter value from 1 to 2, the value of the measured property (for example the particle density) decreases. The positive value of slope indicates the opposite. The

histograms for all parameters are found from Appendix A. The confidence intervals of 68% and 95% are indicated with dotted lines, while the average value is given by the solid line.

There are only a few cases in which these confidence intervals are reached. The standard deviations are large in all cases, resulting in widely spread Gaussian distributions and low confidence levels. The large standard deviation results from the small sample set and the interactions of the variables. However, the effect of the variables can be approximated based on the figures presented in Appendix A. The probabilities of the slopes to be negative are obtained by calculating the ratio of the area covered by the negative slopes and dividing it with the total area. Values close to zero indicate that the probability of the slopes to be positive is higher, and values close to one indicate the opposite. The results from this analysis are presented in Table 11. The values from 0 to 0.3 indicate that an increase in the property value is probable when increasing the variable value. The decrease in the property value occurs at a significant probability when the values range from 0.7 to 1.

Based on the analysis, only the solution pH has no effect to the particle density, size or nearest neighbor distance. The rest of the variables affect either to one, two or all of the properties. The H_2 treatment seems to have the highest influence to the particle density and nearest neighbor distances, as Figures 31 and 33 already suggested. H_2 treatment is also likely to increase the particle size. According to the analysis, the most probable method to increase the particle size is to increase the precursor concentration. As the particle size increases, the particle density is likely to decrease and the nearest neighbor distance to increase. This result is in line with the calculated masses of gold, as they remained quite constant even with increasing particle size (Table 5). The particle size can also be increased by increasing the deposition time and N_2 purging time. Particle density, on the other hand, is likely to increase when increasing the intensity of light. According to the analysis, methanol concentration affects mostly to the nearest neighbor distances by decreasing it.

Table 11: The probability of the variables to decrease the value of property in the photodeposition of gold when changed from parameter value 1 to 2.

	Variable						
Property	H_2	CH_3OH	Intensity	Time	Precursor	N_2 time	pH
ρ [μm^{-2}]	0.982	0.400	0.259	0.355	0.768	0.427	0.493
$\bar{d}$ [nm]	0.293	0.547	0.551	0.294	0.194	0.273	0.676
$\bar{r_A}$ [nm]	0.125	0.735	0.788	0.391	0.210	0.327	0.541

According to the presented variable analysis, in order to achieve **small gold particles deposited densely** one should use **low methanol concentration, low precursor concentration, high intensity, short N_2 time and low pH**. The H_2 thermal treatment should not be conducted. The photodeposition of gold seems to be a rapid process, in which the variables need to be optimized so that the nanoparticle growth will not occur too fast. Thus, the use of low precursor concentration,

low methanol concentration, and shorter N_2 purging time are needed, since they will decrease the efficiency of the process and allow more accurate control of the nanoparticle growth.

By solving the effects of individual parameters, the unsuccessful process of sample 1.4 preparation can be analyzed. According to the results, the low particle density on the sample is due to the small light intensity and high pH. The parameters that affect the particle size (high methanol and precursor concentration, and longer N_2 purging time) promote the growth of larger particles. However, the H_2 treatment was not conducted on sample 1.4, and it seemed to have the largest effect on the particle size.

According to the analysis, the parameters leading to low particle density caused the failure of the sample. This observation is in line with the nucleation and growth theory discussed in Chapter 3. The growth of larger particles requires smaller unstable particles to be nucleated at the TiO_2 surface. Resulting from the instability of small nanoparticles, larger particles are formed, which then grow autocatalytically. The parameter set used with sample 1.4 did not provide sufficient environment for particle reduction, so particle growth could not take place.

Sample 1.4 is imaged also with higher magnification in order to search for smaller nanoparticles that are not visible with the 50000x magnification. A magnification of 150000x is used and some nanoparticles with diameters around 5 nm were found in the illuminated area (Figure 34a) but also in the non-illuminated area (Figure 34b). However, the illuminated area also contains some larger gold particles which were also visible in the previous SEM image with the 50000x magnification 28d. These larger particles are most likely formed due to the illumination. The large particle size can be attributed to the parameters used.

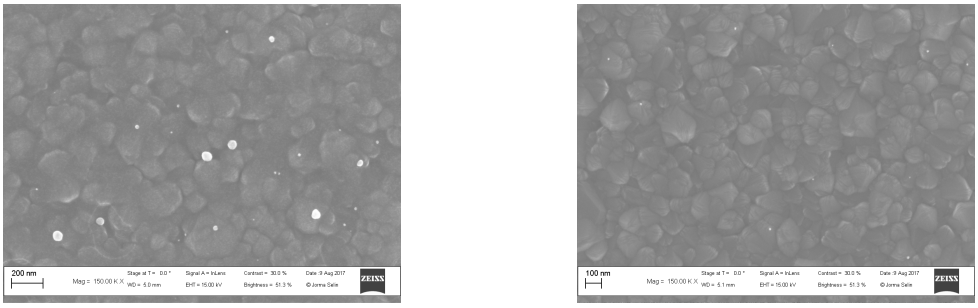

(a) Illuminated. (b) Non-illuminated.

Figure 34: Comparison of illuminated and non-illuminated areas of sample 1.4.

5.4 Photodeposition of platinum

In this section, the analysis of the platinum samples is conducted. Similar to the gold analysis presented in the preceding Section, the analysis is based on SEM images and data obtained from ImageJ image processing. The individual samples are characterized and analyzed first, followed by the discussion of the influence of different variables used in this thesis.

5.4.1 Particle sizes and nearest neighbor distances

The SEM images of the illuminated areas in the photodeposition of platinum for the samples 2.1 – 2.8 are presented in Figure 35a-h, respectively. The sizes of the platinum particles are considerably smaller than the sizes of gold particles, presented previously in Section 5.3.1. The magnification used for the particle size analysis with platinum is 500000x, which is 10 times larger than the one used for the analysis of gold particles. The small particle size also affects the contrast of the SEM images, since the SEM signal originates from a volume rather than the surface, as was explained earlier in Figure 16. The small particle size decreases the amount of secondary electrons that are emitted from the particle. This hinders the particle detection, as the contrast difference becomes small between TiO_2 grain edges and Pt particles.

The influence of process parameters can already be seen from the SEM images. The differences between the samples originate mostly from the particle density, whereas the particle size does not differ significantly. Samples 2.1 and 2.3 (Figures 35a and 35c, respectively) have the highest particle density while sample 2.7 (Figure 35g) has the lowest. Distinguishing individual particles is most difficult on the sample 2.3 due to the high particle density.

Platinum oxide is found on samples 2.1, 2.4, 2.6 and 2.7. The analysis is conducted on the non-oxidized areas since the oxide growth does not allow the detection of individual particles, as seen earlier in Figure 25. In sample 2.4, the oxidized platinum is found evenly spread on the illuminated area. Figure 35d shows a single larger oxide cluster in the analyzed area, which is excluded from the particle size analysis.

The particle size analysis conducted from the SEM images is presented in Figure 36. The log-normal distribution is fitted to the data in red. The fit represents the data fairly well for all of the samples, even though some surplus of small particles is detected. Similar to the gold samples, goodness of fit increases with increasing particle density. The particle size in all of the samples is below 15 nm, and below 10 nm for all the other samples, except the samples 2.3 and 2.4. The average size approximated from the peak of the log-normal fit is around 5 nm for all samples.

The nearest neighbor statistics for the platinum samples are presented in Figure 37. The red curve shows the distribution of completely spatially random particles. The spatially random distribution fits well to the samples with high particle densities (samples 2.1, 2.3, 2.4 and 2.6). With the other samples, the data is not continuous and single columns determine the placement of the fit. However, based on the samples with higher particle densities, the data seems to fit the completely spatially random distribution. The nearest neighbor distances are below 30 nm for these samples. As the particle density decreases, the nearest neighbor distance increases and distances over 100 nm are reached.

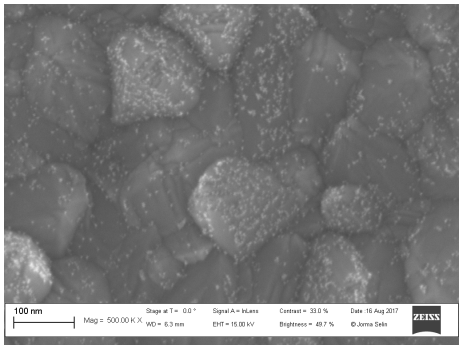

(a) Sample 2.1.

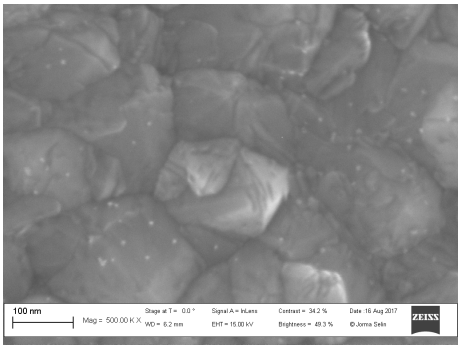

(b) Sample 2.2.

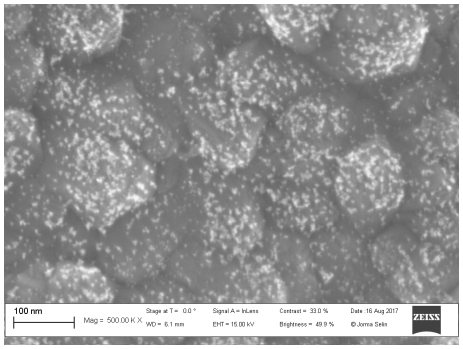

(c) Sample 2.3.

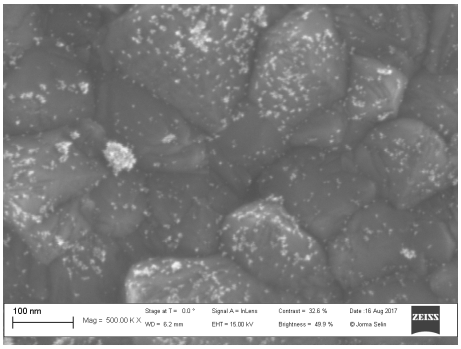

(d) Sample 2.4.

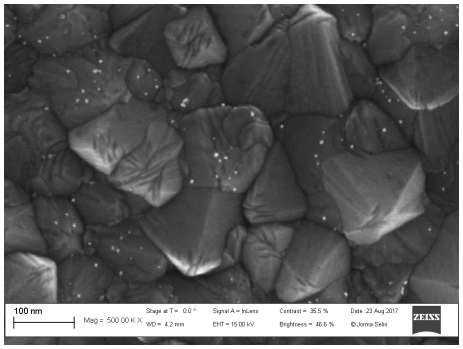

(e) Sample 2.5.

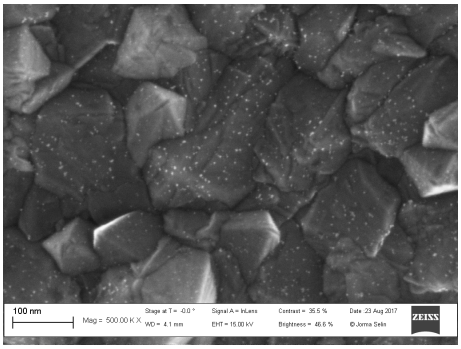

(f) Sample 2.6.

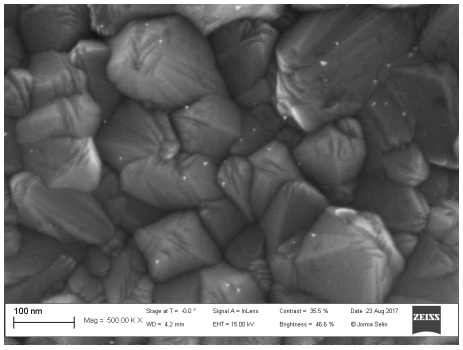

(g) Sample 2.7.

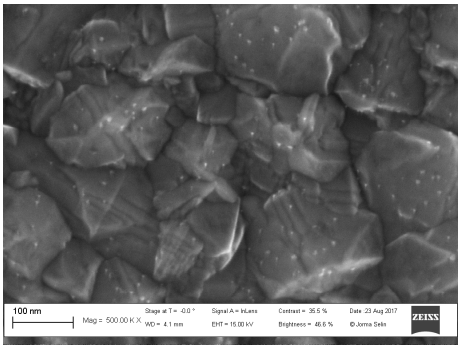

(h) Sample 2.8.

Figure 35: SEM images of the deposited platinum particles.

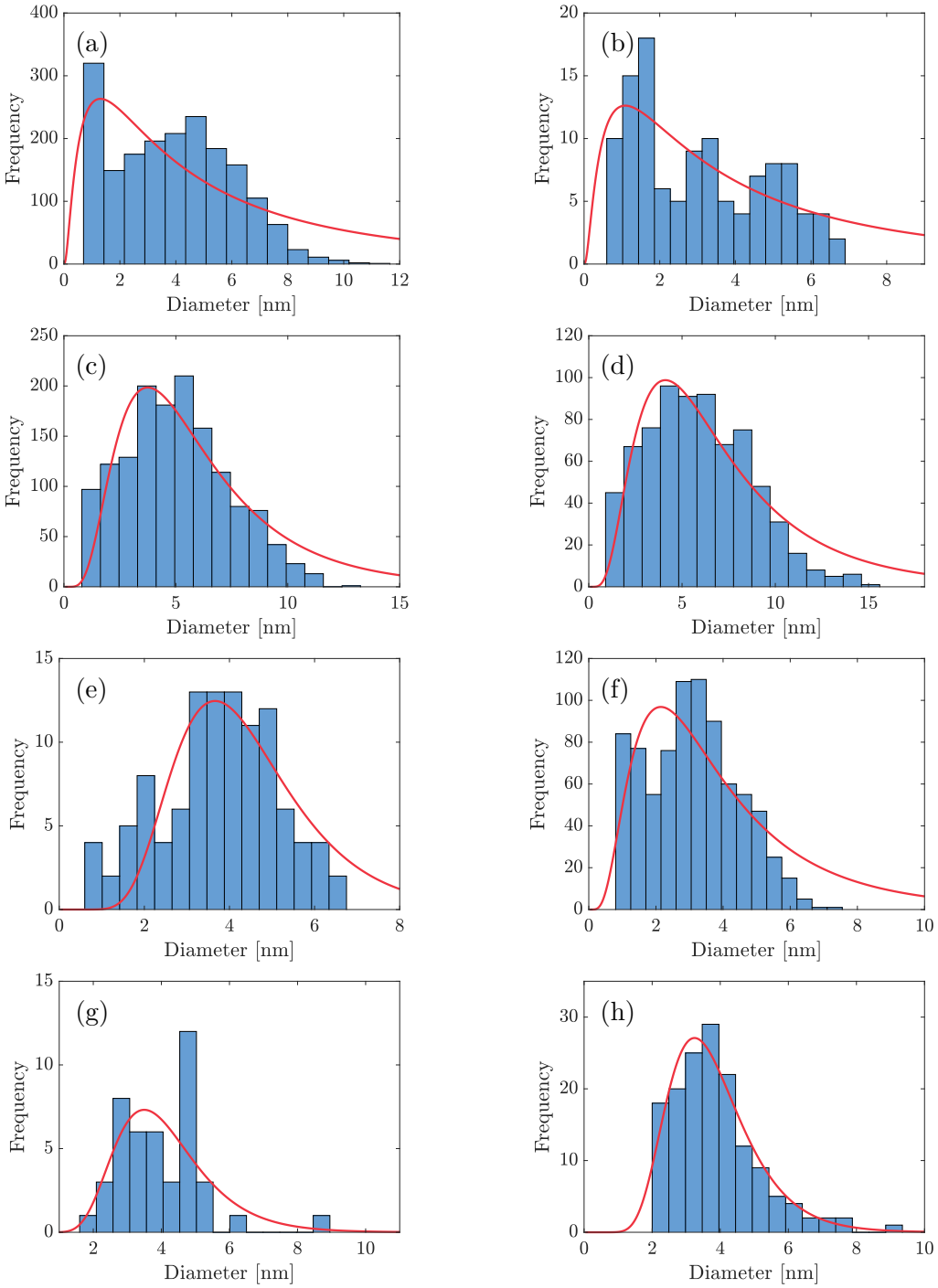

Figure 36: The particle size statistics of the deposited platinum particles on samples 2.1–2.8 ((a)–(h), respectively). The log-normal distribution, seen in red, is fitted to the measured data.

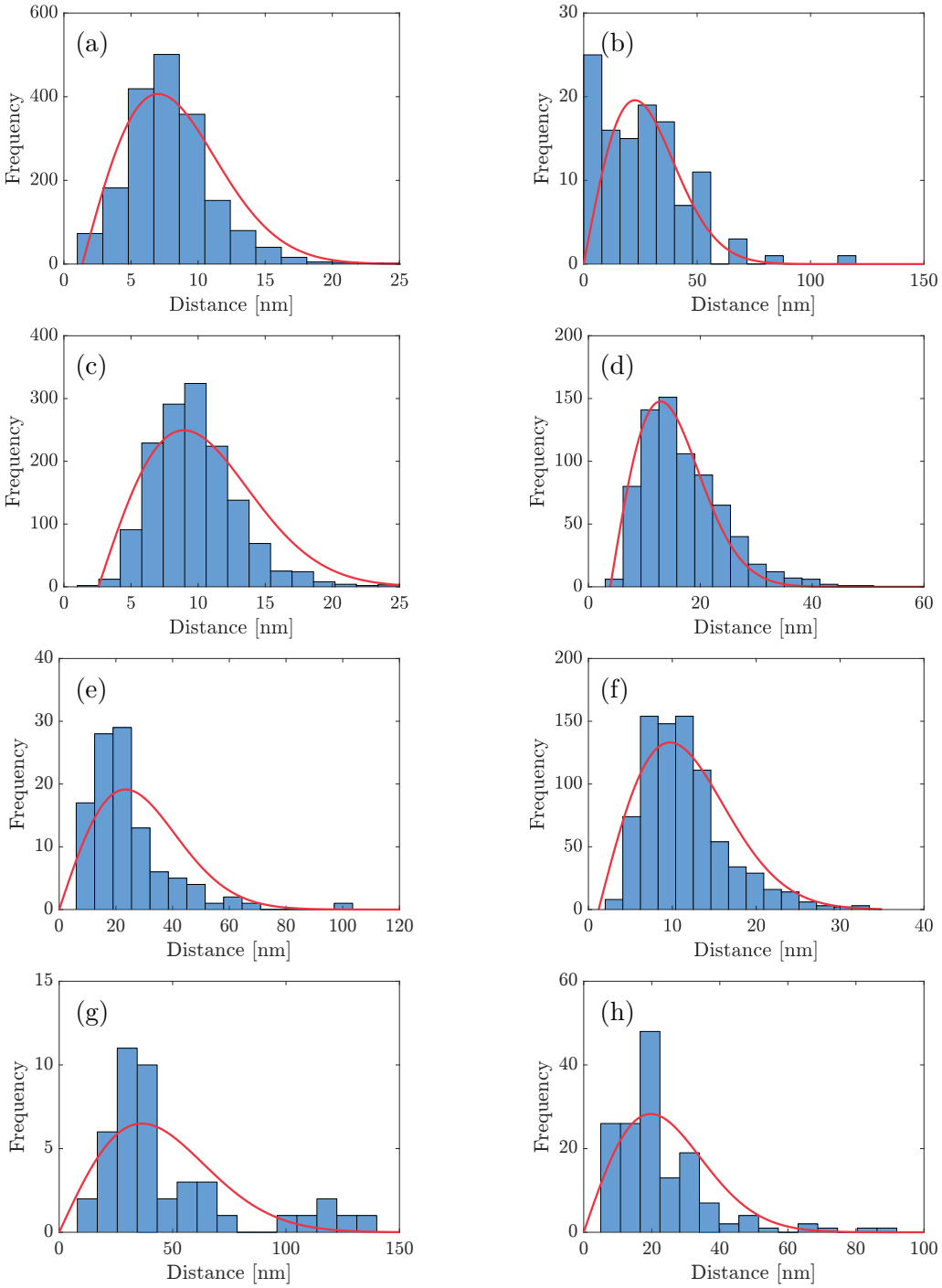

Figure 37: The nearest neighbor distance statistics of the deposited platinum particles on samples 2.1–2.8 ((a)–(h), respectively). The spatially random distribution, seen in red, is fitted to the measured data.

5.4.2 Characteristic values in the photodeposition of platinum

The parameters used in the photodeposition of platinum are collected in Table 12. The results from the particle size (Figure 36) and nearest neighbor distance (Figure 37) analyses are collected in Tables 13 and 14, respectively. The values are calculated from the data obtained from the SEM images.

Table 12: Parameters used for the platinum samples in this thesis.

	Sample							
Parameter	1	2	3	4	5	6	7	8
H_2 treatment	No	No	No	No	Yes	Yes	Yes	Yes
CH_3OH vol-%	5	5	10	10	5	5	10	10
Illumination P [µW]	70	70	35	35	35	35	70	70
Deposition t [min]	120	60	120	60	120	60	120	60
Precursor C [mg/ml]	1	2	1	2	2	1	2	1
N_2 purging t [min]	30	15	15	30	30	15	15	30
pH	7	4	4	7	4	7	7	4

The density (ρ) differences achieved with different photodeposition parameters are significant. Similar to the gold samples, the sample 2.1 had clearly the highest platinum particle density (4992.56 μm^{-2}), whereas the sample 2.7 has the lowest (119.61 μm^{-2}) particle density. The samples can be divided into two groups based on their particle densities. The high density samples (2.1, 2.3, 2.4, and 2.6) have thousands of particles per square micrometer. The low density samples have below 500 particles in the same area. The variables are proven to affect the particle density significantly.

The mean particle diameter ($\bar{d}$) remains fairly constant throughout the samples. The smallest diameter is achieved with sample 2.6 (3.09 nm) and the largest is achieved with sample 2.4 (5.89 nm). Due to the small particle size in the samples, errors originating from the particle size analysis can affect the results significantly. The oxide formation in sample 2.4 could also affect the particle size statistics, since the growth rate of platinum oxide seems to be higher than with metallic particles. However, it is impossible to identify if the individual particles are metallic or metal oxides. Nevertheless, the particle size is small for all of the samples. Contrary to gold, platinum does not show a significant correlation between particle density and size.

The mass of the platinum per area m_A is calculated the same way as m_A for gold. The mass of platinum on a square millimeter is significantly lower compared to gold. This clearly indicates that the platinum reduction occurs through slow mechanisms. The difference in the metal loadings has to occur during particle nucleation and growth phases, since the concentrations of platinum and gold ions are close to equal in the solutions. Thus, the amount of available ions is not the limiting factor for the growth of platinum nanoparticles. The highest loading of platinum is achieved with sample 2.3 (4.76 ng/mm^2) and the lowest is achieved with sample 2.7 (0.06 ng/mm^2).

Samples 2.3 and 2.4 have the highest loadings due to large particle sizes and high particle densities.

Similar to the gold particles, the median of the particle diameter (M) is slightly smaller than the mean particle diameter. This indicates that the particle size distribution is slightly skewed, following the log-normal distribution. Standard deviations (σ) of the mean particle diameter are between 1 nm and 3 nm for the platinum samples. The σ values are around 50% of the average diameter.

The log-normal distribution is worse representation of the data for the platinum samples that the gold samples, as indicated by the low R^2 values. This occurs partly due to the small sizes of platinum particles, as it increases the error during the image analysis. Similar to the gold samples, the R^2 increases with increasing particle density. However, the sample with a lowest particle density (sample 2.8) has the highest R^2 value. However, the shape of the distribution closely resembles the log-normal distribution.

Table 13: Comparison of the particle size statistics of the platinum deposition.

Sample	ρ [μm^{-2}]	$\bar{d}$ [nm]	m_A [ng/mm^2]	M [nm]	σ^2 [nm^2]	σ [nm]	R^2
2.1	4992.89	3.92	3.20	3.86	4.39	2.10	0.671
2.2	312.74	3.10	0.10	2.85	2.95	1.72	0.500
2.3	3932.31	5.03	4.76	4.94	5.59	2.36	0.833
2.4	1971.59	5.89	3.92	5.64	7.93	2.82	0.871
2.5	290.98	3.75	0.12	3.86	1.84	1.36	0.592
2.6	2202.75	3.09	0.58	3.08	1.82	1.35	0.681
2.7	119.66	3.97	0.06	3.86	1.63	1.28	0.567
2.8	410.64	3.88	0.18	3.68	1.58	1.26	0.956

The nearest neighbor distance statistics of the platinum samples are presented in Table 18. The average nearest neighbor distance ($\bar{r_A}$) is found to increase with decreasing particle density (ρ), as expected. The medians of the nearest neighbor distances (M) are smaller than the average distance, as the completely spatially random distribution suggests. The standard deviations (σ) are large for the samples with smaller particle density. For example, the sample 2.7 has a standard deviation of 32.21 nm, which is around two thirds of the value of the average distance (47.63 nm). This indicates that the data is spread on large range. The R^2 values of the samples are below 0.9 for all of the samples except for the samples 2.1 and 2.4. This indicates that the completely spatially random distributions do not describe the data perfectly. However, the R^2 is closer to 1 on the samples with high particle densities, so with increasing density the particles starts to resemble the random distribution.

A Clark-Evans test is conducted based on the nearest neighbor data, as described previously in Section 4.3.3. The results of the Clark-Evans test are collected to Table 15. The R_{CE} values are similar to the gold samples, as the values are over 1 for the high particle density samples and under 1 for the low density samples. However, sample 2.7 has the lowest particle density but the R_{CE} value is slightly over 1. These results indicate similar behavior for the platinum and the gold particles. The

Table 14: Comparison of the nearest neighbor distance statistics of platinum particles.

Sample	ρ [μm^{-2}]	$\bar{r_A}$ [nm]	M [nm]	σ^2 [nm^2]	σ [nm]	R^2
2.1	4992.56	7.90	7.62	10.08	3.17	0.915
2.2	312.71	26.01	25.01	396.48	19.91	0.396
2.3	3932.04	9.77	9.46	9.60	3.10	0.858
2.4	1971.46	16.97	15.41	51.25	7.16	0.976
2.5	290.96	23.91	20.23	218.55	14.78	0.585
2.6	2202.60	11.46	10.72	24.31	4.93	0.873
2.7	119.65	47.63	35.17	1037.56	32.21	0.499
2.8	410.61	22.58	18.97	198.88	14.10	0.638

increasing value of R_{CE} with increasing particle density indicates that particle size focusing effects (for example, Ostwald ripening) take place and cause the dissolution of small nanoparticles in order to initiate the growth of larg particles. However, the particle sizes remain quite constant with all samples. This indicates that the Ostwald ripening might not have a significant influence on the particle distribution. The more likely explanation is that the oxygen vacancies are depleted from the areas between the nanoparticles, stabilizing particles to certain locations. The standard error σ_{rE} is small and has minimal influence to the value of R_{CE}.

Table 15: Clark-Evans test statistics of the deposition of platinum particles.

Sample	ρ [μm^{-2}]	$\bar{r_A}$ [nm]	$\bar{r_E}$ [nm]	R_{CE}	σ_{rE} [nm]
2.1	4992.56	7.90	7.08	1.12	0.09
2.2	312.71	26.01	28.27	0.92	1.38
2.3	3932.04	9.77	7.97	1.23	0.11
2.4	1971.46	16.97	11.26	1.51	0.22
2.5	290.96	23.91	29.31	0.82	1.48
2.6	2202.60	11.46	10.65	1.08	0.20
2.7	119.65	47.63	45.71	1.04	3.60
2.8	410.61	22.58	24.67	0.92	1.05

5.4.3 Comparison of photodeposition parameters

To analyze the influence of single parameters, the samples are ordered based on their particle density (Table 16), particle size (Table 17), and nearest neighbor distances (Table 18), as presented previously in Section 4.2. Each of the parameters has two values, one being the smaller value and 2 being the larger. For H_2 thermal treatment, the value 1 refers to the non-treated samples, and value 2 to the H_2 treated samples. Similar to the gold samples, a variable affects the photodeposition if the parameter values are distributed unevenly, meaning that at least three out of four of a single parameter are located in the top half of the tables.

Table 16 presents the samples arranged from the highest particle density to the lowest. There are four parameters that affect the particle density: H_2 thermal treatment, light intensity, precursor concentration and solution pH. H_2 treatment decreased the particle density, which could already evident from the SEM images presented earlier. The UV-light intensity also affects the particle density. With increasing light intensity, the particle density decreases. Previous study suggest the opposite, *i.e.*, higher intensity increases the deposition rate because of increased photon flux [125]. However, it is stated in the same study, that the photodeposition rate will decrease over time, since the precursor concentration changes as the platinum ions are reduced to the semiconductor surface. The deposition times used in this study could be long enough to diminish the effect of the increased light intensity to the particle density. The higher intensity could have reduced the platinum particles faster, so that particle size focusing effects could have had more time to occur, decreasing the amount of small unstable nanoparticles.

The precursor concentration is the third variable that affects the particle density in the photodeposition of platinum. The increased precursor concentration seems to decrease the particle density. As previous studies suggest, the photodeposition rate of platinum is not determined by the precursor concentration [125]. The concentration of 1 mg/ml is high enough to sufficiently provide the ions for the reactions, so the increase in the concentration will not increase the reaction rate. The higher particle density due to the lower precursor concentration can be a result from decreased interactions between the platinum ions which could lead to increased adsorption to the TiO_2 surface. Another possibility is that particle nucleation occurs faster with high precursor concentration. The faster nucleation allows the size focusing effects to dissolve small and unstable particles and form large particles, decreasing the particle density.

The pH of the solution is the final variable affecting the particle density. The photodeposition in neutral pH resulted in higher particle density. The result is surprising, since acidic pH should cause a positive charge to the surface, attracting the negative platinum complexes and increasing the particle density [121]. However, the contrary result could occur due to the oxide formation. As seen in the images of the oxide formation show earlier (Figure 25), the platinum oxide forms a dense and uniform layer on the TiO_2 surface. The particles seen in the SEM images for the pH 7 samples could be an earlier stage of similar oxide growth resulting in a high density of separate particles.

In Table 17, the samples are arranged from the smallest average particle diameter to the highest. Once again, four variables can be detected to affect the particle size: H_2 treatment, the sacrificial methanol concentration, the deposition time and the pH.

The increase of sacrificial agent concentration increases the size of the platinum particles. The sacrificial agents seem to participate in the reaction, allowing more platinum ions to reduce to the TiO_2 surface. The methanol molecules provide electrons to the reduction reaction once the molecules form radicals due to the UV-illumination [131]. The longer deposition time also increases the particle size which is inline with previous studies [126]. As shown earlier in the Figure 13, the particle size

Table 16: Influences of variables to the platinum particle densities.

		Variable						
Sample	ρ [μm^{-2}]	H_2	CH_3OH	Intensity	Time	Precursor	N_2 time	pH
2.1	4992.56	1	1	2	2	1	2	2
2.3	3932.04	1	2	1	2	1	1	1
2.6	2202.6	2	1	1	1	1	1	2
2.4	1971.46	1	2	1	1	2	2	2
2.8	410.61	2	2	2	1	1	2	1
2.2	312.71	1	1	2	1	2	1	1
2.5	290.96	2	1	1	2	2	2	1
2.7	119.65	2	2	2	2	2	1	2

was expected to increase from 3.9 nm to 4.4 nm when the deposition time increased from 60 min to 120 min. The increase in particle size with increasing deposition time can be explained with the larger amount of electron-hole pair generated in TiO_2. The results in this study support the results from previous reports.

The pH is found to affect the particle size as well. Neutral pH results in a higher particle size. Previous articles suggest, that platinum particles should be adsorbed onto the TiO_2 surface at acidic pH, because the surface is positively charged and attracts the negative platinum complexes [121]. On the other hand, the results from this study are similar to the result presented by Qamar and Ganguli [124], who discovered that platinum agglomeration can also occur in the neutral pH range of 5–9. The other explanation is the oxide formation which occurs at pH 7. The oxide formation seems to occur at higher rate than the metallic particles, based on the SEM images of the oxidized areas. The particles seen in the analyzed area could be platinum oxide particles on earlier stage of the oxide formation, causing the high density and large particle size.

The H_2 treatment actually appears to decrease the particle size. Based on the results obtained from gold deposition, the H_2 treatment was expected to have a contrary effect. The most probable reason for these results is that the affect of H_2 treatment to the particle size is actually small, and that the other parameters (methanol concentration, deposition time and pH) have a larger effect on the variation in particle size. The different variable combinations causes the H_2 treated samples are arranged in such order.

Table 18 shows the samples arranged from the shortest nearest neighbor distance to the longest. The table is almost identical to the table of particle densities (Table 16) with the exception of samples 2.5 and 2.2 have changed their position. This does not affect the results of the analysis, as the same four parameters which affect the density, affect the nearest neighbor distance (H_2 treatment, light intensity, precursor concentration and pH). This is expected based on the Clark-Evans test (Table 15), as the particle distributions are similar for the samples with similar particle densities. The positions of samples 2.5 and 2.2 are altered due to their almost equal particle

Table 17: Influences of variables to the platinum particle sizes.

		Variable						
Sample	$\bar{d}$ [nm]	H_2	CH_3OH	Intensity	Time	Precursor	N_2 time	pH
2.6	3.09	2	1	1	1	1	1	2
2.2	3.1	1	1	2	1	2	1	1
2.5	3.75	2	1	1	2	2	2	1
2.8	3.88	2	2	2	1	1	2	1
2.1	3.92	1	1	2	2	1	2	2
2.7	3.97	2	2	2	2	2	1	2
2.3	5.03	1	2	1	2	1	1	1
2.4	5.89	1	2	1	1	2	2	2

densities, so even small variations in the similar particle distributions can result in a change of order.

Table 18: Influences of variables on the nearest neighbor distances of platinum particles.

		Variable						
Sample	$\bar{r_A}$ [nm]	H_2	CH_3OH	Intensity	Time	Precursor	N_2 time	pH
2.1	7.90	1	1	2	2	1	2	2
2.3	9.77	1	2	1	2	1	1	1
2.6	11.46	2	1	1	1	1	1	2
2.4	16.97	1	2	1	1	2	2	2
2.8	22.58	2	2	2	1	1	2	1
2.5	23.91	2	1	1	2	2	2	1
2.2	26.01	1	1	2	1	2	1	1
2.7	47.63	2	2	2	2	2	1	2

The magnitude of the influence caused by different parameters are evaluated in Figures 38–40, which show the average particle densities, sizes, and nearest neighbor distances for parameter values 1 and 2 for all of the variables. The effects of variables to the particle density are compared in Figure 38. The most profound influence is achieved by conducting a H_2 heat treatment and by changing the precursor concentration. Both of them change the particle density from around 2800 μm^{-2} to around 800 μm^{-2}. The effect of pH seems to be similar to the effect of deposition time, even though deposition time was not detected to be a meaningful parameter in the previous analysis. The effect of light intensity is small according to the figure. However, the average values of the particle densities are balanced by the highest density which is achieved with the higher intensity, opposite to the overall trend.

Figure 39 compares the influences of different variables on the particle size. The changes in particle size overall are small for the platinum samples. The largest

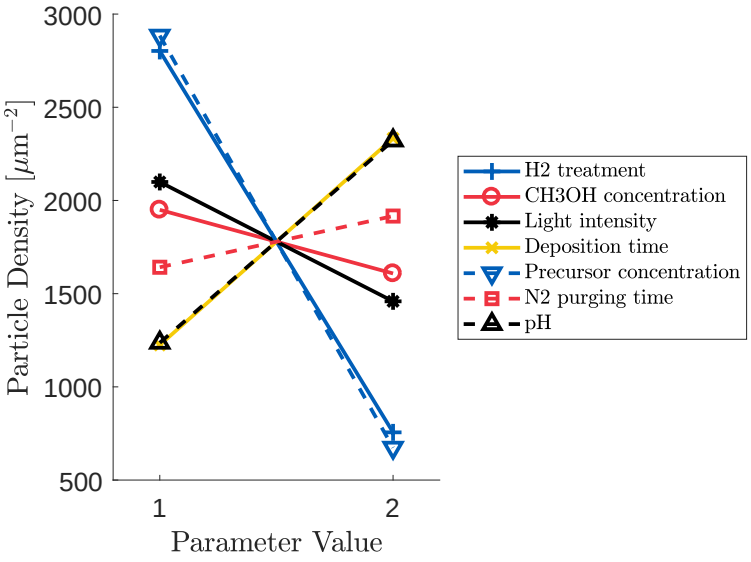

Figure 38: Influence of the variables to the particle density of platinum.

difference is observed with the increased methanol concentration which increases the average particle diameter from 3.45 nm to 4.75 nm. All the other parameters account for changes less than 1 nm. For example, the second and third largest changes are observed by applying H_2 treatment and adjusting pH. The total change in particle diameter is only around 0.8 nm for both of these variables.

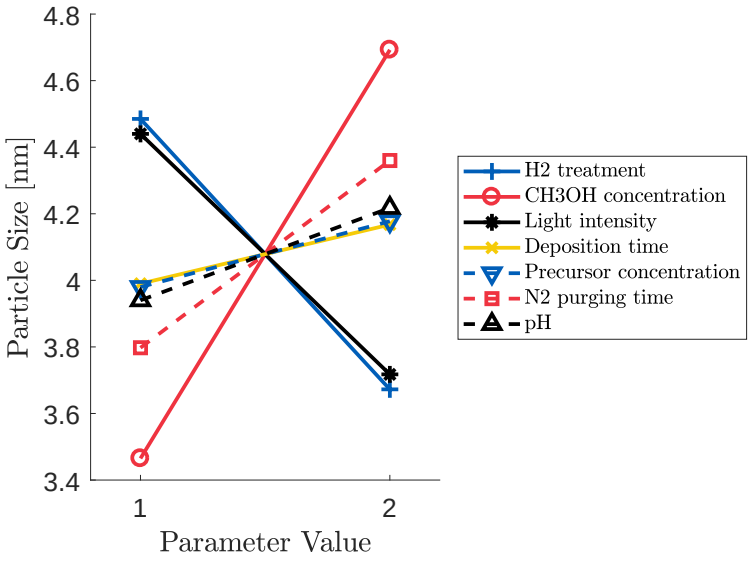

Figure 39: Influence of the variables to the particle size of platinum.

The average nearest neighbor distances for all of the variables are compared in Figure 40. The lines are in opposite order compared to the particle density graph (Figure 38). However, the precursor concentration seems to have larger effect on the nearest neighbor distance than the H_2 treatment, even though their influence is

identical to the particle density. The changes are once again small, below 15 nm, for all of the other variables.

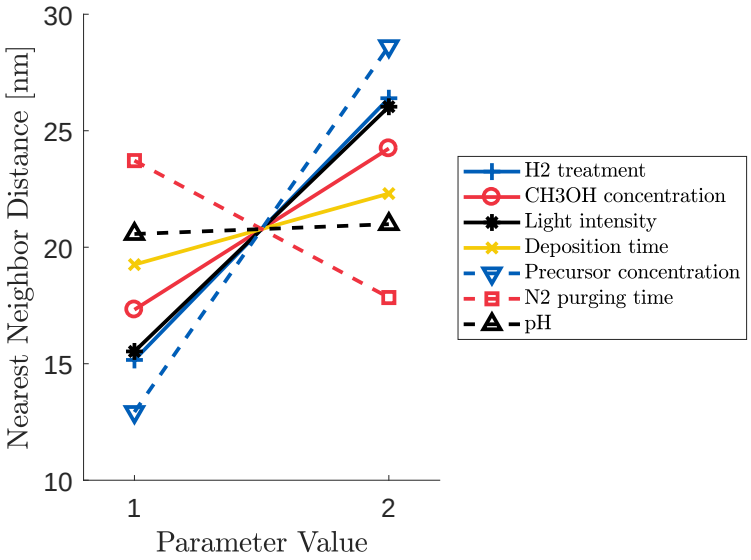

Figure 40: Influence of the variables to the nearest neighbor distance of the platinum particles.

Similar probability analysis is conducted for the platinum samples as was previously done for the gold samples in Section 5.3.3. Figures B1–B7 (Appendix B) present the slopes of the 10000 randomly generated points based on the average and standard deviations values measured from the platinum samples. The samples are arranged according to the process parameters and the distributions are calculated for both parameter values. Variables with values between 0 and 0.3 have a 70% probability to increase the property value when the value of variable increases (or when H_2 treatment is conducted). Values 0.7 to 1 indicate a decrease in the property value with the increasing value of variable.

Based on the analysis, three variables have no effect to the particle density, particle size or nearest neighbor distance: the deposition time, N_2 purging time and solution pH. The particle density and nearest neighbor distance are the most likely to be affected by precursor concentration and H_2 treatment. An increase in the precursor concentration will decrease the particle density and increase the nearest neighbor distance, as was stated previously in this Section. Conducting a H_2 thermal treatment has similar effects. The nearest neighbor distance can also be increased by increasing the intensity of light.

As was stated in Section 5.4.1, the particle size of platinum nanoparticles seems to stay approximately constant regardless of variable changes. According to the analysis, the only variable that is likely to influence the particle size is methanol concentration. Increasing CH_3OH concentration increases the size of deposited platinum particles. Methanol participates in the reduction of the metal by forming a radical and donating excess electrons to the reduction reaction (Equation (16)) [89]. The excess electrons allow faster growth of the platinum particle.

Table 19: The probability of the variables to decrease the value of property in the photodeposition of platinum when changed from parameter value 1 to 2.

	Variable						
Property	H_2	CH_3OH	Intensity	Time	Precursor	N_2 time	pH
ρ [μm^{-2}]	0.846	0.535	0.600	0.303	0.873	0.437	0.316
$\bar{d}$ [nm]	0.616	0.282	0.620	0.438	0.444	0.401	0.447
$\bar{r_A}$ [nm]	0.260	0.363	0.268	0.434	0.248	0.589	0.455

Based on the particle analysis, to achieve **small and densely packed metallic** platinum nanoparticles, one should have **low light intensity, low sacrificial agent content, low precursor concentration and acidic pH**. The acidic pH should be selected in all cases, in order to achieve metallic nanoparticles. The metallic nanoparticles have shown to be more photocatalytically active than platinum oxides [151]. The H_2 thermal treatment should not be conducted for the sample, since it was shown to decrease the particle density more drastically than particle size. Platinum particle sizes are small for all of the samples, independent of the parameters used in this thesis. This is a promising result, as the small particle size has been proven to have a profound effect on the photocatalytic activity [29].

5.5 Comparison of the photodeposition of gold and platinum

This Section summarizes the similarities and differences in the photodeposition of gold and platinum. The observations are discussed and explained. Finally, the possible consequences of the results to the photoactivity are speculated.

The photodeposition of gold and platinum resulted in overall to similar results. The distributions of the particle densities, sizes, and nearest neighbor distances are similar for both materials. With both platinum and gold samples, the measured particle sizes and the nearest neighbor distances are well described by the fitted distributions, especially in the case of high particle density samples. The Clark-Evans test also resulted in similar results for both noble materials. For higher particle densities, the value of R_{CE} is over 1, indicating that the particles have slightly larger nearest neighbor distances than in the case of complete spatial randomness. This is explained with the depletion of oxide vacancies in the substrate around the nanoparticles. The oxide vacancies are diffused from the depleted areas in order to stabilize the growing nanoparticle, causing the formation of vacancy clusters in which the metal particle is reduced. Without the oxide vacancies, the reduced metal is not in a stable form as a solid particle on TiO_2 surface.

There are three distinct differences observed for the photodeposition of gold and platinum. First, the deposition time is significantly longer for the photodeposition of platinum. In this study, the used deposition times for gold were 15 min and 30 min, whereas the deposition times for platinum were 60 min and 120 min. The platinum

deposition time was increased to achieve a distinct difference between the samples. The needed deposition times depend on the kinetics of the nucleation and growth phases. Because the mechanisms are different for gold and platinum nanoparticles, the reactions occur at different rates. Even though both of the materials experience autocatalytic growth, the initial nucleation of gold has been proven to be faster and occurs in a burst-like manner [117]. The faster nucleation allows the deposition times to be significantly shorter.

The second distinct difference between the photodeposition of gold and platinum is the deposited particle size. Platinum photodeposition is found to result in significantly smaller nanoparticles compared to the photodeposited gold particles. The diameters of the platinum nanoparticles were less than 15 nm for all of the samples whereas the diameter of the deposited gold particles were less than 50 nm (except for the sample 1.5). This observation is in line with previously published articles, where similar process parameters yielded platinum particles with diameter range from 3–6 nm whereas the diameters of gold particles are between 10 nm and 100 nm [29]. This difference in particle sizes arose from different nucleation and growth mechanisms, *i.e.*, for the same reasons presented previously in Section 3.1.

Particle growth due to parameter changes was observed in the case of the photodeposition of gold, whereas the particle sizes of platinum remained fairly constant throughout the samples. However, particle densities were affected by the studied process parameters in both cases. Due to their small sizes, the masses of the platinum particles were significantly lower than the masses of gold particles. This further indicates the differences in the nucleation and growth kinetics, since the precursor masses in the solutions were approximately identical, implying that the growth is at least not limited by the amount of available ions for the reduction.

The third difference observed between the photodeposition of gold and platinum is the form of the deposited material. In the case of the photodeposition of gold, all of the gold particles are deposited as metallic particles, and there are no distinct differences in the external appearance of the photodeposited gold particles. However, the platinum particles were found to be in oxidized form if the photodeposition was conducted in neutral pH. Gold does not form oxides easily as it is considered to be most stable and non-reactive metal [152]. Platinum, on the other hand, is a relatively reactive noble metal, which also partly explains its higher catalytic activity.

Based on these differences, the photocatalytic efficiency of the photodeposited materials can be evaluated. Platinum has been proven to be the more photocatalytically active than gold due to its high electron trapping efficiency and low work function [16, 29]. The photodeposited Pt nanoparticles are also smaller than gold particles which is beneficial for photocatalytic applications. As discussed previously in Section 3.1, large cocatalyst particles shadow the active sites on the surface of a photocatalyst and increase the possibility of the metal cocatalysts to act as a recombination centers [29]. Because of their slow growth during photodeposition, the sizes of platinum particles are (presumably) easier to control than the sizes of gold particles. The efficiency of platinum as a cocatalyst is hindered by oxide formation. However, the results demonstrate that the oxide formation can be avoided efficiently by adjusting pH.

Photodeposition allows the control of particle density by changing the deposition parameters, as the results have shown. This allows the optimization of the cocatalyst loading on the photocatalytic material. The loading amount has been proven to have similar effects on photocatalytic activity as particle size [97]. On the other hand, if the loading is too small, the photogenerated carriers will recombine before the electron trapping can occur. Finding the optimal cocatalyst loading will require further studies, but photodeposition has proven to be an excellent method for controlling the density of gold and platinum nanoparticles.

The distribution of the nanoparticles reduced by photodeposition could also be beneficial considering the electron trapping. The Clark-Evans test conducted in this thesis showed that the distribution of the particles is not perfectly random. Instead, the particles on average are distributed slightly further away from each other compared to the case of complete randomness. This can enable more efficient charge trapping, as the metal nanoparticles are distributed more evenly across the surface (Figure 41). This evens the carrier diffusion lengths for the photogenerated charge carriers, compared to a clustered growth in which the distances between the charge trapping clusters are large. The area that is left between the clusters will be ineffective for photocatalysis as the photogenerated charge carriers recombine before reaching the clustered electron traps.

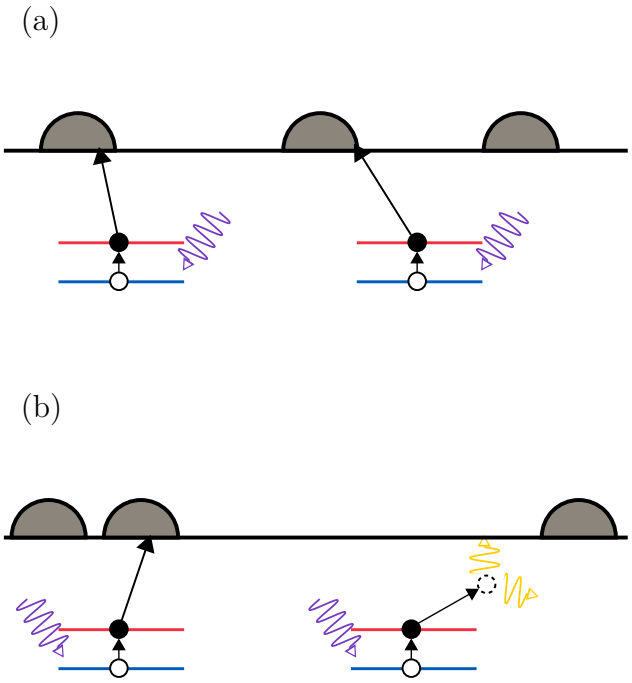

Figure 41: A schematic figure of charge trapping by cocatalyst in the case of (a) evenly distributed particles, and (b) clustered particles. In (a), the photogenerated electrons are efficiently trapped by the cocatalysts. In (b), the diffusion length increases for the charge carriers generated between the clusters, leading to recombination before the electron is trapped and heat is released.

6 Conclusions

In this thesis, photodeposition of gold and platinum nanoparticles was conducted on ALD-grown titanium dioxide layer. The aim was to understand the effect of process parameters on the particle densities, sizes, and nearest neighbor distances of noble metal nanoparticles. The number of samples was minimized using the Taguchi approach. The samples were characterized with scanning electron microscope, followed by image analysis. The influences of different variables were analyzed, and the reasoning behind the observed behaviour was presented.

Gold and platinum were both successfully photodeposited on TiO_2-coated samples. Photodeposition was determined to require a TiO_2 layer with a thickness over 50 nm. The selected photodeposition parameters have a significant effect on the particle densities and the nearest neighbor distances. The platinum particle densities varied from 120 μm^{-2} to 4993 μm^{-2}, whereas the particle densities for gold ranged from 28.7 μm^{-2} to 440.1 μm^{-2}. For all samples, the nearest neighbor distances decreased with increasing particle density and vice versa. The most influential variables for changing particle densities and nearest neighbor distances are H_2 thermal treatment and the precursor concentration. Conducting the H_2 treatment and increasing the precursor concentration decrease the particle densities and increase the nearest neighbor distances of both platinum and gold nanoparticles.

The nearest neighbor distances were found to be slightly larger compared to a completely randomly distributed particles. This behavior was attributed to the depletion of oxygen vacancies between the reduced metal particles. Oxygen vacancies are active sites for metal reduction reactions, and without them the metal nucleation is unlikely.

The influence of photodeposition parameters to the deposited particle sizes is significantly different for the gold and platinum particles. For the gold particles, the process parameters influenced the particle size more drastically. The average diameters of gold nanoparticles ranged from 12 mm to 37 nm. The most influential variable considering the gold particle size was determined to be the precursor concentration. The platinum particle size variations were found to be almost insignificant. The average diameters of the platinum particles were between 3 nm and 6 nm. The differences in the sizes of gold and platinum particles occur due to different nucleation processes. The nucleation of gold occurs in a burst-like process which enables a faster transfer to the stage of autocatalytic growth.

The solution pH is an important variable especially in the photodeposition of platinum. The oxidation number of the platinum nanoparticles was found to depend on the solution pH. In pH 4, the platinum particles are metallic. When the pH is increased to neutral, the formation of platinum oxide occurs in addition to the reduction of metallic platinum. In contrast, gold particles were deposited in metallic form in neutral and acidic pH.

The results obtained in this thesis allow the extrapolation of the data for further studies. Furthermore, increasing the amount of samples in following studies would allow a more complete understanding of the interactions between different variables. Using a larger number of samples would also allow adding more variables,

such as the influence of different organic donors or precursors. For photocatalytic applications, photoacitivity measurements should be conducted in order to optimize the photodeposition parameters for the best result. In addition, for future work the possibilities of photodeposition in other applications, such as plasmonic nanoparticle fabrication, should be considered.

The results obtained in this study clearly indicate that photodeposition can be conducted on an ALD-grown TiO_2 layer in a controlled manner in order to yield desired particle densities and particle sizes. The results suggest that photodeposition is an effective method for cocatalyst deposition. The effectiveness of cocatalysts in photocatalytic reactions is largely based on the particle size and the particle density, which are purely determined by the used process parameters. Small particle size has been shown to be beneficial in cocatalysts, and for effective cocatalysts the size should be below 10 nm [60]. For the photodeposition of platinum, the particle size remained below 6 nm throughout the samples. Platinum in itself, is also known to be one of the most efficient cocatalyst [91]. By using photodeposited platinum particles as cocatalysts, the efficiency of photocatalytic reactions could be increased. As photodeposition enables accurate control of particle size and density, it is one of the most promising cocatalyst deposition methods in the future. For example, if coupled with a photoelectrochemical cell, photodeposition of cocatalysts could revolutionize the H_2 production, and encourage the wider implementation of technologies utilizing hydrogen fuel.

References

1. A. Kudo and Y. Miseki, "Heterogeneous photocatalyst materials for water splitting," *Chemical Society Reviews*, vol. 38, no. 1, pp. 253–278, 2009.

2. S. C. Roy, O. K. Varghese, M. Paulose, and C. A. Grimes, "Toward solar fuels: photocatalytic conversion of carbon dioxide to hydrocarbons," *Acs Nano*, vol. 4, no. 3, pp. 1259–1278, 2010.

3. K. Maeda, "Photocatalytic water splitting using semiconductor particles: history and recent developments," *Journal of Photochemistry and Photobiology C: Photochemistry Reviews*, vol. 12, no. 4, pp. 237–268, 2011.

4. K. Maeda and K. Domen, "Photocatalytic water splitting: recent progress and future challenges," *The Journal of Physical Chemistry Letters*, vol. 1, no. 18, pp. 2655–2661, 2010.

5. S.-Y. Lee and S.-J. Park, "TiO_2 photocatalyst for water treatment applications," *Journal of Industrial and Engineering Chemistry*, vol. 19, no. 6, pp. 1761–1769, 2013.

6. A. Di Paola, E. García-López, G. Marcì, and L. Palmisano, "A survey of photocatalytic materials for environmental remediation," *Journal of hazardous materials*, vol. 211, pp. 3–29, 2012.

7. J.-M. Herrmann, "Heterogeneous photocatalysis: fundamentals and applications to the removal of various types of aqueous pollutants," *Catalysis today*, vol. 53, no. 1, pp. 115–129, 1999.

8. M. D. Hernández-Alonso, R. Portela, and J. M. Coronado, "Turning sunlight into fuels: Photocatalysis for energy," in *Design of Advanced Photocatalytic Materials for Energy and Environmental Applications*, pp. 67–84, Springer, 2013.

9. A. L. Linsebigler, G. Lu, J. T. Yates, *et al.*, "Photocatalysis on TiO_2 surfaces: principles, mechanisms, and selected results," *Chemical reviews*, vol. 95, no. 3, pp. 735–758, 1995.

10. W. Niu, X. Li, S. K. Karuturi, D. W. Fam, H. Fan, S. Shrestha, L. H. Wong, and A. I. Y. Tok, "Applications of atomic layer deposition in solar cells," *Nanotechnology*, vol. 26, no. 6, p. 064001, 2015.

11. A. Paracchino, V. Laporte, K. Sivula, M. Grätzel, and E. Thimsen, "Highly active oxide photocathode for photoelectrochemical water reduction," *Nature materials*, vol. 10, no. 6, pp. 456–461, 2011.

12. Y. W. Chen, J. D. Prange, S. Dühnen, Y. Park, M. Gunji, C. E. Chidsey, and P. C. McIntyre, "Atomic layer-deposited tunnel oxide stabilizes silicon photoanodes for water oxidation," *Nature materials*, vol. 10, no. 7, pp. 539–544, 2011.

13. M. H. Lee, K. Takei, J. Zhang, R. Kapadia, M. Zheng, Y.-Z. Chen, J. Nah, T. S. Matthews, Y.-L. Chueh, J. W. Ager, *et al.*, "p-type InP nanopillar photocathodes for efficient solar-driven hydrogen production," *Angewandte Chemie International Edition*, vol. 51, no. 43, pp. 10760–10764, 2012.

14. S. Hu, M. R. Shaner, J. A. Beardslee, M. Lichterman, B. S. Brunschwig, and N. S. Lewis, "Amorphous TiO_2 coatings stabilize Si, GaAs, and GaP photoanodes for efficient water oxidation," *Science*, vol. 344, no. 6187, pp. 1005–1009, 2014.

15. A. K. Vannucci, L. Alibabaei, M. D. Losego, J. J. Concepcion, B. Kalanyan, G. N. Parsons, and T. J. Meyer, "Crossing the divide between homogeneous and heterogeneous catalysis in water oxidation," *Proceedings of the National Academy of Sciences*, vol. 110, no. 52, pp. 20918–20922, 2013.

16. J. Ran, J. Zhang, J. Yu, M. Jaroniec, and S. Z. Qiao, "Earth-abundant cocatalysts for semiconductor-based photocatalytic water splitting," *Chemical Society Reviews*, vol. 43, no. 22, pp. 7787–7812, 2014.

17. J.-G. Kang and Y. Sohn, "Interfacial nature of Ag nanoparticles supported on TiO_2 photocatalysts," *Journal of Materials Science*, vol. 47, no. 2, pp. 824–832, 2012.

18. A. Murata, N. Oka, S. Nakamura, and Y. Shigesato, "Visible-light active photocatalytic WO_3 films loaded with Pt nanoparticles deposited by sputtering," *Journal of nanoscience and nanotechnology*, vol. 12, no. 6, pp. 5082–5086, 2012.

19. K. Maeda, R. Abe, and K. Domen, "Role and function of ruthenium species as promoters with TaON-based photocatalysts for oxygen evolution in two-step water splitting under visible light," *The Journal of Physical Chemistry C*, vol. 115, no. 7, pp. 3057–3064, 2011.

20. G. R. Bamwenda, S. Tsubota, T. Nakamura, and M. Haruta, "Photoassisted hydrogen production from a water-ethanol solution: a comparison of activities of Au-TiO_2 and Pt-TiO_2," *Journal of Photochemistry and Photobiology A: Chemistry*, vol. 89, no. 2, pp. 177–189, 1995.

21. W. Clark and A. Vondjidis, "An infrared study of the photocatalytic reaction between titanium dioxide and silver nitrate," *Journal of Catalysis*, vol. 4, no. 6, pp. 691–696, 1965.

22. B. Kraeutler and A. Bard, "Heterogenous photocatalytic preparation of supported catalyst. photodeposition of platinum on titanium dioxide powder and other substrates," *J Am Chem Soc*, vol. 100, pp. 4317–4318, 1978.

23. K. Wenderich and G. Mul, "Methods, mechanism, and applications of photodeposition in photocatalysis: A review," *Chemical Reviews*, vol. 116, pp. 14587–14619, 2016.

24. A. Fujishima, "Electrochemical photolysis of water at a semiconductor electrode," *nature*, vol. 238, pp. 37–38, 1972.

25. A. Fahmi, C. Minot, B. Silvi, and M. Causá, "Theoretical analysis of the structures of titanium dioxide crystals," *Physical Review B*, vol. 47, no. 18, p. 11717, 1993.

26. G. L. Chiarello, A. Di Paola, L. Palmisano, and E. Selli, "Effect of titanium dioxide crystalline structure on the photocatalytic production of hydrogen," *Photochemical & Photobiological Sciences*, vol. 10, no. 3, pp. 355–360, 2011.

27. F. Grant, "Properties of rutile (titanium dioxide)," *Reviews of Modern Physics*, vol. 31, no. 3, p. 646, 1959.

28. H. Chen, J. A. Dawson, and N. Umezawa, "Anisotropic nature of anatase TiO_2 and its intrinsic (001) surface electronic states," *Physical Review Applied*, vol. 4, no. 1, p. 014007, 2015.

29. M. Maicu, M. Hidalgo, G. Colón, and J. A. Navío, "Comparative study of the photodeposition of Pt, Au and Pd on pre-sulphated TiO_2 for the photocatalytic decomposition of phenol," *Journal of Photochemistry and Photobiology A: Chemistry*, vol. 217, no. 2, pp. 275–283, 2011.

30. V. Luca, S. Djajanti, and R. F. Howe, "Structural and electronic properties of sol-gel titanium oxides studied by x-ray absorption spectroscopy," *The Journal of Physical Chemistry B*, vol. 102, no. 52, pp. 10650–10657, 1998.

31. A. P. French and E. F. Taylor, *An introduction to quantum physics*. CRC Press, 1979.

32. J. Li and D. Xu, "Tetragonal faceted-nanorods of anatase TiO_2 single crystals with a large percentage of active {100} facets," *Chemical Communications*, vol. 46, no. 13, pp. 2301–2303, 2010.

33. M. Ramamoorthy, D. Vanderbilt, and R. King-Smith, "First-principles calculations of the energetics of stoichiometric TiO_2 surfaces," *Physical Review B*, vol. 49, no. 23, p. 16721, 1994.

34. Y. Miseki, H. Kato, and A. Kudo, "Water splitting into H_2 and O_2 over niobate and titanate photocatalysts with (111) plane-type layered perovskite structure," *Energy & Environmental Science*, vol. 2, no. 3, pp. 306–314, 2009.

35. K. Wenderich, A. Klaassen, I. Siretanu, F. Mugele, and G. Mul, "Sorption-determined deposition of platinum on well-defined platelike WO_3," *Angewandte Chemie International Edition*, vol. 53, no. 46, pp. 12476–12479, 2014.

36. A. Mills, N. Elliott, I. P. Parkin, S. A. O'Neill, and R. Clark, "Novel TiO_2 CVD films for semiconductor photocatalysis," *Journal of Photochemistry and Photobiology A: Chemistry*, vol. 151, no. 1, pp. 171–179, 2002.

37. D. Macwan, P. N. Dave, and S. Chaturvedi, "A review on nano-TiO_2 sol–gel type syntheses and its applications," *Journal of Materials Science*, vol. 46, no. 11, pp. 3669–3686, 2011.

38. P. Löbl, M. Huppertz, and D. Mergel, "Nucleation and growth in TiO_2 films prepared by sputtering and evaporation," *Thin solid films*, vol. 251, no. 1, pp. 72–79, 1994.

39. M. Abou-Helal and W. Seeber, "Preparation of TiO_2 thin films by spray pyrolysis to be used as a photocatalyst," *Applied surface science*, vol. 195, no. 1, pp. 53–62, 2002.

40. G. Li, R. Bai, and X. Zhao, "Coating of TiO_2 thin films on the surface of SiO_2 microspheres: Toward industrial photocatalysis," *Industrial & Engineering Chemistry Research*, vol. 47, no. 21, pp. 8228–8232, 2008.

41. V. Pore, A. Rahtu, M. Leskelä, M. Ritala, T. Sajavaara, and J. Keinonen, "Atomic layer deposition of photocatalytic TiO_2 thin films from titanium tetramethoxide and water," *Chemical Vapor Deposition*, vol. 10, no. 3, pp. 143–148, 2004.

42. S. M. George, "Atomic layer deposition: an overview," *Chemical reviews*, vol. 110, no. 1, pp. 111–131, 2009.

43. W. Chiappim, G. Testoni, R. Moraes, R. Pessoa, J. Sagás, F. Origo, L. Vieira, and H. Maciel, "Structural, morphological, and optical properties of TiO_2 thin films grown by atomic layer deposition on fluorine doped tin oxide conductive glass," *Vacuum*, vol. 123, pp. 91–102, 2016.

44. U. Diebold, "The surface science of titanium dioxide," *Surface science reports*, vol. 48, no. 5, pp. 53–229, 2003.

45. J. Nowotny, "Titanium dioxide-based semiconductors for solar-driven environmentally friendly applications: impact of point defects on performance," *Energy & Environmental Science*, vol. 1, no. 5, pp. 565–572, 2008.

46. L. Kavan, "Electrochemistry of titanium dioxide: some aspects and highlights," *The Chemical Record*, vol. 12, no. 1, pp. 131–142, 2012.

47. X. Pan, M.-Q. Yang, X. Fu, N. Zhang, and Y.-J. Xu, "Defective TiO_2 with oxygen vacancies: synthesis, properties and photocatalytic applications," *Nanoscale*, vol. 5, no. 9, pp. 3601–3614, 2013.

48. U. Diebold, M. Li, O. Dulub, E. L. Hebenstreit, and W. Hebenstreit, "The relationship between bulk and surface properties of rutile TiO_2 (110)," *Surface Review and Letters*, vol. 7, no. 05n06, pp. 613–617, 2000.

49. A. Janotti, J. Varley, P. Rinke, N. Umezawa, G. Kresse, and C. Van de Walle, "Hybrid functional studies of the oxygen vacancy in TiO_2," *Physical Review B*, vol. 81, no. 8, p. 085212, 2010.

50. E. Yagi, R. R. Hasiguti, and M. Aono, "Electronic conduction above 4 K of slightly reduced oxygen-deficient rutile TiO_{2-x}," *Physical Review B*, vol. 54, no. 11, p. 7945, 1996.

51. M. K. Nowotny, L. R. Sheppard, T. Bak, and J. Nowotny, "Defect chemistry of titanium dioxide. application of defect engineering in processing of TiO_2-based photocatalysts," *The Journal of Physical Chemistry C*, vol. 112, no. 14, pp. 5275–5300, 2008.

52. G. Pacchioni, "Oxygen vacancy: the invisible agent on oxide surfaces," *ChemPhysChem*, vol. 4, no. 10, pp. 1041–1047, 2003.

53. I. Nakamura, N. Negishi, S. Kutsuna, T. Ihara, S. Sugihara, and K. Takeuchi, "Role of oxygen vacancy in the plasma-treated TiO_2 photocatalyst with visible light activity for NO removal," *Journal of Molecular Catalysis A: Chemical*, vol. 161, no. 1, pp. 205–212, 2000.

54. N. Serpone, "Is the band gap of pristine TiO_2 narrowed by anion-and cation-doping of titanium dioxide in second-generation photocatalysts?," *Journal of Physical Chemistry B*, vol. 110, no. 48, pp. 24287–24293, 2006.

55. L. Jing, B. Xin, F. Yuan, L. Xue, B. Wang, and H. Fu, "Effects of surface oxygen vacancies on photophysical and photochemical processes of Zn-doped TiO_2 nanoparticles and their relationships," *The Journal of Physical Chemistry B*, vol. 110, no. 36, pp. 17860–17865, 2006.

56. J. Zhuang, W. Dai, Q. Tian, Z. Li, L. Xie, J. Wang, P. Liu, X. Shi, and D. Wang, "Photocatalytic degradation of RhB over TiO_2 bilayer films: effect of defects and their location," *Langmuir*, vol. 26, no. 12, pp. 9686–9694, 2010.

57. X. Jiang, Y. Zhang, J. Jiang, Y. Rong, Y. Wang, Y. Wu, and C. Pan, "Characterization of oxygen vacancy associates within hydrogenated TiO_2: a positron annihilation study," *The Journal of Physical Chemistry C*, vol. 116, no. 42, pp. 22619–22624, 2012.

58. M. Kong, Y. Li, X. Chen, T. Tian, P. Fang, F. Zheng, and X. Zhao, "Tuning the relative concentration ratio of bulk defects to surface defects in TiO_2 nanocrystals leads to high photocatalytic efficiency," *Journal of the American Chemical Society*, vol. 133, no. 41, pp. 16414–16417, 2011.

59. D. C. Hurum, K. A. Gray, T. Rajh, and M. C. Thurnauer, "Recombination pathways in the Degussa P25 formulation of TiO_2: surface versus lattice mechanisms," *The Journal of Physical Chemistry B*, vol. 109, no. 2, pp. 977–980, 2005.

60. M. Hidalgo, J. Murcia, J. Navío, and G. Colón, "Photodeposition of gold on titanium dioxide for photocatalytic phenol oxidation," *Applied Catalysis A: General*, vol. 397, no. 1, pp. 112–120, 2011.

61. M. Chen and D. W. Goodman, "Catalytically active gold: from nanoparticles to ultrathin films," *Accounts of chemical research*, vol. 39, no. 10, pp. 739–746, 2006.

62. X. Pan and Y.-J. Xu, "Fast and spontaneous reduction of gold ions over oxygen-vacancy-rich TiO_2: a novel strategy to design defect-based composite photocatalyst," *Applied Catalysis A: General*, vol. 459, pp. 34–40, 2013.

63. E. Wahlström, N. Lopez, R. Schaub, P. Thostrup, A. Rønnau, C. Africh, E. Lægsgaard, J. K. Nørskov, and F. Besenbacher, "Bonding of gold nanoclusters to oxygen vacancies on rutile TiO_2 (110)," *Physical review letters*, vol. 90, no. 2, p. 026101, 2003.

64. H. Liu, H. Ma, X. Li, W. Li, M. Wu, and X. Bao, "The enhancement of TiO_2 photocatalytic activity by hydrogen thermal treatment," *Chemosphere*, vol. 50, no. 1, pp. 39–46, 2003.

65. T. L. Thompson and J. T. Yates, "TiO_2-based photocatalysis: surface defects, oxygen and charge transfer," *Topics in Catalysis*, vol. 35, no. 3, pp. 197–210, 2005.

66. M. Salari, K. Konstantinov, and H. K. Liu, "Enhancement of the capacitance in TiO_2 nanotubes through controlled introduction of oxygen vacancies," *Journal of Materials Chemistry*, vol. 21, no. 13, pp. 5128–5133, 2011.

67. K. Onda, B. Li, and H. Petek, "Two-photon photoemission spectroscopy of TiO_2 (110) surfaces modified by defects and O_2 or H_2O adsorbates," *Physical Review B*, vol. 70, no. 4, p. 045415, 2004.

68. Q. Wu, Q. Zheng, and R. van de Krol, "Creating oxygen vacancies as a novel strategy to form tetrahedrally coordinated Ti^{4+} in Fe/TiO_2 nanoparticles," *The Journal of Physical Chemistry C*, vol. 116, no. 12, pp. 7219–7226, 2012.

69. L.-Q. Wang, D. R. Baer, M. H. Engelhard, and A. N. Shultz, "The adsorption of liquid and vapor water on TiO_2 (110) surfaces: the role of defects," *Surface science*, vol. 344, no. 3, pp. 237–250, 1995.

70. M. Knotek and P. J. Feibelman, "Ion desorption by core-hole auger decay," *Physical Review Letters*, vol. 40, no. 14, p. 964, 1978.

71. P. Chabert and N. Braithwaite, *Physics of radio-frequency plasmas*. Cambridge University Press, 2011.

72. K. Takeuchi, I. Nakamura, O. Matsumoto, S. Sugihara, M. Ando, and T. Ihara, "Preparation of visible-light-responsive titanium oxide photocatalysts by plasma treatment," *Chemistry letters*, vol. 29, no. 12, pp. 1354–1355, 2000.

73. T. Ihara, M. Miyoshi, M. Ando, S. Sugihara, and Y. Iriyama, "Preparation of a visible-light-active TiO_2 photocatalyst by RF plasma treatment," *Journal of materials science*, vol. 36, no. 17, pp. 4201–4207, 2001.

74. S. Hu, Z. Kang, Z. Ning, J. Ye, F. Li, and Z. Fan, "H_2 plasma treatment to prepare reduced TiO_2 catalyst with high oxygen vacancies content," *Asian Journal of Chemistry*, vol. 26, no. 8, pp. 2403–2406, 2014.

75. T. Takata and K. Domen, "Defect engineering of photocatalysts by doping of aliovalent metal cations for efficient water splitting," *The Journal of Physical Chemistry C*, vol. 113, no. 45, pp. 19386–19388, 2009.

76. A. Czoska, S. Livraghi, M. Chiesa, E. Giamello, S. Agnoli, G. Granozzi, E. Finazzi, C. D. Valentin, and G. Pacchioni, "The nature of defects in fluorine-doped TiO_2," *The Journal of Physical Chemistry C*, vol. 112, no. 24, pp. 8951–8956, 2008.

77. Z. Zhang, J. Long, X. Xie, H. Zhuang, Y. Zhou, H. Lin, R. Yuan, W. Dai, Z. Ding, X. Wang, *et al.*, "Controlling the synergistic effect of oxygen vacancies and N dopants to enhance photocatalytic activity of N-doped TiO_2 by H_2 reduction," *Applied Catalysis A: General*, vol. 425, pp. 117–124, 2012.

78. D. A. Panayotov and J. R. Morris, "Thermal decomposition of a chemical warfare agent simulant (DMMP) on TiO_2: Adsorbate reactions with lattice oxygen as studied by infrared spectroscopy," *The Journal of Physical Chemistry C*, vol. 113, no. 35, pp. 15684–15691, 2009.

79. R. Schlögl, "Heterogeneous catalysis," *Angewandte Chemie International Edition*, vol. 54, no. 11, pp. 3465–3520, 2015.

80. X. Chen, L. Liu, Y. Y. Peter, and S. S. Mao, "Increasing solar absorption for photocatalysis with black hydrogenated titanium dioxide nanocrystals," *Science*, vol. 331, no. 6018, pp. 746–750, 2011.

81. A. Fujishima and X. Zhang, "Titanium dioxide photocatalysis: present situation and future approaches," *Comptes Rendus Chimie*, vol. 9, no. 5, pp. 750–760, 2006.

82. J.-M. Herrmann, "Heterogeneous photocatalysis: state of the art and present applications," *Topics in Catalysis*, vol. 34, no. 1, pp. 49–65, 2005.

83. R. Li, "Latest progress in hydrogen production from solar water splitting via photocatalysis, photoelectrochemical, and photovoltaic-photoelectrochemical solutions," *Chinese Journal of Catalysis*, vol. 38, no. 1, pp. 5–12, 2017.

84. R. Van de Krol and M. Grätzel, *Photoelectrochemical hydrogen production*, vol. 90. Springer, 2012.

85. J. Zhao and X. Yang, "Photocatalytic oxidation for indoor air purification: a literature review," *Building and Environment*, vol. 38, no. 5, pp. 645–654, 2003.

86. V. Iliev, D. Tomova, R. Todorovska, D. Oliver, L. Petrov, D. Todorovsky, and M. Uzunova-Bujnova, "Photocatalytic properties of TiO_2 modified with gold nanoparticles in the degradation of oxalic acid in aqueous solution," *Applied Catalysis A: General*, vol. 313, no. 2, pp. 115–121, 2006.

87. I. Justicia, P. Ordejón, G. Canto, J. L. Mozos, J. Fraxedas, G. A. Battiston, R. Gerbasi, and A. Figueras, "Designed self-doped titanium oxide thin films for efficient visible-light photocatalysis," *Advanced Materials*, vol. 14, no. 19, pp. 1399–1402, 2002.

88. J. Wang, D. N. Tafen, J. P. Lewis, Z. Hong, A. Manivannan, M. Zhi, M. Li, and N. Wu, "Origin of photocatalytic activity of nitrogen-doped TiO_2 nanobelts," *Journal of the American Chemical Society*, vol. 131, no. 34, pp. 12290–12297, 2009.

89. J. Schneider, M. Matsuoka, M. Takeuchi, J. Zhang, Y. Horiuchi, M. Anpo, and D. W. Bahnemann, "Understanding TiO_2 photocatalysis: mechanisms and materials," *Chemical reviews*, vol. 114, no. 19, pp. 9919–9986, 2014.

90. A. N. Shultz, W. Jang, W. Hetherington, D. R. Baer, L.-Q. Wang, and M. H. Engelhard, "Comparative second harmonic generation and x-ray photoelectron spectroscopy studies of the UV creation and O_2 healing of Ti^{3+} defects on (110) rutile TiO_2 surfaces," *Surface Science*, vol. 339, no. 1-2, pp. 114–124, 1995.

91. J. Yang, D. Wang, H. Han, and C. Li, "Roles of cocatalysts in photocatalysis and photoelectrocatalysis," *Accounts of chemical research*, vol. 46, no. 8, pp. 1900–1909, 2013.

92. G. Zhao, H. Kozuka, and T. Yoko, "Sol—gel preparation and photoelectrochemical properties of TiO_2 films containing Au and Ag metal particles," *Thin solid films*, vol. 277, no. 1-2, pp. 147–154, 1996.

93. V. Iliev, D. Tomova, L. Bilyarska, and G. Tyuliev, "Influence of the size of gold nanoparticles deposited on TiO_2 upon the photocatalytic destruction of oxalic acid," *Journal of Molecular Catalysis A: Chemical*, vol. 263, no. 1, pp. 32–38, 2007.

94. M. Hidalgo, M. Maicu, J. A. Navío, and G. Colón, "Effect of sulfate pretreatment on gold-modified TiO_2 for photocatalytic applications," *The Journal of Physical Chemistry C*, vol. 113, no. 29, pp. 12840–12847, 2009.

95. M. Hidalgo, M. Maicu, J. Navío, and G. Colón, "Photocatalytic properties of surface modified platinised TiO_2: effects of particle size and structural composition," *Catalysis Today*, vol. 129, no. 1, pp. 43–49, 2007.

96. M. Hidalgo, M. Maicu, J. Navío, and G. Colón, "Study of the synergic effect of sulphate pre-treatment and platinisation on the highly improved photocatalytic activity of TiO_2," *Applied Catalysis B: Environmental*, vol. 81, no. 1, pp. 49–55, 2008.

97. R. Reichert, Z. Jusys, and R. J. Behm, "Au/TiO_2 photo (electro) catalysis: The role of the Au cocatalyst in photoelectrochemical water splitting and photocatalytic H_2 evolution," *The Journal of Physical Chemistry C*, vol. 119, no. 44, pp. 24750–24759, 2015.

98. G. Yun, G. Y. Song, B.-E. Ahn, S.-K. Lee, J. Heo, K.-S. Ahn, and S. H. Kang, "Beneficial surface passivation of hydrothermally grown TiO_2 nanowires for solar water oxidation," *Applied Surface Science*, vol. 366, pp. 561–566, 2016.

99. A. Gehring and S. Selberherr, "Modeling of tunneling current and gate dielectric reliability for nonvolatile memory devices," *IEEE Transactions on Device and Materials Reliability*, vol. 4, no. 3, pp. 306–319, 2004.

100. F.-C. Chiu, "A review on conduction mechanisms in dielectric films," *Advances in Materials Science and Engineering*, vol. 2014, 2014.

101. N. P. Dasgupta, C. Liu, S. Andrews, F. B. Prinz, and P. Yang, "Atomic layer deposition of platinum catalysts on nanowire surfaces for photoelectrochemical water reduction," *Journal of the American Chemical Society*, vol. 135, no. 35, pp. 12932–12935, 2013.

102. L. Ma, Z. Cui, Z. Li, S. Zhu, Y. Liang, Q. Yin, and X. Yang, "The fabrication of SnSe/Ag nanoparticles on TiO_2 nanotubes," *Materials Science and Engineering: B*, vol. 178, no. 1, pp. 77–82, 2013.

103. E. A. Kozlova and A. V. Vorontsov, "Influence of mesoporous and platinum-modified titanium dioxide preparation methods on photocatalytic activity in liquid and gas phase," *Applied Catalysis B: Environmental*, vol. 77, no. 1, pp. 35–45, 2007.

104. C. Gebauer, D. Hoffmann, Z. Jusys, and R. J. Behm, "Novel, highly conductive Pt/TiO_2 thin-film model catalyst electrodes: The role of metal–support interactions," *ChemElectroChem*, vol. 3, no. 10, pp. 1553–1563, 2016.

105. J. Li, J. Xu, W.-L. Dai, and K. Fan, "Dependence of Ag deposition methods on the photocatalytic activity and surface state of TiO_2 with twistlike helix structure," *The Journal of Physical Chemistry C*, vol. 113, no. 19, pp. 8343–8349, 2009.

106. R. Abe, M. Higashi, and K. Domen, "Overall water splitting under visible light through a two-step photoexcitation between TaON and WO_3 in the presence of an iodate–iodide shuttle redox mediator," *ChemSusChem*, vol. 4, no. 2, pp. 228–237, 2011.

107. A. Peled and N. Mirchin, "Liquid phase photodeposition processes from colloid solutions," in *Photo-Excited Processes, Diagnostics and Applications*, pp. 251–280, Springer, 2003.

108. R. Kydd, J. Scott, W. Y. Teoh, K. Chiang, and R. Amal, "Understanding photocatalytic metallization of preadsorbed ionic gold on titania, ceria, and zirconia," *Langmuir*, vol. 26, no. 3, pp. 2099–2106, 2009.

109. S. Sun, W. Wang, S. Zeng, M. Shang, and L. Zhang, "Preparation of ordered mesoporous Ag/WO_3 and its highly efficient degradation of acetaldehyde under visible-light irradiation," *Journal of hazardous materials*, vol. 178, no. 1, pp. 427–433, 2010.

110. L. M. Peter, "Photoelectrochemistry: From basic principles to photocatalysis," in *Photocatalysis: Fundamentals and Perspectives*, pp. 3–28, Royal Society of Chemistry, 2016.

111. R. Beranek, "(Photo) electrochemical methods for the determination of the band edge positions of TiO_2-based nanomaterials," *Advances in Physical Chemistry*, vol. 2011, 2012.

112. C. Hu, *Modern semiconductor devices for integrated circuits*. Prentice Hall, 2010.

113. B. Ohtani, "Titania photocatalysis beyond recombination: A critical review," *Catalysts*, vol. 3, no. 4, pp. 942–953, 2013.

114. J. Piprek, *Semiconductor optoelectronic devices: introduction to physics and simulation*. Academic press, 2013.

115. J. F. Fernando, M. P. Shortell, C. J. Noble, J. R. Harmer, E. A. Jaatinen, and E. R. Waclawik, "Controlling Au photodeposition on large ZnO nanoparticles," *ACS applied materials & interfaces*, vol. 8, no. 22, pp. 14271–14283, 2016.

116. C. Li, S. Zhang, B. Zhang, D. Su, S. He, Y. Zhao, J. Liu, F. Wang, M. Wei, D. G. Evans, *et al.*, "Photohole-oxidation-assisted anchoring of ultra-small Ru clusters onto TiO_2 with excellent catalytic activity and stability," *Journal of Materials Chemistry A*, vol. 1, no. 7, pp. 2461–2467, 2013.

117. N. T. Thanh, N. Maclean, and S. Mahiddine, "Mechanisms of nucleation and growth of nanoparticles in solution," *Chemical reviews*, vol. 114, no. 15, pp. 7610–7630, 2014.

118. J. Polte, T. T. Ahner, F. Delissen, S. Sokolov, F. Emmerling, A. F. Thünemann, and R. Kraehnert, "Mechanism of gold nanoparticle formation in the classical citrate synthesis method derived from coupled in situ XANES and SAXS evaluation," *Journal of the American Chemical Society*, vol. 132, no. 4, pp. 1296–1301, 2010.

119. C. Besson, E. E. Finney, and R. G. Finke, "A mechanism for transition-metal nanoparticle self-assembly," *Journal of the American Chemical Society*, vol. 127, no. 22, pp. 8179–8184, 2005.

120. C. Xi, Z. Chen, Q. Li, and Z. Jin, "Effects of H^+, Cl^- and CH_3COOH on the photocatalytic conversion of $PtCl_6^{2-}$ in aqueous TiO_2 dispersion," *Journal of Photochemistry and Photobiology A: Chemistry*, vol. 87, no. 3, pp. 249–255, 1995.

121. F. Zhang, J. Chen, X. Zhang, W. Gao, R. Jin, N. Guan, and Y. Li, "Synthesis of titania-supported platinum catalyst: the effect of pH on morphology control and valence state during photodeposition," *Langmuir*, vol. 20, no. 21, pp. 9329–9334, 2004.

122. C. Sungbom, M. Kawai, and K. Tanaka, "XPS studies of the platinum species photodeposited on titania from aqueous chloroplatinic acid," *Bulletin of the Chemical Society of Japan*, vol. 57, no. 3, pp. 871–872, 1984.

123. G. A. Parks, "The isoelectric points of solid oxides, solid hydroxides, and aqueous hydroxo complex systems," *Chemical Reviews*, vol. 65, no. 2, pp. 177–198, 1965.

124. M. Qamar and A. K. Ganguli, "Self-assembling behaviour of Pt nanoparticles onto surface of TiO_2 and their resulting photocatalytic activity," *Bulletin of Materials Science*, vol. 36, no. 6, pp. 945–951, 2013.

125. J.-M. Herrmann, J. Disdier, and P. Pichat, "Photoassisted platinum deposition on TiO_2 powder using various platinum complexes," *Journal of physical chemistry*, vol. 90, no. 22, pp. 6028–6034, 1986.

126. J. Murcia, J. Navío, and M. Hidalgo, "Insights towards the influence of Pt features on the photocatalytic activity improvement of TiO_2 by platinisation," *Applied Catalysis B: Environmental*, vol. 126, pp. 76–85, 2012.

127. L.-H. Chang, Y.-L. Yeh, and Y.-W. Chen, "Preferential oxidation of CO in hydrogen stream over nano-gold catalysts prepared by photodeposition method," *International Journal of Hydrogen Energy*, vol. 33, no. 7, pp. 1965–1974, 2008.

128. S. C. Chan and M. A. Barteau, "Preparation of highly uniform Ag/TiO_2 and Au/TiO_2 supported nanoparticle catalysts by photodeposition," *Langmuir*, vol. 21, no. 12, pp. 5588–5595, 2005.

129. S. Oros-Ruiz, J. Pedraza-Avella, C. Guzmán, M. Quintana, E. Moctezuma, G. Del Angel, R. Gómez, and E. Pérez, "Effect of gold particle size and deposition method on the photodegradation of 4-chlorophenol by Au/TiO_2," *Topics in Catalysis*, vol. 54, no. 8-9, pp. 519–526, 2011.

130. J. Lee and W. Choi, "Photocatalytic reactivity of surface platinized TiO_2: substrate specificity and the effect of Pt oxidation state," *The Journal of Physical Chemistry B*, vol. 109, no. 15, pp. 7399–7406, 2005.

131. H. Nakamatsu, T. Kawai, A. Koreeda, and S. Kawai, "Electron-microscopic observation of photodeposited Pt on TiO_2 particles in relation to photocatalytic activity," *Journal of the Chemical Society, Faraday Transactions 1: Physical Chemistry in Condensed Phases*, vol. 82, no. 2, pp. 527–531, 1986.

132. H. Ishii, S. Juodkazis, S. Matsuo, and H. Misawa, "Photoelectrochemical fabrication of submicrometer platinum pattern on titanium dioxide single crystal surface," *Chemistry letters*, vol. 27, no. 7, pp. 655–656, 1998.

133. Y. Matsumoto, S. Ida, and T. Inoue, "Photodeposition of metal and metal oxide at the TiO_x nanosheet to observe the photocatalytic active site," *The Journal of Physical Chemistry C*, vol. 112, no. 31, pp. 11614–11616, 2008.

134. A. Mills, P. A. Duckmanton, and J. Reglinski, "A simple, novel method for preparing an effective water oxidation catalyst," *Chemical Communications*, vol. 46, no. 14, pp. 2397–2398, 2010.

135. E. M. Steinmiller and K.-S. Choi, "Photochemical deposition of cobalt-based oxygen evolving catalyst on a semiconductor photoanode for solar oxygen production," *Proceedings of the National Academy of Sciences*, vol. 106, no. 49, pp. 20633–20636, 2009.

136. C. Yogi, K. Kojima, T. Takai, and N. Wada, "Photocatalytic degradation of methylene blue by Au-deposited TiO_2 film under UV irradiation," *Journal of materials science*, vol. 44, no. 3, p. 821, 2009.

137. A. Fernandez, A. Caballero, A. Gonzalez-Elipe, J. Herrmann, H. Dexpert, F. Villain, *et al.*, "In situ EXAFS study of the photocatalytic reduction and deposition of gold on colloidal titania," *Journal of Physical Chemistry*, vol. 99, no. 10, pp. 3303–3309, 1995.

138. S. D. Tilley, M. Schreier, J. Azevedo, M. Stefik, and M. Graetzel, "Ruthenium oxide hydrogen evolution catalysis on composite cuprous oxide water-splitting photocathodes," *Advanced Functional Materials*, vol. 24, no. 3, pp. 303–311, 2014.

139. T. Ohno, L. Bai, T. Hisatomi, K. Maeda, and K. Domen, "Photocatalytic water splitting using modified GaN: ZnO solid solution under visible light: long-time operation and regeneration of activity," *Journal of the American Chemical Society*, vol. 134, no. 19, pp. 8254–8259, 2012.

140. P. J. Ross, *Taguchi techniques for quality engineering: loss function, orthogonal experiments, parameter and tolerance design*. McGraw Hill Professional, 1996.

141. Y. Leng, *Materials characterization: introduction to microscopic and spectroscopic methods*. John Wiley & Sons, 2009.

142. L. Kiss, J. Söderlund, G. Niklasson, and C. Granqvist, "New approach to the origin of lognormal size distributions of nanoparticles," *Nanotechnology*, vol. 10, no. 1, p. 25, 1999.

143. S. N. Chiu, D. Stoyan, W. S. Kendall, and J. Mecke, *Stochastic geometry and its applications*. John Wiley & Sons, 2013.

144. D. Moltchanov, "Distance distributions in random networks," *Ad Hoc Networks*, vol. 10, no. 6, pp. 1146–1166, 2012.

145. P. J. Clark and F. C. Evans, "Distance to nearest neighbor as a measure of spatial relationships in populations," *Ecology*, vol. 35, no. 4, pp. 445–453, 1954.

146. M. Trzcinski, A. Antończak, P. Domanowski, M. Kustra, W. Wachowiak, M. Naparty, T. Hiller, A. Bukaluk, A. Wronkowska, *et al.*, "Characterisation of coloured TiO_x/Ti/glass systems," *Applied Surface Science*, vol. 322, pp. 209–214, 2014.

147. J. Aarik, A. Aidla, A.-A. Kiisler, T. Uustare, and V. Sammelselg, "Effect of crystal structure on optical properties of TiO_2 films grown by atomic layer deposition," *Thin Solid Films*, vol. 305, no. 1-2, pp. 270–273, 1997.

148. J. Halley, M. Kozlowski, M. Michalewicz, W. Smyrl, and N. Tit, "Photoelectrochemical spectroscopy studies of titanium dioxide surfaces: theory and experiment," *Surface science*, vol. 256, no. 3, pp. 397–408, 1991.

149. S. Juodkazis, H. Ishii, S. Matsuo, and H. Misawa, "Photoelectrochemical submicrometer patterning of titanium dioxide by platinum," *Journal of Electroanalytical Chemistry*, vol. 473, no. 1, pp. p. 235–239, 1999.

150. F. Zhang, J. Chen, X. Zhang, W. Gao, R. Jin, and N. Guan, "Simple and low-cost preparation method for highly dispersed Pd/TiO_2 catalysts," *Catalysis today*, vol. 93, pp. 645–650, 2004.

151. A. V. Vorontsov, E. N. Savinov, and J. Zhensheng, "Influence of the form of photodeposited platinum on titania upon its photocatalytic activity in CO and acetone oxidation," *Journal of Photochemistry and Photobiology A: Chemistry*, vol. 125, no. 1, pp. 113–117, 1999.

152. B. Hammer and J. Norskov, "Why gold is the noblest of all the metals," *Nature*, vol. 376, no. 6537, pp. 238–240, 1995.

Appendices

A Confidence intervals in the photodeposition of gold

In Appendix A, the confidence intervals of the variables used in this thesis for the photodeposition of gold are evaluated. All seven variables (H_2 treatment, CH_3OH concentration, light intensity, deposition time, precursor concentration, N_2 purging time and pH) are processed in their own figures (Figures A1-A7, respectively). All figures have three histograms, indicating the influence of the variable to (a) particle density, (b) particle size and (c) nearest neighbor distance. The confidence intervals of σ and 2σ are indicated with dotted line on both sides of the average value (solid line). If the slope value of 0 is outside the σ level, it can be deduced that the variable affects the property in question at the probability of 68%. Similarly, if the slope value of 0 is outside the 2σ line, the same probability is 95%.

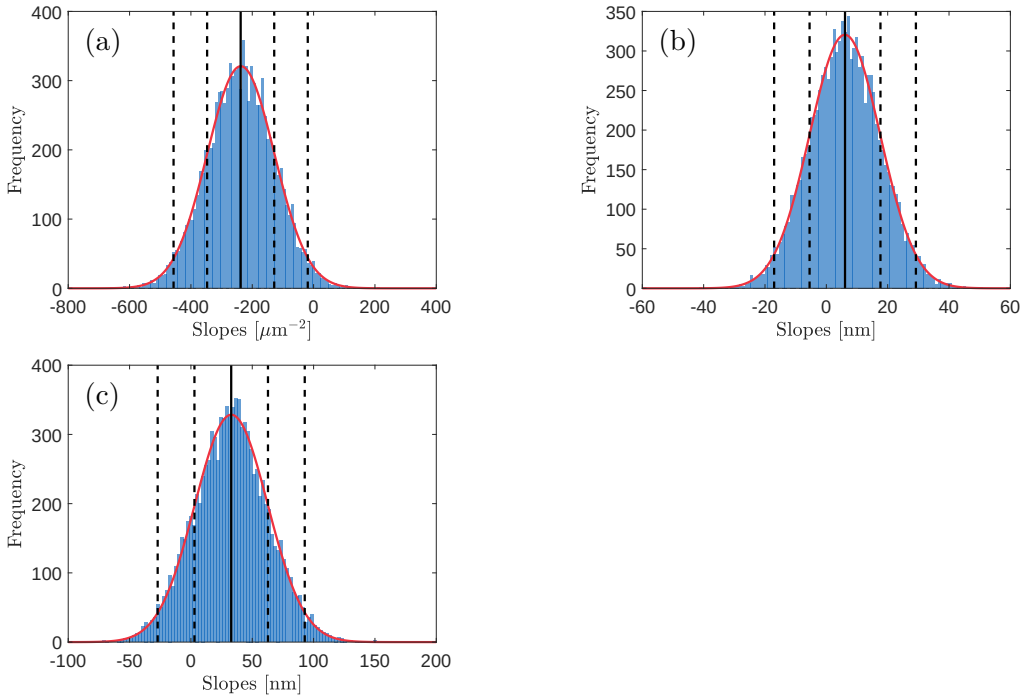

Figure A1: The confidence intervals of the H_2 treatment to the (a) particle density, (b) particle size, (c) nearest neighbor distance of the photodeposition of gold.

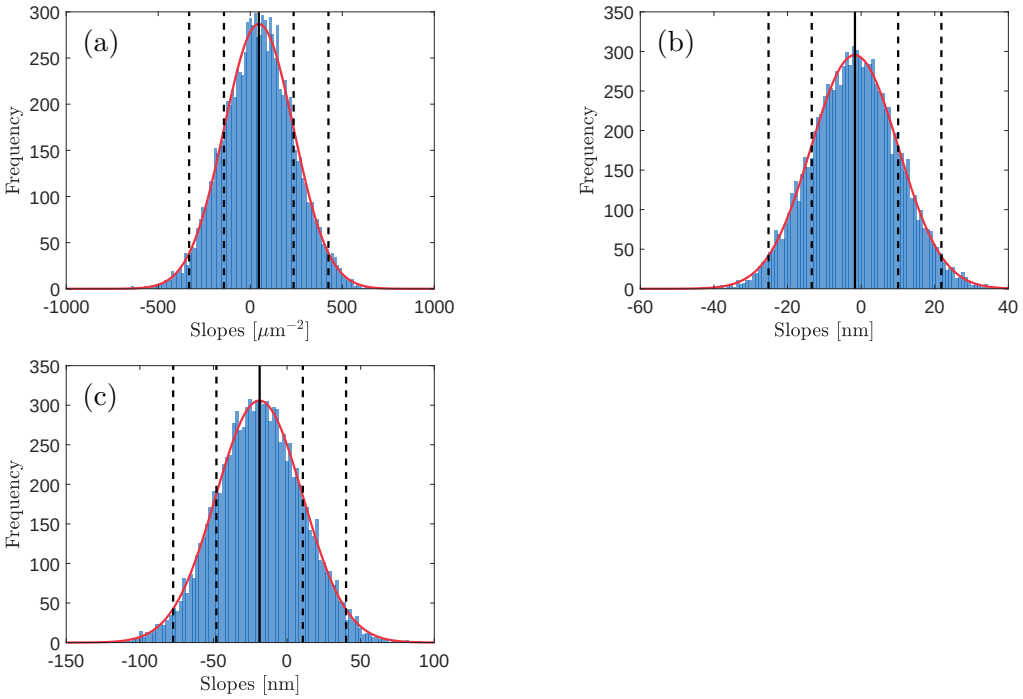

Figure A2: The confidence intervals of the sacrificial methanol concentration to the (a) particle density, (b) particle size, (c) nearest neighbor distance of the photodeposition of gold.

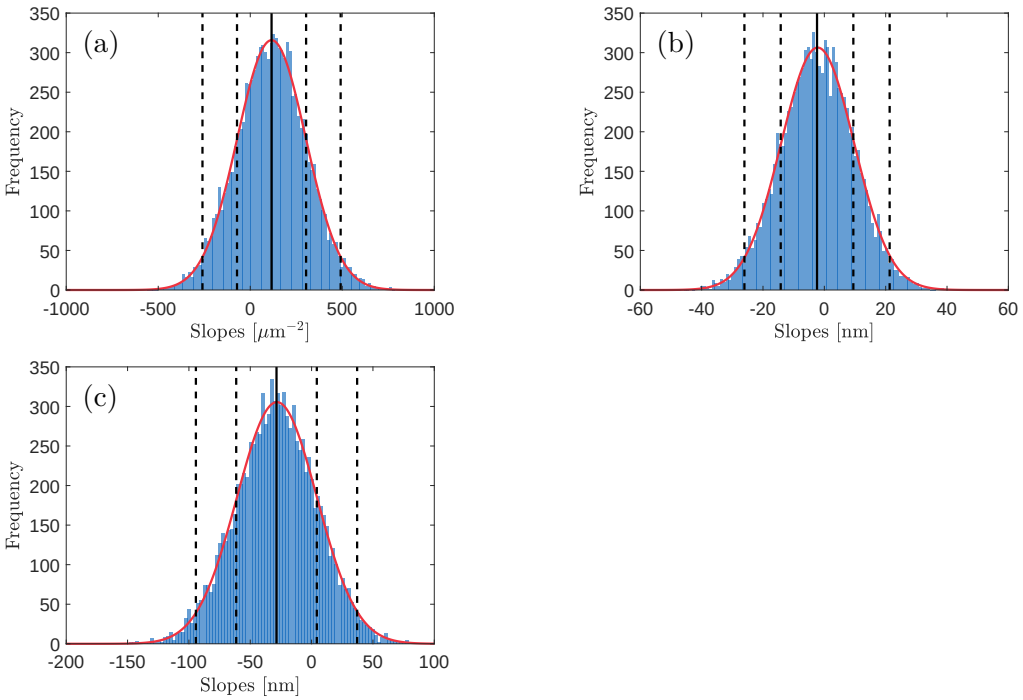

Figure A3: The confidence intervals of the light intensity to the (a) particle density, (b) particle size, (c) nearest neighbor distance of the photodeposition of gold.

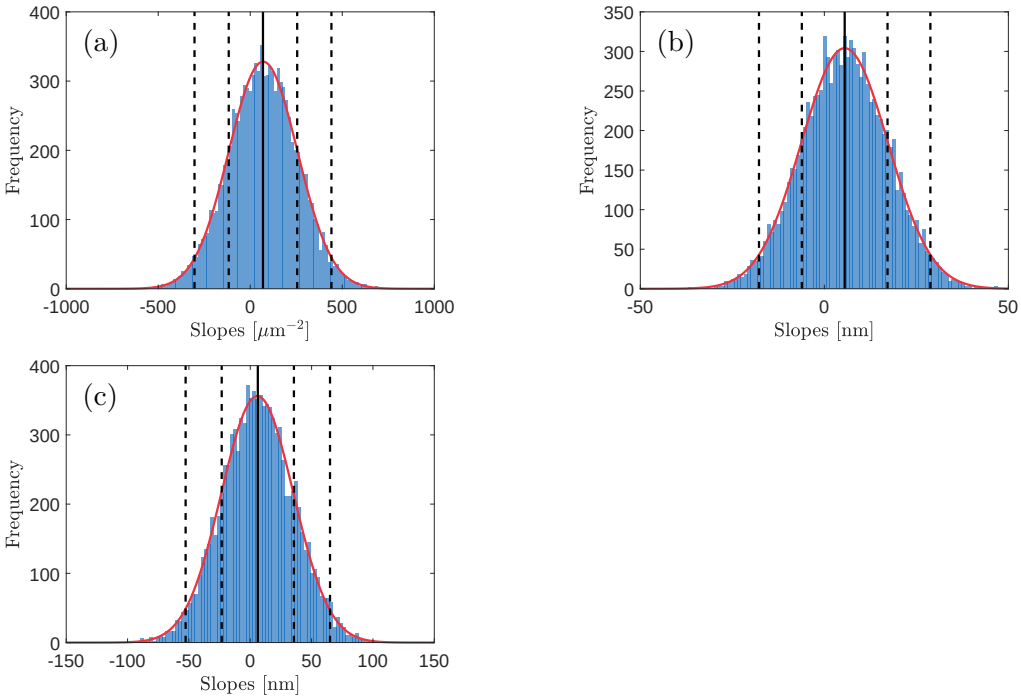

Figure A4: The confidence intervals of the deposition time to the (a) particle density, (b) particle size, (c) nearest neighbor distance of the photodeposition of gold.

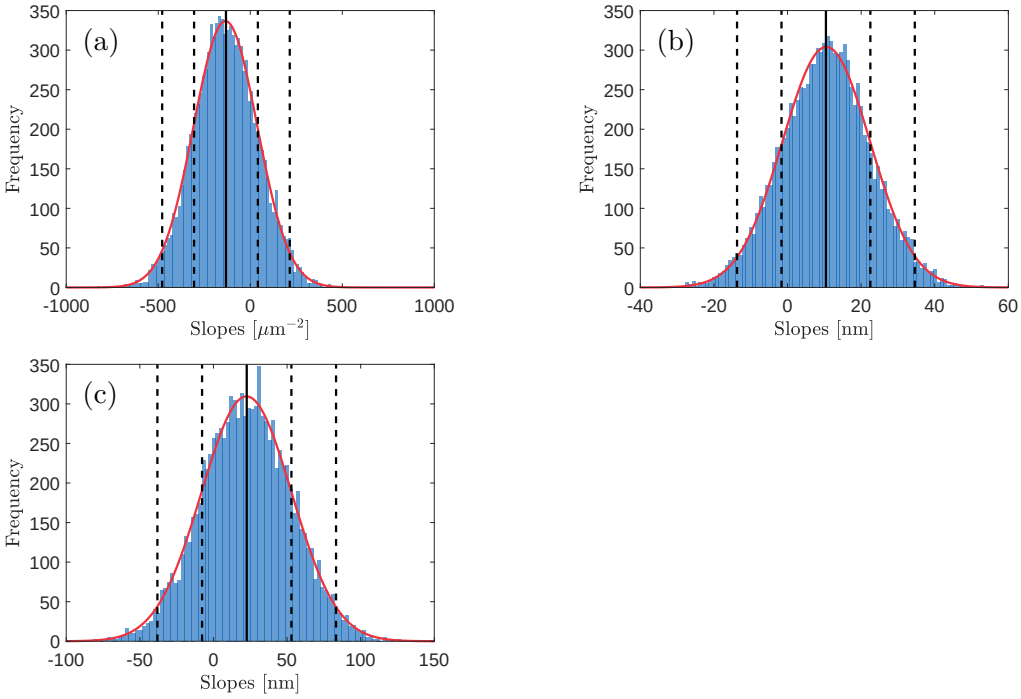

Figure A5: The confidence intervals of the precursor concentration to the (a) particle density, (b) particle size, (c) nearest neighbor distance of the photodeposition of gold.

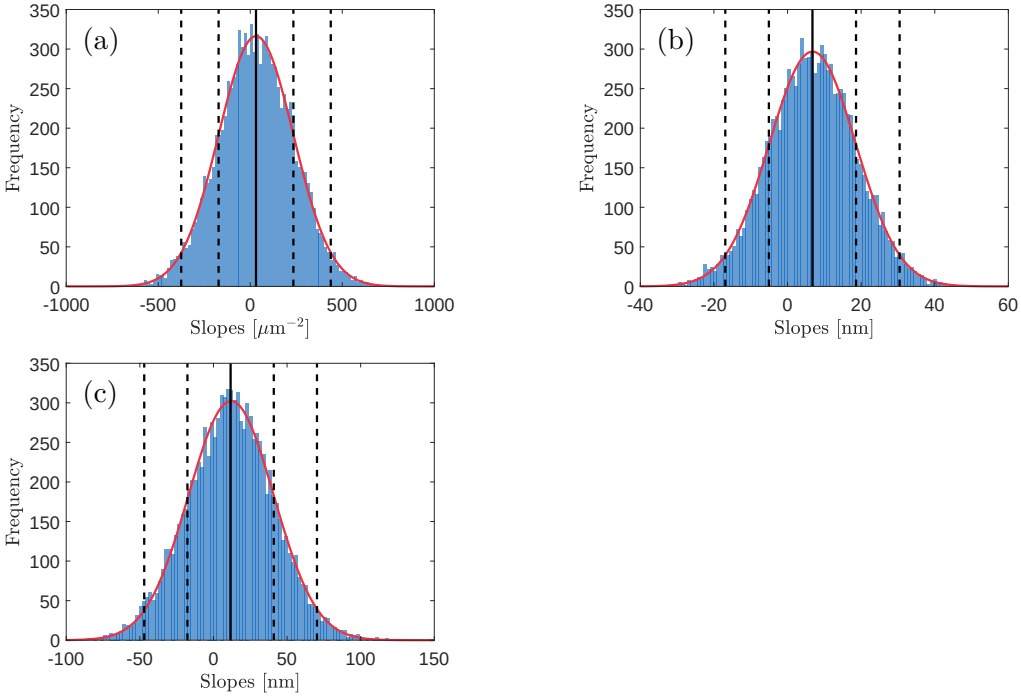

Figure A6: The confidence intervals of the N_2 purging time to the (a) particle density, (b) particle size, (c) nearest neighbor distance of the photodeposition of gold.

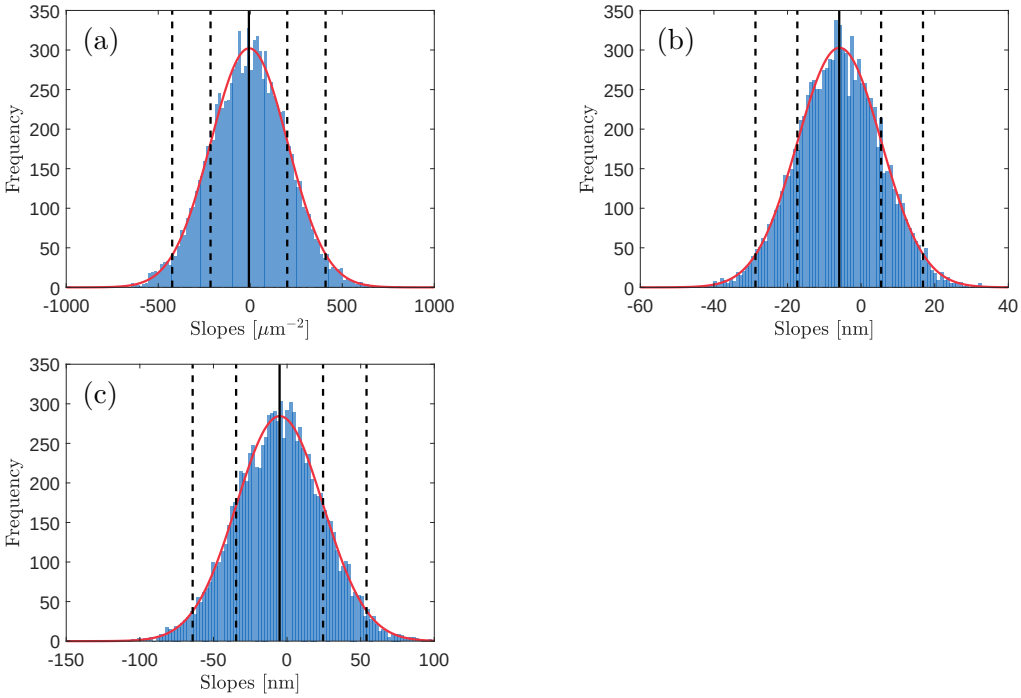

Figure A7: The confidence intervals of the solution pH to the (a) particle density, (b) particle size, (c) nearest neighbor distance of the photodeposition of gold.

B Confidence intervals in the photodeposition of platinum

In Appendix B, the confidence intervals of the variables used in this thesis for the photodeposition of platinum are evaluated. All seven variables (H_2 treatment, CH_3OH concentration, light intensity, deposition time, precursor concentration, N_2 purging time and pH) are processed in their own figures (Figures A1-A7, respectively). All figures have three histograms, indicating the influence of the variable to (a) particle density, (b) particle size and (c) nearest neighbor distance. The confidence intervals of σ and 2σ are indicated with dotted line on both sides of the average value (solid line). If the slope value of 0 is outside the σ level, it can be deduced that the variable affects the property in question at the probability of 68%. Similarly, if the slope value of 0 is outside the 2σ line, the same probability is 95%.

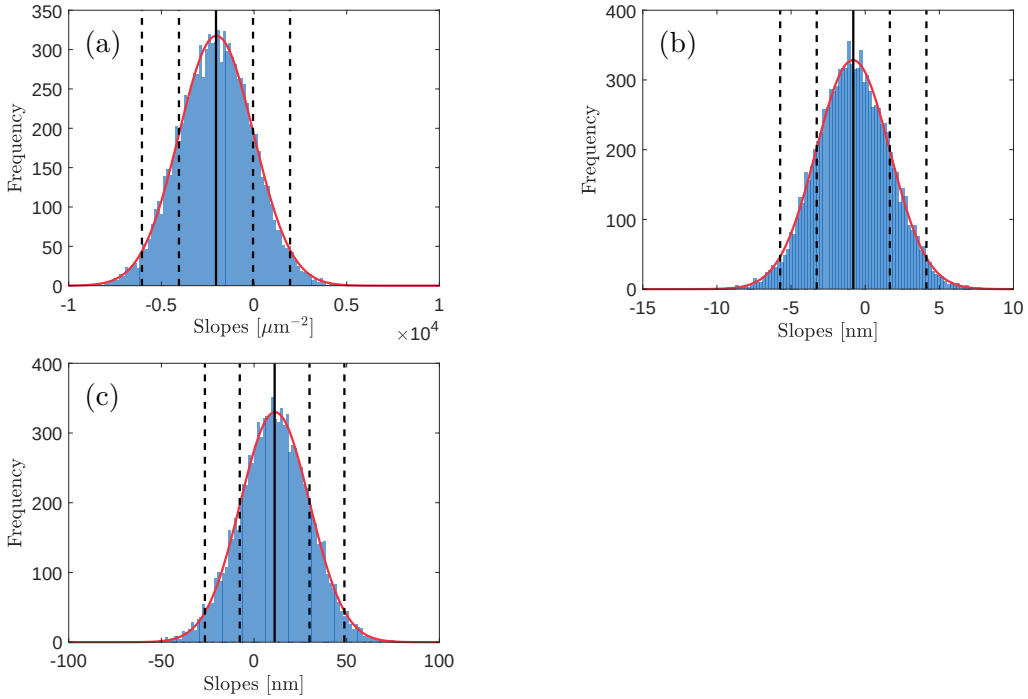

Figure B1: The confidence intervals of the H_2 treatment to the (a) particle density, (b) particle size, (c) nearest neighbor distance of the photodeposition of platinum.

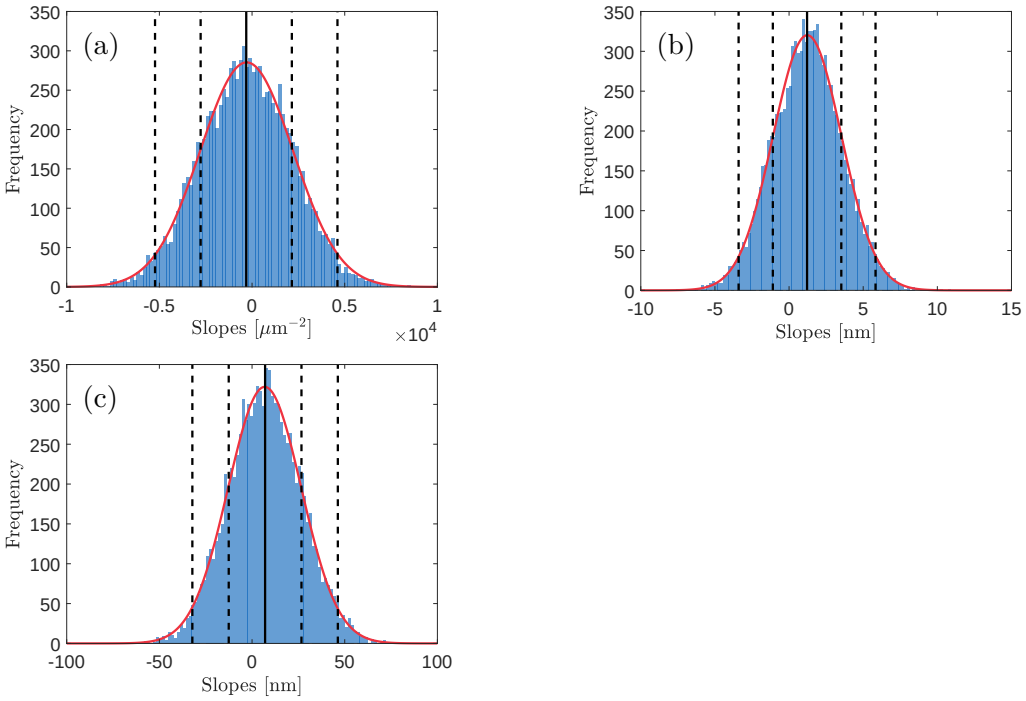

Figure B2: The confidence intervals of the sacrificial methanol concentration to the (a) particle density, (b) particle size, (c) nearest neighbor distance of the photodeposition of platinum.

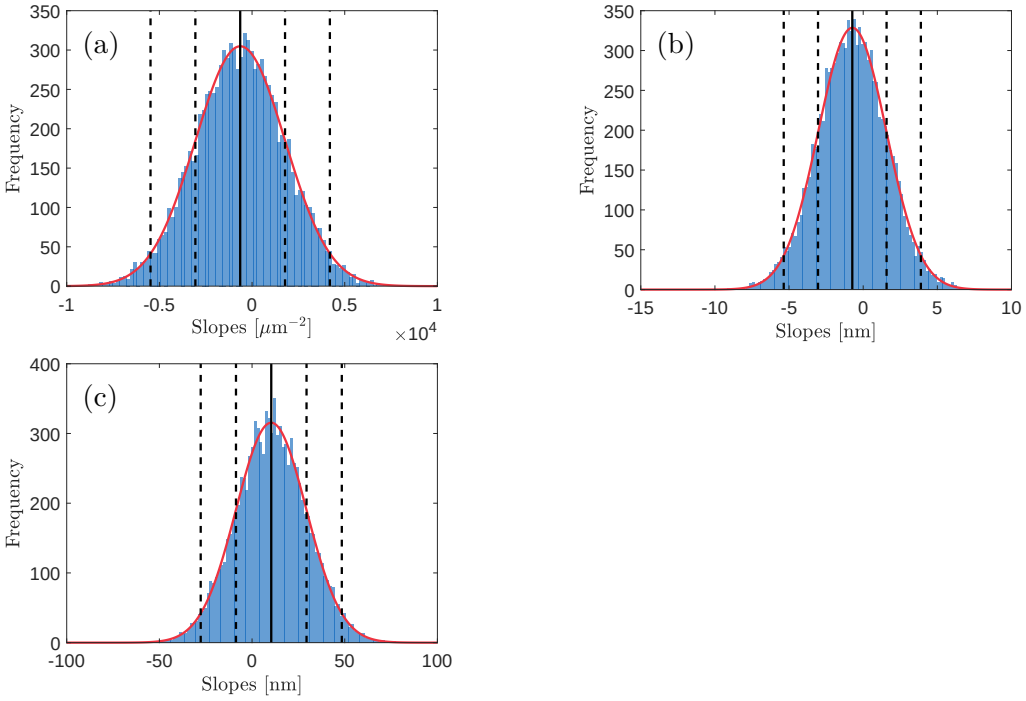

Figure B3: The confidence intervals of the light intensity to the (a) particle density, (b) particle size, (c) nearest neighbor distance of the photodeposition of platinum.

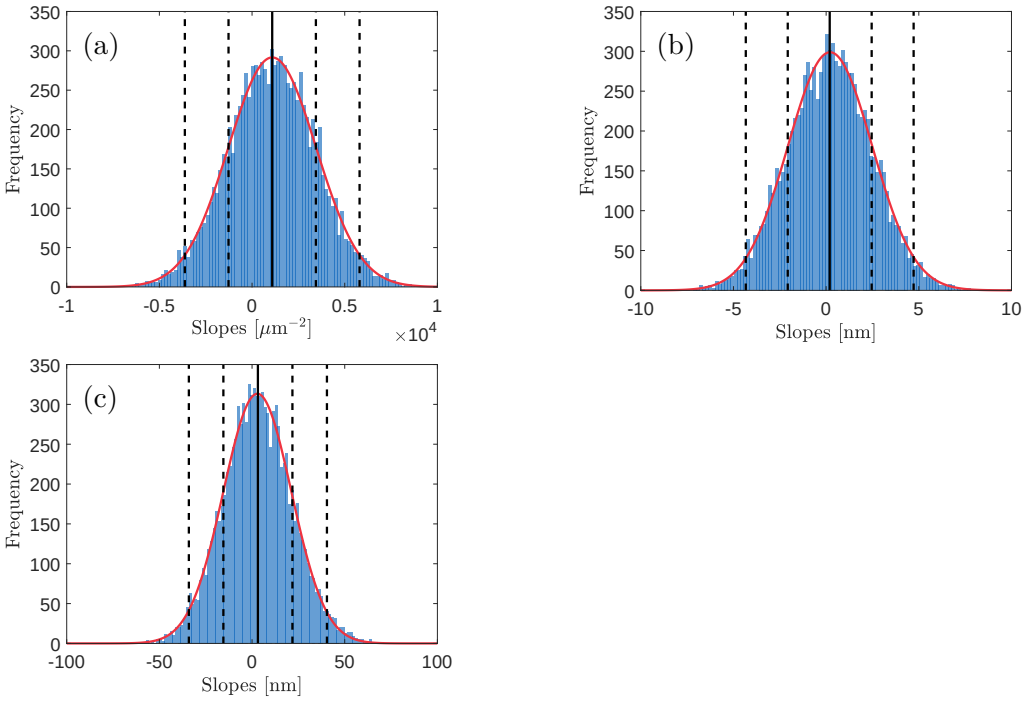

Figure B4: The confidence intervals of the deposition time to the (a) particle density, (b) particle size, (c) nearest neighbor distance of the photodeposition of platinum.

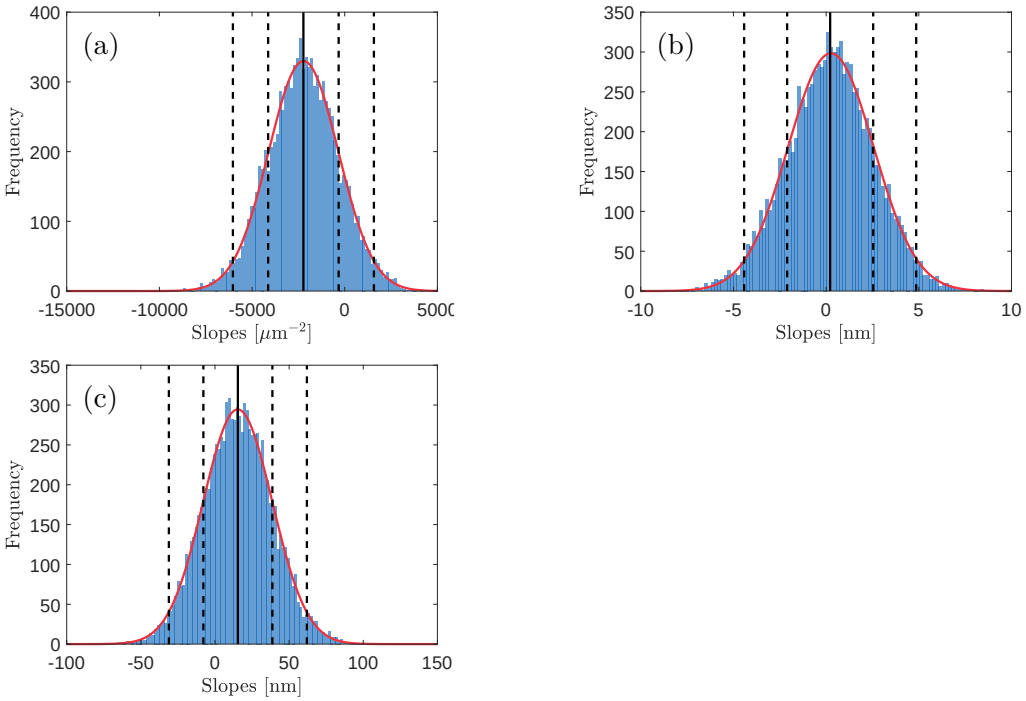

Figure B5: The confidence intervals of the precursor concentration to the (a) particle density, (b) particle size, (c) nearest neighbor distance of the photodeposition of platinum.

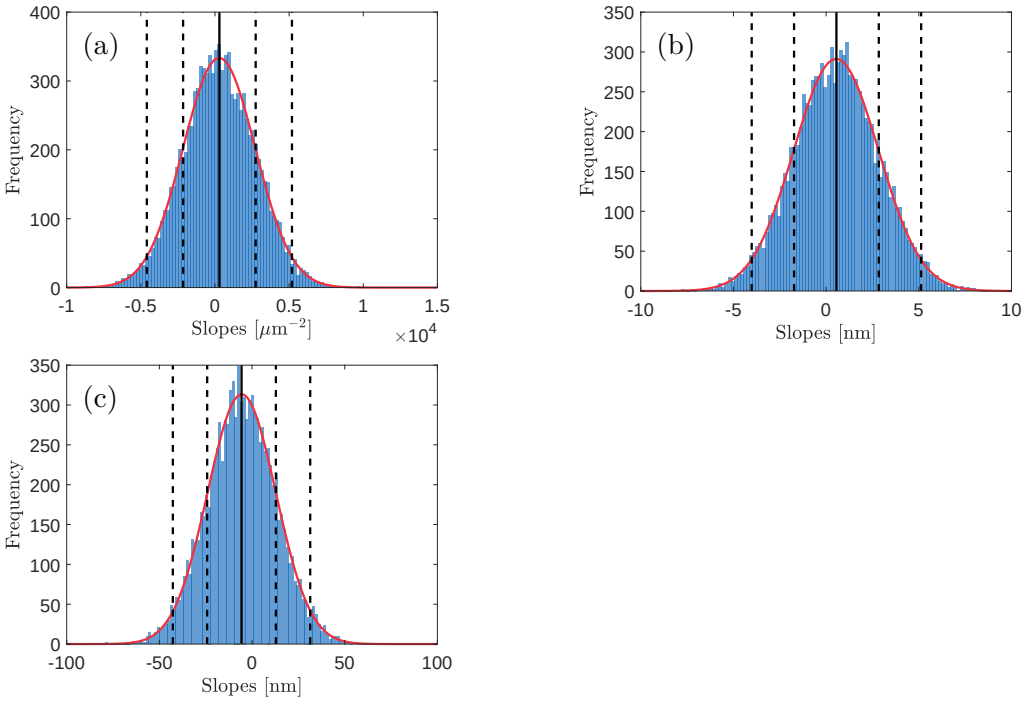

Figure B6: The confidence intervals of the N_2 purging time to the (a) particle density, (b) particle size, (c) nearest neighbor distance of the photodeposition of platinum.

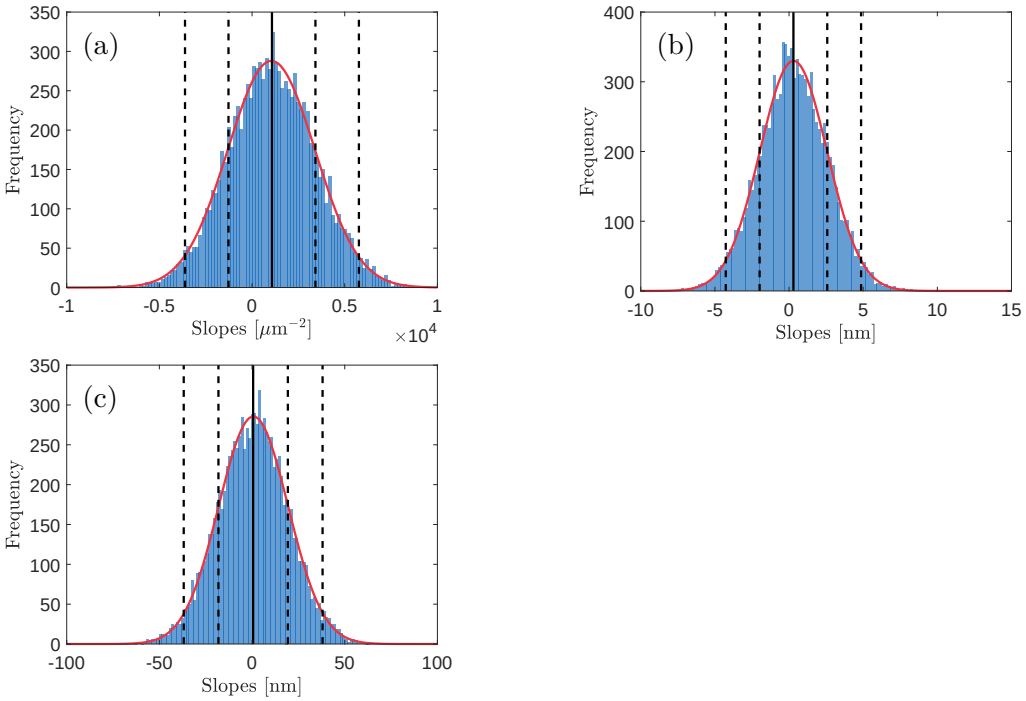

Figure B7: The confidence intervals of the solution pH to the (a) particle density, (b) particle size, (c) nearest neighbor distance of the photodeposition of platinum.